Curved beam based model for piston-ring designs in internal combustion engines

By

Mohamed Aziz Bhouri

B.Sc., Mechanical Engineering
Ecole Centrale Paris, 2015

Submitted to the Department of Mechanical Engineering
in Partial Fulfillment of the Requirements of the Degree of

Master of Science in Mechanical Engineering

at the

MASSACHUSETTS INSTITUTE OF TECHNOLOGY

June 2017

Signature of Author: Signature redacted
Department of Mechanical Engineering
May 12th, 2017

Certified by: Signature redacted
Dr. Tian Tian
Principal Research Engineer, Department of Mechanical Engineering
Thesis Supervisor

Accepted by: Signature redacted
Professor Rohan Abeyaratne
Chairman, Committee on Graduate Students
Department of Mechanical Engineering

Curved beam based model for piston-ring designs in internal combustion engines

By

Mohamed Aziz Bhouri

Submitted to the Department of Mechanical Engineering on May 12th, 2017
in Partial Fulfillment of the Requirements of the Degree of
Masters of Science in Mechanical Engineering

Abstract

Characterizing the piston ring behavior is inherently associated with the oil consumption, friction, wear and blow-by in internal combustion engines. This behavior varies along the ring's circumference and determining these variations is of utmost importance for developing ring-packs achieving desired performances in terms of sealing and conformability. This study based on straight beam model was already developed but does not consider the lubrication sub-models, the tip gap effects and the characterization of the ring free shape based on any final closed shape. In this work, three numerical curved beam based models were developed to study the performance of the piston ring-pack.

The conformability model was developed to characterize the behavior of the ring within the engine. In this model, the curved beam model is adopted with considering ring-bore and ring-groove interactions. This interactions include asperity and lubrication forces. Besides, gas forces are included to the model along with the inertia and initial ring tangential load. In this model we also allow for bore, groove upper and lower flanks thermal distortion. We also take into account the thermal expansion effect of the ring and the temperature gradient from inner diameter (ID) to outer diameter (OD) effects. The piston secondary motion and the variation of oil viscosity on the liner with its temperature in addition to the existence of fuel and the different hydrodynamic cases (Partially and fully flooded cases) are considered as well. This model revealed the ring position relative to the groove depending on the friction, inertia and gas pressures. It also characterizes the effect of non-uniform oil distribution on the liner and groove flanks. Finally, the ring gap position within a distorted bore also reveals the sealing performance of the ring.

Using the curved beam model we also developed a module determining the twist calculation under fix ID or OD constraint. The static twist is an experimental characterization of the ring during which the user taps on the ring till there is a minimum clearance between the ring lowest point and the lower plate all over the ring's circumference but without any force contact.

Our last model includes four sub-models that relate the ring free shape, its final shape when subjected to a constant radial pressure (this final shape is called ovality) and the force distribution in circular bore. Knowing one of these distribution, this model determines the other two. This tool is useful in the sense that the characterization of the ring is carried out by measuring its ovality which is more accurate than measuring its free shape or force distribution in circular bore. Thus, having a model that takes the ovality as an input is more convenient and useful based on the experiments carried out to characterize the ring.

Thesis Supervisor: Dr. Tian Tian

Acknowledgements

During my Masters at MIT I had the opportunity to meet wonderful people whom I would like to thank for their contributions not only regarding my development on the professional level but also on the personal one. In particular I would like to thank my thesis supervisor Dr. Tian Tian, who not only gave me the opportunity to carry out my Masters studies at MIT, but also supported and guided me consistently through his insightful and broad knowledge. I enjoyed and will always remember every single discussion that we had and which helped me solve the problems I faced and lead to the achievement of my thesis work. Besides the academic support, I would also like to thank Dr. Tian Tian for being a supportive friend for all his lab students including me during the two years that I spent within his group.

I would also like to thank Yang Liu, Camille Baelden and Liang Liu from whom I took over my Masters project. Their knowledge and mostly my discussion with Yang helped me understand the basic of the problems and the challenges to face.

This work is sponsored by the consortium on lubrication in internal combustion engines at MIT with additional support by Argonne national laboratory and US department of energy. The current consortium members are Daimler AG, Mahle GmbH, MTU Friedrichshafen, PSA Peugeot Citroën, Renault S.A., Royal Dutch Shell, Toyota, Volkswagen AG, Volvo Cars, Volvo Truck, and Weichai Power. Our meetings were an opportunity not only to motivate me to improve myself but also an invaluable occasion to share knowledge and gain experience. I would especially like to thank MAHLE and Eduardo Tomanik for proving us with the ovality measurements and the theoretical characterizations coming along with them.

I also gratefully acknowledge the support and friendship of the Sloan Automotive Laboratory faculty and stuff. In particular I would like to thank my office mates Yang Liu, Vinayak Teja Kalva, Sebastian Ahling, Zhen Meng, Chongjie Gu, Yuwei Li, Tianshi Fang, Sarthak Vaish, Qing Zhao, Zhe Chen and Xiaofeng Qin for their contribution to my thesis work and their effort to make my time at MIT enjoyable and fulfilling.

My family and friends' support has been an essential part of my academic career throughout these past two years. I would first like to express my deepest thanks and gratitude to my incredible parents Kamila El-Abassi and Amor Bhouri. Their love and unlimited sacrifice from the moment I was born was the greatest gift anyone has ever given me. I would also like to thank my wonderful brother Ghassen for his endless support and words of comfort at times of challenges and adversity. Lastly, I would like to extend my gratification to my lovely girlfriend Ons M'Saad. Her encouragement has been one of the driving forces in my pursuit of my life goals. This thesis would not have been completed without the unconditional help and support of my loved ones.

Mohamed Aziz Bhouri
May 2017

Dedication

A ma mère,

Kamila El-Abassi

Cette thèse est la vôtre

Table of Contents

List of Figures

Figure 5.31 – Free shape curvature comparison for fitted measured ovality with one 8th order polynomial for the whole ring (usual case)

Figure 5.32 – Force distribution recovered from fitted measured ovality with one 8th order polynomial for the whole ring with a liner roughness of 0.3 (left curve) and $3\ \mu m$ (right curve) for the usual case

Figure 5.33 – Force distribution recovered from fitted measured ovality with one 8th order polynomial for the whole ring with a liner roughness of 10 (left curve) and $50\ \mu m$ (right curve) for the usual case

Figure 5.34 – Extrapolated curvature and force distribution comparison from fitted measured ovality with the least square method based on 3rd order polynomial shape functions (usual case)

Figure 5.35 – Extrapolated curvature and force distribution comparison from fitted measured ovality with one 8th order polynomial for the whole ring (usual case)

1. Introduction

1.1. Background and Motivation

1.1.1. Piston ring pack system

The piston ring pack system which is the study subject of our work is composed of the piston and the three piston rings (Figure 1.1).

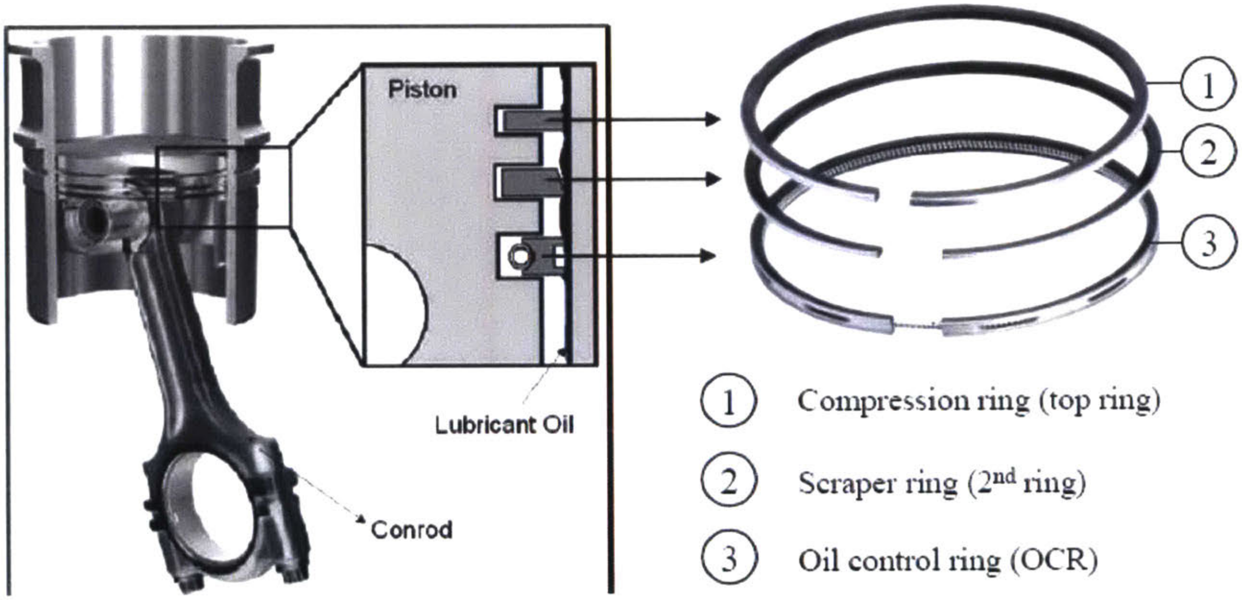

Figure 1.1 – Overview of the Power Cylinder System (PCS)

The main function of the piston is to transmit the mechanical work done by the ignited gas fuel mixture on the combustion chamber to the crankshaft. The piston presents some geometrical features that are related to its functions and shown in Figure 1.2.

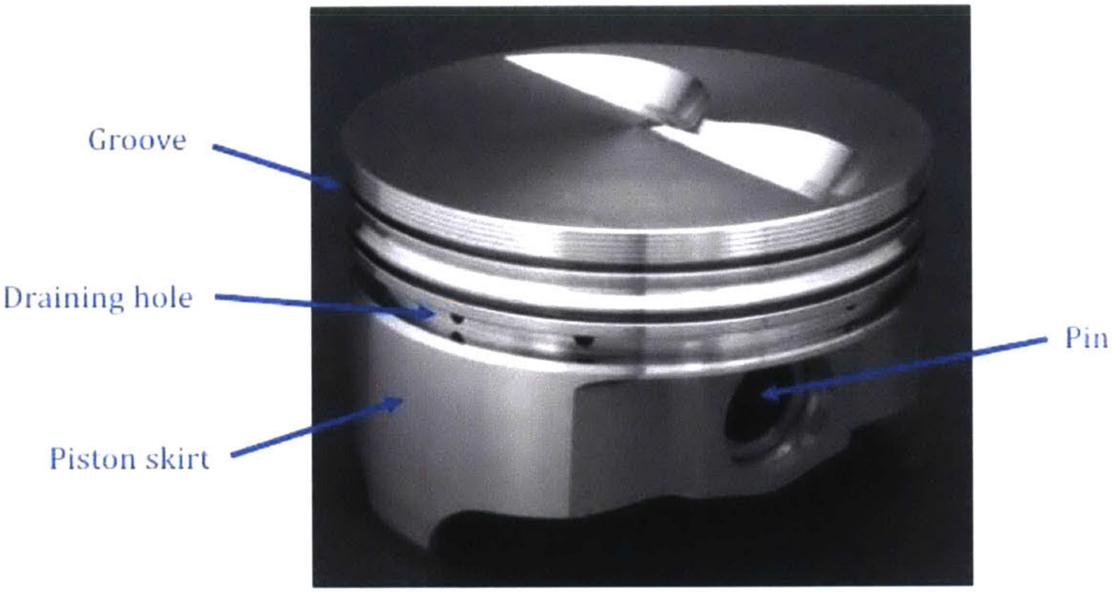

Figure 1.2 – Overview of the piston geometry

The piston presents three grooves on its side to insert the piston rings. The 3rd groove generally contains draining holes in order to let oil and gas flow to the crankcase. The piston skirt is located below the grooves and 90 degrees on both side of the pin. This surface is in contact with the cylinder liner and its function is to maintain the lateral forces and guide the piston in the cylinder.

Each piston ring has a specific function. The compression ring or the top ring primary function is to prevent gas leakage from the combustion chamber through the piston-liner clearance. The 3rd ring or oil control ring (OCR) controls the amount of lubrication oil that is supplied to the ring pack. Oil supply to the piston skirt is large and the function of the OCR is to let only a thin film of oil left on the liner such that a proper lubrication of the top two rings is maintained with a reasonable oil consumption. The second ring, also called scraper ring, has a hybrid function related to oil lubrication and gas pressure since it limits the rise of pressure in the region above the OCR and stops the excessive amount of lubricant that passed the OCR.

The nomenclature of the piston ring pack is shown on a section view of piston, cylinder and ring pack in Figure 1.3.

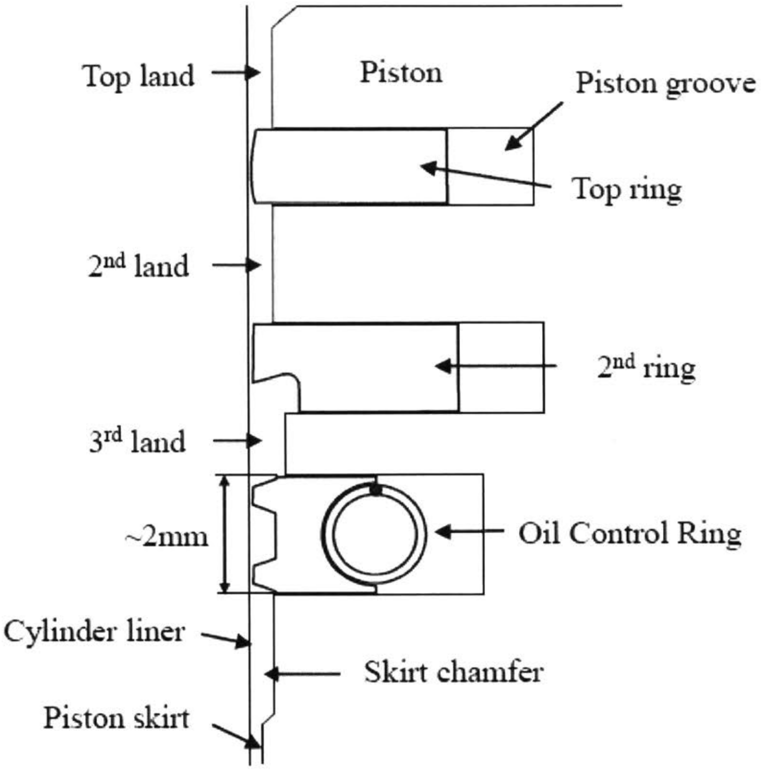

Figure 1.3 – Nomenclature of the piston ring pack

The piston outer surfaces between the chamfers are called piston land. Cylinder-land clearances vary by design to control gas pressure in different regions of the ring pack. The top of the piston skirt can present a cut or a chamfer whose functions are to retain oil to lubricate the piston skirt during the up stroke and to limit the build-up pressure in the oil below the OCR. The chamfer could be a square cut or a diagonal one.

The three piston rings have different designs based on their functions. The compression ring generally present a rectangular cross section. Its running face has a microscopic parabolic profile in order to favor generation of hydrodynamic pressure for lubrication purposes. Other features can be added such as static twist in order to push the ring against the top groove lower flank and make sure the ring prevents gas leakage when its upper surface is exposed to high gas pressure. This positive static twist can be achieved by creating a cut at the upper ID. This lets the top ring contact the lower groove flank at the ID first and due to the rising pressure in the cylinder and the smaller one at in the second land region, the ring is pushed towards the groove lower flank preventing high pressure gas from leaking towards the second land and lower cylinder regions. The second ring presented in Figure 1.3 is a Napier ring which is a common design for second rings. The hook acts like an oil reservoir to prevent oil flowing on the piston 3rd land from returning to the liner and hence prevent it from evaporating. To assemble the top two rings within the cylinder, we close them from their free shapes modifying their curvature and torsion which increases their internal energy and provide them with an expansion radial force and static twist. This helps the top two rings to be conform to the liner and groove interfaces. The OCR or 3rd ring present a distinct design from the top two rings. The OCR presented in figure 1.3 is a two piece OCR and has two components: a metallic ring and a coiled spring located in the inner diameter of the metallic ring. This particular design ensures maximum flexibility of the OCR so that it maintains contact with the cylinder independently from its deformation. The top two rings rely on the ring elastic force created when closing them in the cylinder to provide a radial contact pressure sealing the ring-liner interface. However the OCR does not generate enough elastic force when closed since it has a thin section which is why a coiled spring is placed at its inner diameter. The OCR maintains contact with the liner by only two thin portions of its outer diameter. They present a flat profile parallel to the liner. This property helps increase the contact pressure and limits the hydrodynamic pressure generation, which helps control the oil film thickness supplied to the top two rings and thus limits oil consumption.

1.1.2. Energy efficiency in internal combustion engines

New engines design is driven by three major factors: fuel economy, pollutant emission and customer satisfaction. To fulfill these requirements, more developed technologies and tools are needed for all aspects of engines including lubrication oil, fuel and engine components. The piston ring-pack performance is inherently related to the friction, blow-by gas and oil consumption. Therefore, a detailed understanding of the piston ring-pack behavior is of utmost importance in order to develop internal combustion engines with better performance.

Blow-by gas refers to the undesired gas leakage from the combustion chamber to the crankcase. Therefore, sine unburned working charge may flow from the combustion towards the crankcase and hence do not contribute to the work production. Besides, this leakage will reduce the in-cylinder pressure and hence decrease the engine power. Blow-by gas flow is determined by the ring-liner and ring-groove conformability and is a major factor of the piston ring pack performance.

A major source of pollutant emissions is the engine oil consumption. Partially burned and unburned oil in the exhaust gases contribute directly to the generation of hydrocarbon and particle emissions. In addition, exhaust treatment devices performance are altered by the chemical compounds existing in oil additives and hence reduce their efficiency. In order to understand oil consumption, we should characterize oil transport from lower region to the combustion chamber. Oil flow between the ring's gaps, along the liner and along the piston are three major oil paths. Oil transport along the liner is mainly determined by the rind pack lubrication and ring-liner conformability, while oil transport along the piston is mainly controlled by the ring-groove conformability and gas pressures. The study of ring conformability can help to understand the oil transport phenomenon and to investigate new strategies to reduce the oil consumption.

Piston ring friction accounts for 25% of the power loss in power cylinder systems [1] and reducing it is among engine manufacturers priorities based on its impact on the total engine mechanical losses. Since ring-liner and ring-groove frictions are largely determined by the ring-liner and ring-groove lubrication and the relative clearances, a study of the lubrication performance of piston ring pack based on the ring conformability needs to be carried out. Besides, gas pressure effect influence ring conformability with the groove and liner and thus should also be thoroughly studied.

Ring-liner friction is generated due to the sliding contact between the piston ring and the cylinder liner. This force is of opposite direction to the ring motion and created energy losses.

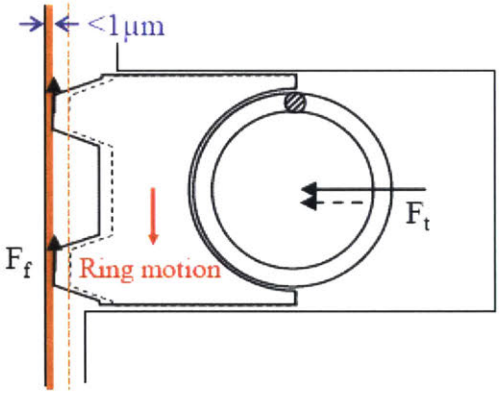

Figure 1.4 – Illustration of the compromise between frication reduction and oil consumption

The friction force F_f is the product of the normal load of the ring-liner contact and the friction coefficient f_c (1.1).

$$F_f = 2\Pi f_c F_t$$

(1.1)

The ring tension F_t for a ring with a standard deign is the tangential load required to close its gap and is statistically equivalent to a uniform radial pressure distribution. Since the integration of the ring tension of the ring circumference is equal to $2\Pi F_t$, the radial force per unit length f_r is given by (1.2) where R is the radius of the closed ring.

$$f_r = \frac{F_t}{R}$$

(1.2)

Based on equation (1.1), friction can be reduced by either reducing the friction coefficient in order to keep the same radial load, or by reducing the ring tension and thus the radial load. It is usually easier to reduce the ring tension than the friction coefficient by changing the coiled spring in the case of the OCR or modifying the free shape of the ring for the top two ones. Reducing the friction coefficient for ring-liner interaction is carried out by choosing the surface material, designing the ring profile and liner surface roughness and adjusting the lubrication oil properties such as its viscosity [2]. The interaction force between the piston ring and the liner is characteristic of sliding contact which is represented by Stribeck [3], [4] curve presented in Figure 1.5. This curves shows the variation of the friction coefficient as a function of dimensionless number combining the oil viscosity μ, the sliding speed V, the bore radius R and the ring tension F_t. This number defines the different lubrication regimes. The friction coefficient reaches a minimal value at the interface between the mixed lubrication case and the hydrodynamic lubrication one.

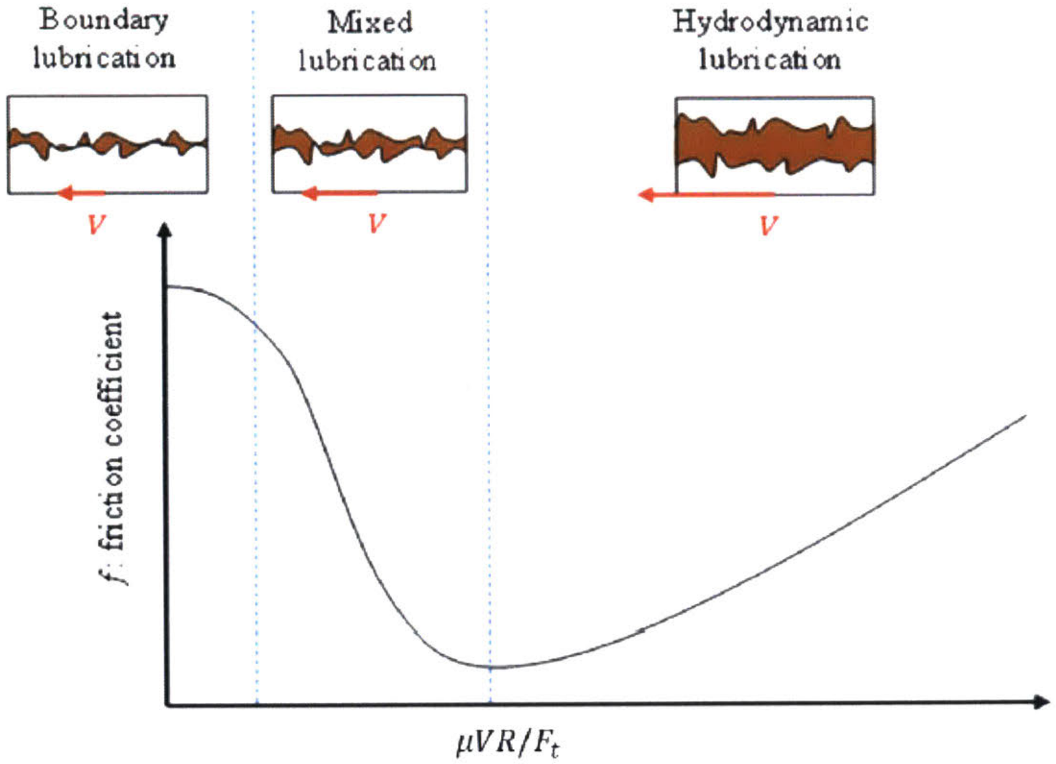

Figure 1.5 – Stribeck curve of a sliding contact

As we can see a compromise has to be made between tension reduction in order to reduce friction and sealing performances of the ring. As presented in Figure 1.4, reducing ring tension will decrease the radial force pushing the ring against the cylinder and thus will result in a thicker oil film (the dashed lines show the reduce tension case). This shows the negative impact of reducing OCR tension on oil consumption by allowing a larger amount of oil passing through [5]. Although the width of the OCR lands can be reduced in order to maintain the magnitude of the contact pressure, the main argument is still valid and tension reduction reduces the force maintaining the ring in contact with the cylinder affecting its sealing performance.

Another source of losing ring-liner conformability is bore distortion under thermal and mechanical loads which affects oil consumption. The cylinder is deformed due to stresses from the engine block assembly and gradients of temperature created by heat transfer from combustion chamber to coolant. These deformation, though they are small compared to the bore radius. The latter is generally of order $80\ mm$. The 0th order bore distortion which corresponds to the thermal expansion has a magnitude of order $100\ \mu m$. The second order results from the difference in the liner temperature in the circumferential direction depending on the cooling chamber position and is on the order of $10\ \mu m$. The mechanical stresses from the engine block assembly cause the 3rd and 4th order bore distortion which are on the order of 1 μm. These local deformations are able to affect the ring-liner clearance significantly. Bore distortion deforms the initial circular shape into a deformed one with multiple lobes around the circumference (Figure 1.6).

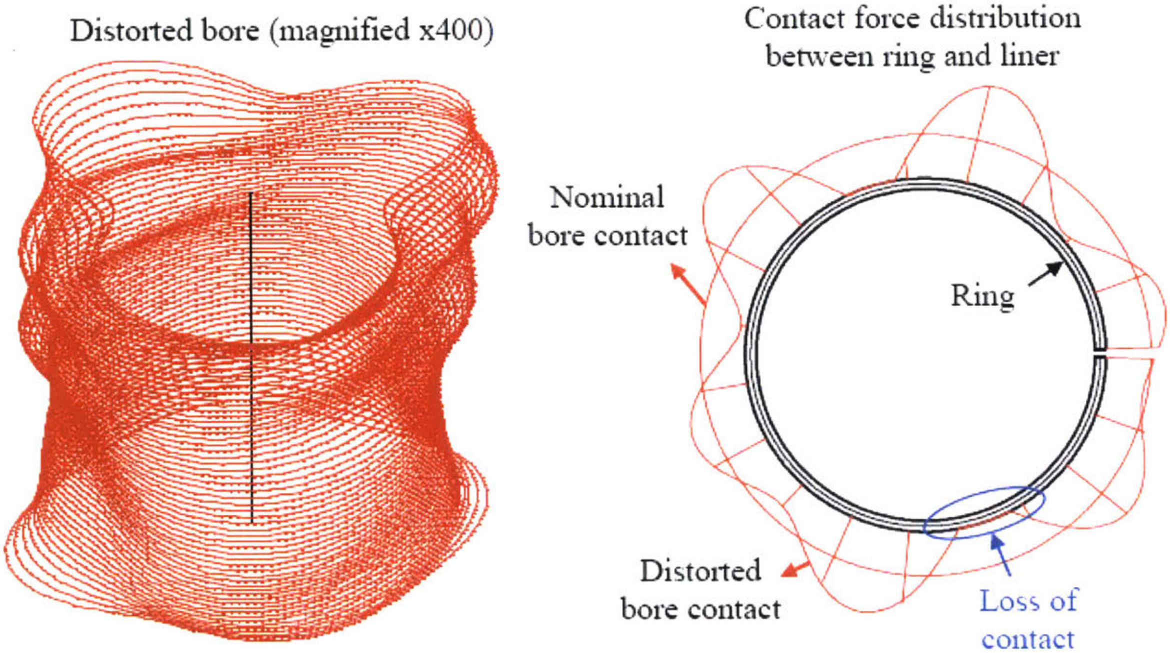

Figure 1.6 – Bore distortion and its effect on the contact between the ring and the liner

A ring with a relative high stiffness and / or small tension might not be able to adapt to these local changes of geometry and thus lose contact. As a consequence, the sealing performance of the ring for oil and gas is also hampered. For instance, a difference in the ring-liner clearance between the down and up strokes can result in oil up-scraping (Figure 1.7).

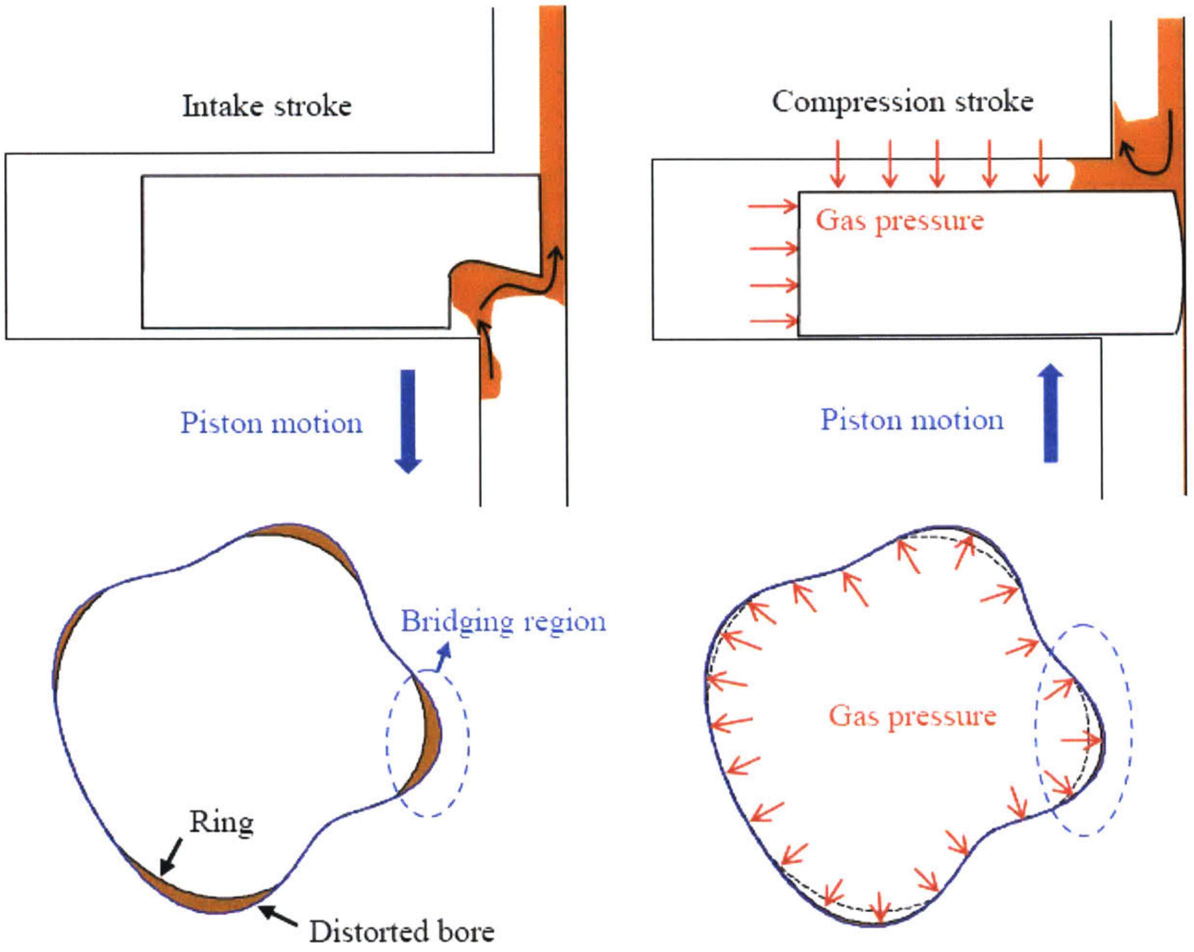

Figure 1.7 – Ring-liner conformability and oil up-scraping

This scenario can happen for top rings during the intake and compression strokes. If the bore distortion is large enough to cause the second ring to lose contact with the liner as presented in Figure 1.6, then during the intake stroke, oil can connect to the liner at the location of the second ring and a thick oil film is able to pass the ring to the upper region. The compression ring will have a similar liner clearance as the second ring and therefore it will also allow this oil film to slide over to the top land during the intake stroke. However during the compression stroke, the increasing gas pressure in the top ring groove will make the top ring conform to the distorted bore. Therefore the thick oil film that was left on the liner during the intake stroke will be scraped and flow to the top land. Thereafter, during the combustion stroke or even before, oil will be consumed either by being evaporated or throw off in the combustion chamber. Thus, the difference of conformability between the intake and compression stroke can also contribute to oil consumption.

Ring-groove conformability can also affect oil consumption (figure 1.8). During the down stroke, the OCR scrapes oil lubricating the piston skirt. This oil will accumulate below the OCR. In the initial phase of the down stroke, inertia and friction holds the ring against the upper flank of the piston groove creating a channel of a height in the order of 50 µm between the groove lower flank and the ring which lets oil flow since oil pressure below the ring is higher than the pressure inside the groove.

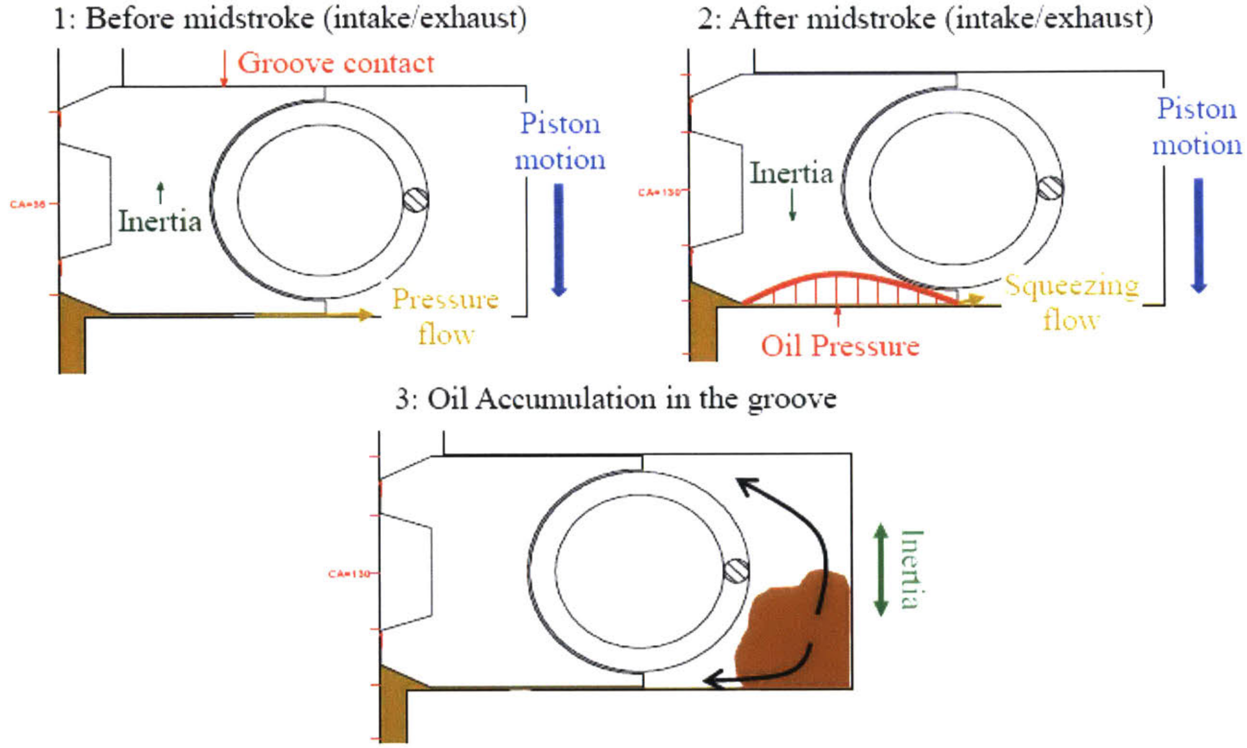
1: Before midstroke (intake/exhaust)

2: After midstroke (intake/exhaust)

3: Oil Accumulation in the groove

Figure 1.8 – Ring-groove conformability and oil pumping

The direction of inertia is reversed during the second half of the down stroke and oil is squeezed by the ring on the lower flank of the groove. Therefore, a fraction of the oil is transferred to the groove region behind the ring. After being repeated at every engine cycle, oil accumulates in the groove and once the amount of oil in that region is large enough, it can flow to the upper flank of the groove due to the inertia force and hence oil can flow to the third land through the ring-groove interface.

Finally, the piston is free to rotate around the pin connecting the piston to the connecting rode and to move laterally due to the radial clearance between the piston skirt and the cylinder liner. Tilt and lateral displacement constitute the piston secondary motion. Piston tilt cannot be neglected when modeling piston rings since tilted piston grooves force the ring to tilt and twist. As shown in Figure 1.9, the piston tilt is denoted by β_p and the piston lateral displacement by y_p.

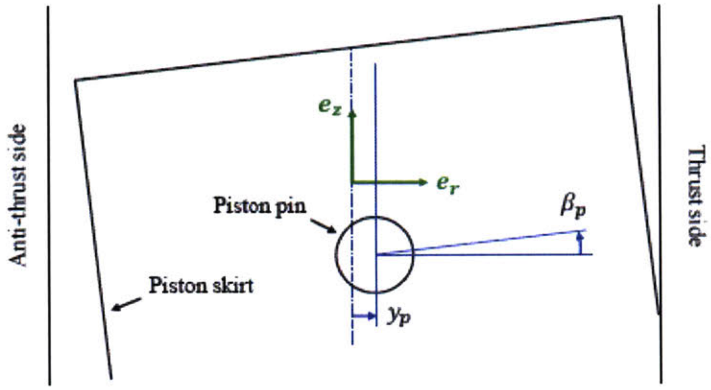

Figure 1.9 – Piston secondary motion and ring relative position

A positive piston tilt corresponds to an upward movement of the thrust side and a downward movement of the anti-thrust side. Positive lateral motion means that the piston is moving towards the thrust side. This lateral motion is due to the reaction of the tilted connecting rod to both the action of inertia and gas pressure on the piston. The piston tilt is due to the axial motion of the center of the skirt contact and variation of the skirt friction. Piston secondary motion was studied by Bai [6,7].

Piston secondary motion is important in modeling oil transport around the ring pack system. Lateral displacement modifies the clearance between the piston lands and the liner, thus modifying the gas pressure. Inertial force and gas pressure push the piston ring to conform to the groove geometry forcing them to twist as shown in Figure 1.10.

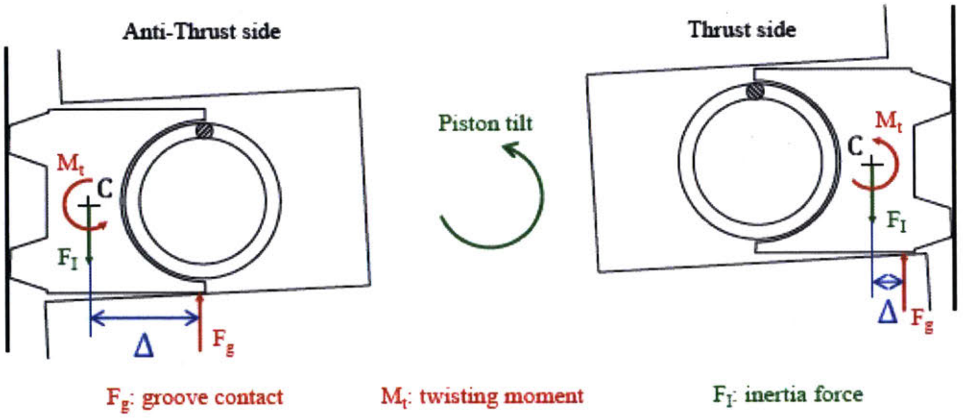

Figure 1.10 – Piston tilt and ring relative position

Ring twist affects the oil film thickness left on the liner and this is more significant for the OCR, since it can result in a loss of contact of one of the OCR lands. Piston tilts varies in the engine cycle. Initially, during the down-stroke, ring twist forces the OCR to twist negatively such that the lower land-liner clearance is larger than the upper land-liner clearance which makes oil accumulate between the two lands. Later in the down-stroke, the direction of the OCR twist is reversed and inertial force may drive the oil to the liner. This phenomenon is called bridging and in this case it happens between the OCR two lands. In this scenario, the amount of oil accumulated is released to the liner. During the upstroke, the OCR moves back to the initial position that we described since ring twist changes its direction and the oil is scraped from the liner and can flow to the piston as demonstrated in Figure 1.11.

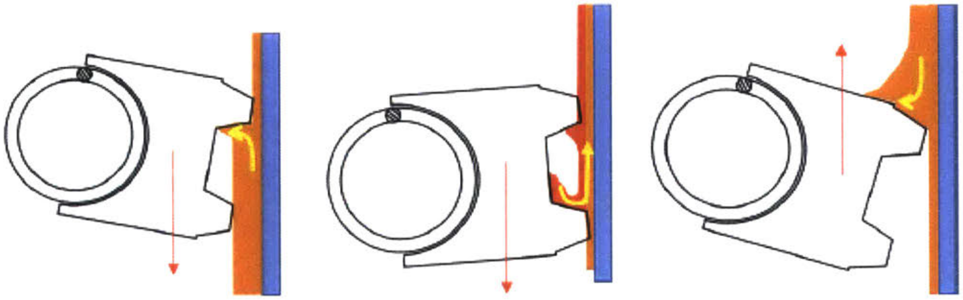

Figure 1.11 – OCR twist and oil transport

A great deal of efforts has been made to investigate the piston ring pack performance. In particular, numerical simulation has played a central role in modeling the different engine components along with the oil lubrication and gas pressure in order to better understand the behavior of the whole system. Numerical methods include static analysis that refers to the study of the static interaction between a ring and the power cylinder system including the liner, the groove, the lubrication oil and gases. In the following sections, the existing modeling works and their limitations are reviewed.

1.2. Static analysis

Ring design include two categories: material and geometry designs. Geometry design for top two rings relies on three key elements, namely ring free shape, its cross-section and its running surface profile and these elements determine the interaction of the ring with the liner as well as with the piston groove [8,9].

Considering only dry contact and oil lubrication, the ring-liner interaction is determined by the ring geometry and the bore shape. Due to the thermal expansion and cylinder head bolting, the bore is not perfectly circular and is subject to distortions. At the same time, ring geometry is rarely found as designed initially, mainly because of the plastic deformation during the manufacturing stages. Thereby, it is crucial in practice to know the contact force based on the ring geometry and bore shape.

There are multiple analytical works on ring bore conformability. Timoshenko and Lessell [10] presented a solution for a circular ring conforming to a circular bore, where they developed a formula for a variable wall thickness of a rectangular cross-section ring in order to achieve a uniform contact pressure on a circular bore. Sun [11] modeled the ring as a curved beam with in-plane elastic, gas and thermal loads at a steady state within a distorted bore. The identification of the bore distortion as a potential source of oil consumption [12], [13], [14] triggered several studies. An analytical criterion to compute the maximum admissible bore distortion was carried out by Mueller [15]. Dunaevsky used a similar analytical approach and statistical treatment of bore distortion in order to determine different bore distortion limits [16]-[20]. Later on, Tomanik suggested a new conformability criterion based on experimental measurement of ring conformability limits [21], [22]. Using ANSYS, Ma et al. [23] developed different independent models (gap model, cable model and thermal liner model) to study ring-liner conformability and also the effect of thermal stress.

Most of these models rely on the small displacement assumption. However, the ring shape change significantly when the ring is closed from it free shape into the bore and hence that assumption is no longer valid and would cause notable errors. Besides, all the existing models were developed for ring with symmetric cross-section, while rings could also be designed to have asymmetric cross-section in practice. This asymmetry will affect the ring behavior since it will introduce liner and angular displacement in all directions, which will affect ring-bore and ring-groove interactions.

Finite element methods have been used to model the structural behavior of the ring and its interaction with the cylinder [24]-[27]. However most of the existing structural model are based on straight beam model which has some limitations as the discontinuity of physical properties at the nodes of the finite element grid such as the curvature in addition to the large number of elements needed to reach sufficient accuracy which hamper the computation cost of these models.

It is of utmost importance for ring manufacturers to have an analytical tool that determines the required ring free shape which will provide the desired ring-bore and ring-groove conformability and the required interactions. Besides, taking into account thermal moment, piston secondary motion, gas pressures and the different lubrication cases is of practical interest since it models the ring within engine working conditions. Prescott et al. [28] has developed an analytical solution for the free shape of a ring with constant rectangular cross-section that will give a uniform ring-bore contact pressure. That solution is quoted as the basis of piston ring design. However, that tool does not determine the ring free shape for any arbitrary contact pressure distribution.

In order to control oil transport more efficiently, compression rings are generally designed to have static twist angles once inserted into the piston and cylinder. This is accomplished by designing asymmetric cross-section. It is of practical interest for ring designers to have an analytical tool that determines the ring static twist based on its design which will facilitate the iterative design process needed to obtain the desired static twist. Few published studies on the ring static twist calculation are available. Dunaevsky et al. [17], [19], [29] have developed models that can be used in order to calculate the ring static twist. However, the boundary conditions used within these models do not really correspond to the engine applications.

1.3. Thesis scope

As presented in the previous section piston rings have been studied extensively in order to characterize their performance in terms of conformability which plays a critical role in determining oil consumption, gas blow by and friction. Yet no complete ring design tool based on curved beam model has been developed yet. A straight beam based ring design tool was developed by Liu [30] based on the static analysis presented in his thesis. However this modeling does not include oil lubrication, variable gas pressure in the circumference direction and non-zero gap effects. Additionally, no model, whether based on curved or straight beam, determines the ring free shape and the force distribution in radial bore based on ring ovality or any final ring shape given any arbitrary radial force distribution. Moreover, conversions among ring's free shape, its ovality and the force distribution in radial bore have not been done yet and will be useful for ring designer in order to facilitate the design process and minimize the number of iterations required to obtain the desired ring properties.

Conformability should also be studied with the ability of modelling working engine conditions including the different lubrication cases, the gas pressure effect along with the groove and bore distortion and thermal moment effect. Besides, non-zero ring gap and variable oil distributions and gas pressures along the circumference should be modeled since these conditions can be encountered in working engine conditions.

As proven by Baelden [31], curved beam model resolved several issues existing in the straight beam model such as discontinuities of quantities of bending moment and curvature, and the singular behavior of the ring gap that can be studied with a higher degree of confidence. Hence, developing a static twist under fixed ID/OD constraint based on curved beam model is essential to conceive a complete ring design tool based solely on that modelling that allows us to reach a better accuracy with less computation cost than the straight beam model.

This thesis work is focusing on the top two rings but the methodology and the RDT developed can be extended to study the OCR.

Our model relies on a multi-scale meshing which is able to solve the ring structural deformation of the piston ring using a coarse mesh but considers the different interactions with the liner and piston on a finer contact grid. This method allows efficient coupling of structural deformation of the ring and contact forces at the ring-liner and ring-groove interfaces which occur at different length scales. As a result, contact and gas forces can be simulated taking into account relevant factors such as bore distortion or piston tilt.

In chapter 2 of this work, the ring geometry and the equations for its analysis based on the curved beam finite element is presented. We also present the modeling of closing the ring from its free shape to final radial one to simulate the process of introducing it inside the cylinder. At the end of that chapter we present the final matrix form equation modeling the ring's analysis that has to be solved in order to determine its conformability with the liner and piston and the different force distributions.

The conformability analysis is detailed in chapter 3. Contact and lubrication models for the ring-liner and ring groove interfaces are presented first. Piston secondary motion and the thermal moment resulting from the radial temperature gradient between the ID and OD are also studied to be included in our modelling. Finally, sample results are presented in order to show some of the key results obtained with the simulations carried out with our model such as the effect of the gap position with a distorted bore on the ring-liner conformability and the bending moment resulting from radial temperature gradient. Furthermore, the effect of local oil accumulation on liner and the ring-groove conformability are discussed as well.

The fourth chapter is devoted to the static twist under fixed ID/OD constraint modeling in which we extend the curved beam model in order to simulate the axial tapping force carried out in the experimental set-up in order to determine the ring static twist. The effect of the ring's symmetry along with sample results are presented.

In chapter 5, we present the four models developed to relate the ring's free shape, its ovality and force distribution in radial bore, which defines a complete tool that relates in any desired order these three ring's characterizations. A theoretical validation of these four models is presented by recovering the radial force distribution used first as an input and then recovered after being processed through all the four models. A validation of the model using ovality measurement is also presented and limitation of the results is also discussed.

Finally a summary of the thesis main results and tool developed can be found in chapter 6. A list of additions and area of possible improvement that would best complement this thesis work is given.

2. Curved beam finite element model of piston rings

Given their dimensions, piston rings can be considered as metallic beams. The size of their cross section is small compared to their radius. For instance a typical ring for a passenger car engine has a radius of around $40\ mm$ and a cross section of a height around $1.5\ mm$ and a radial width around $3\ mm$. This gives a ratio of cross section typical size by the radius below 0.1. Hence one can uses beam theory in order to characterize ring structural behavior. Timoshenko's book on materials strength [32] provides a complete treatment and overview of beam theory.

Like bore distortions, ring's deformations are of the order of $100\ \mu m$ and its length scale as mentioned previously is in the order of tens of millimeters which is determined by bore diameter primarily and bore distortion and piston tilt. However, ring-liner and ring-groove contact forces depend on the clearances which are within sub-micron level and the on boundary conditions like fuel-lube interaction and bridging which include length scales around $100\ \mu m$ and even lower. Therefore the classic straight beam description is not able to respect the local force generation and provide an accurate description of the structural deformation physics. For instance for the given orders of magnitude, straight beam based finite element method needs to reduce the grid size below $1\ mm$ in order to provide enough accurate prediction of ring-liner contact force. However, for this element size, the beam element is likely to not give an accurate description of the ring structural response since the ration between the length scale of cross-section sizes and the beam one is not small anymore and thus the beam theory is not valid anymore.

To address this problem and to couple ring deformations and its contact interaction with the piston and cylinder despite their different length scales, a dual grid curved beam finite element method was developed by Baelden [31] first and then used by Y. Liu [33] to successfully assemble a multi-scale-length ring pack model that provides an accurate description of a cycle model and all the relevant mechanisms taking part in it within a reasonable computation cost.

This curved beam finite element method takes advantage of the dual grid used for the ring's deformations and the contact force based on the typical length scales they rely on. Ring structural deformations are solved with sufficient accuracy using a coarse structural mesh and local interactions are studied based on a much finer grid. Therefore thanks to this separation this method is able to address the problem mentioned above by handling different length scales at the same time.

The derivation of the finite element equations for the different rings was developed in Baelden [31] and Y. Liu [33] works. We present here the calculation details for the sake of clarity and to have a more complete work and comprehensible model.

2.1. Review of ring differential geometry

Inside the engine, the piston ring is subject to in-plane and out of plane deformations along with its twist. These deformations result in bending and twisting moments which are proportional to changes of curvature and torsion of the ring's neutral axis. In this section we present a brief review of ring differential geometry in order to understand the development of curved beam finite element. For further details, Pressley [34] presented a more complete treatment of differential geometry of space curves.

Since the ring's neutral axis is expected to bend and twist in three dimensions, it should be treated as a 3D curve. Three different frames that will be used in the remaining parts of this work are introduced. below.

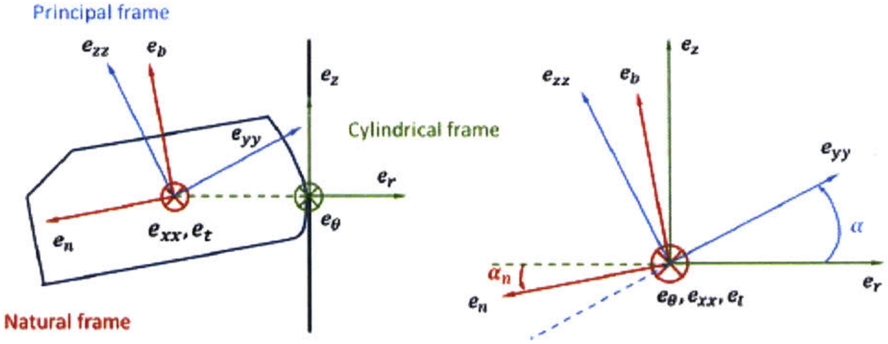

Figure 2.1 – Ring principle frame, Natural frame and Cylindrical frame

Based on the notation used in Figure 2.1, the cylindrical frame is attached to the piston liner. $\boldsymbol{e_r}$ is in the bore radius direction and pointing outward, $\boldsymbol{e_z}$ is in the axial direction and pointing upwards and $\boldsymbol{e_\theta}$ is directed along the circumferential direction. The natural frame is attached to the ring neutral axis and contains the normal unit vector $\boldsymbol{e_n}$, the binormal unit one $\boldsymbol{e_b}$ and the tangent unit vector $\boldsymbol{e_t}$. The definition and calculation of these three vectors is presented below. α_n is the orientation of the ring natural frame. The principal frame is defined by the two principle axes $\boldsymbol{e_{zz}}$ and $\boldsymbol{e_{yy}}$ that lie in the plane of the ring cross section and by the tangent unit vector $\boldsymbol{e_{xx}}$ which is perpendicular to the plane of the ring cross section. The principal frame is defined by three mutually perpendicular axes within a body about which the moment of inertia is maximum and the product of inertia of each pair of the three axes is zero.

This means that bending moments that are normal to a principal plane result in deformation of the beam neutral axis in that principal plane.

Any 3D curve C can be described in cylindrical coordinates by:

$$C(\theta): \boldsymbol{r}(\theta) = \rho(\theta)\boldsymbol{e_r} + z(\theta)\boldsymbol{e_z}\ (\theta_1 \leq \theta \leq \theta_2)$$

(2.1)

As shown in Figure 2.2, in (2.1), $\boldsymbol{r}$ refers to the position vector representing the curve, θ to the polar angle, ρ to the radial distance and z to the axial coordinate. Figure 2.2 also shows the natural frame of the curve C.

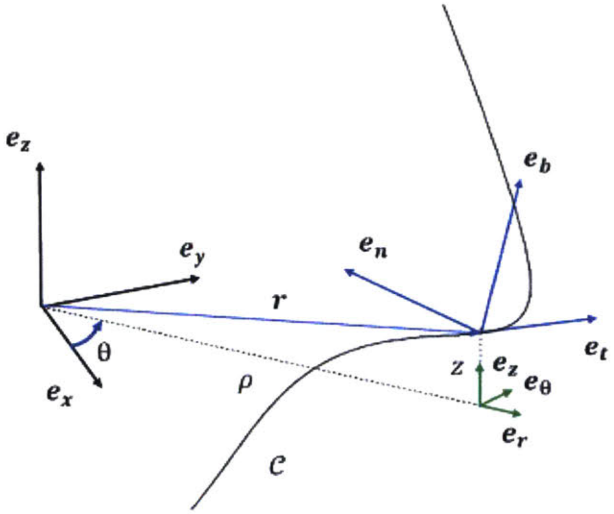

Figure 2.2 – Cylindrical and natural frames for a space curve

The curve unit tangent vector $\boldsymbol{e_t}$ is equal to the unit vector of the derivative of the position vector $\boldsymbol{r}(\theta)$ with respect to θ (2.2). For the rest of this thesis, the prime sign is used to refer to a derivation with respect to the polar angle θ.

$$\boldsymbol{e_t}(\theta) = \frac{\boldsymbol{r}'(\theta)}{\|\boldsymbol{r}'(\theta)\|} = \frac{\rho'\boldsymbol{e_r} + \rho\boldsymbol{e_\theta} + z'\boldsymbol{e_z}}{\sqrt{\rho^2 + \rho'^2 + z'^2}}$$

(2.2)

The unit normal vector $\boldsymbol{e_n}$ is equal to the unit vector of the second derivative of the position vector $\boldsymbol{r}(\theta)$ with respect to θ (2.3).

$$\boldsymbol{e_n}(\theta) = \frac{\boldsymbol{r}''(\theta)}{\|\boldsymbol{r}''(\theta)\|} = \frac{(\rho'' - \rho)\boldsymbol{e_r} + 2\rho'\boldsymbol{e_\theta} + z''\boldsymbol{e_z}}{\sqrt{(\rho'' - \rho)^2 + 2\rho'^2 + z''^2}}$$

(2.3)

The binormal vector $\boldsymbol{e_b}$ is normal to both $\boldsymbol{e_t}$ and $\boldsymbol{e_t}$ and forms a right hand coordinate system with them. It is equal to the cross product of $\boldsymbol{e_t}$ and $\boldsymbol{e_n}$ (2.4).

$$\boldsymbol{e_b}(\theta) = \boldsymbol{e_t}(\theta) \times \boldsymbol{e_n}(\theta)$$

(2.4)

The tangent of the angle α_n is equal to the ratio of the axial component of the normal vector to its radial one (2.5).

$$\tan(\alpha_n) = \frac{z''}{\rho'' - \rho}$$

(2.5)

The plane formed by the tangent and normal vectors $\boldsymbol{e_t}$ and $\boldsymbol{e_n}$ is called the osculating plane or plane of curvature of the curve C. Locally, C can be approximated by a planar curve which is contained in the osculating plane. The coordinates of a space curve can be recovered from its curvature κ and torsion τ. Curvature and torsion are measures of the local radius of curvature and twist of the curve respectively. The curvature is related to the differential variation of the unit tangent vector $\boldsymbol{e_t}$ (2.6).

$$\frac{d\boldsymbol{e_t}}{ds} = \kappa\boldsymbol{e_n}$$

(2.6)

The variable s here refers to the arc length of the curve C. Using the parametric expression of the position vector and the chain rule, the arc length of a differential element of C can be expressed as in equation (2.7).

$$ds(\theta) = \|\boldsymbol{r}'(\theta)\|d\theta = \sqrt{\rho^2 + \rho'^2 + z'^2}d\theta$$

(2.7)

The curvature represents the rate at which the tangent vector $\boldsymbol{e_t}$ is rotated towards the normal one as one moves along the curve C. It measures how much the curve is curved locally. A large curvature corresponds to an arc with a small radius of curvature.

Using equations (2.2), (2.3), (2.6) and (2.7), we can express the curvature as follows:

$$\kappa = \frac{\|r'' \times r'\|}{\|r'\|^3} = \frac{\sqrt{[\rho z'' - 2\rho' z']^2 + [(\rho'' - \rho)z' - \rho' z'']^2 + [\rho(\rho - \rho'') + 2\rho'^2]^2}}{[\rho^2 + \rho'^2 + z'^2]^{\frac{3}{2}}}$$

(2.8)

For planar curve, the axial coordinate z and its derivatives can be removed from (2.8) to obtain the expression of the curvature in polar coordinates (2.9).

$$\kappa = \frac{|\rho^2 + 2\rho'^2 - \rho\rho''|}{(\rho^2 + \rho'^2)^{\frac{3}{2}}}$$

(2.9)

Besides curvature, space curves are twisted which make them leave the osculating plane. Torsion is a measure of the rate at which the space curve twist which is the rotation rate of the binormal vector along the curve C. It is calculated from the differential variation of the unit normal vector $\boldsymbol{e_b}$ (2.10).

$$\frac{d\boldsymbol{e_b}}{ds} = -\tau \boldsymbol{e_n}$$

(2.10)

Using equations (2.3), (2.4), (2.7) and (2.10), we can express the torsion as follows:

$$\tau = \frac{(r' \times r'').r'''}{\|r'' \times r'\|^2}$$

$$= \frac{[\rho z'' - 2\rho' z'][\rho^{(3)} - 3\rho'] + [3\rho'' - \rho][(\rho'' - \rho)z' - \rho' z''] + z^{(3)}[\rho(\rho - \rho'') + 2\rho'^2]}{[\rho z'' - 2\rho' z']^2 + [(\rho'' - \rho)z' - \rho' z'']^2 + [\rho(\rho - \rho'') + 2\rho'^2]^2}$$

(2.11)

The ring neutral axis is determined by the position vector $\boldsymbol{r}$ which can be written as a function of the nominal ring radius R, the radial displacement y and the axial displacement z (2.12).

$$\boldsymbol{r} = (R + y)\boldsymbol{e_r} + z\boldsymbol{e_z}$$

(2.12)

The general expressions of curvature (2.8) and torsion (2.11) for space curves in cylindrical coordinates are non-liner and depend on relative large number of variables (coordinates and their derivatives). However we can seek to obtain simpler relations using some relevant approximations. Under the action of ring tension, gas pressure and inertia, piston rings deform to adapt to the groove and cylinder geometry once they are assembled inside the engine. Hence, ring neutral axis displacements in the axial and radial directions are of the same order of piston and cylinder deformations and piston displacement. For typical passenger car engines, the bore radius in around $40\ mm$ and the bore distortion is on the order of $100\ \mu m$. The piston land/groove deformation and piston secondary motion in radial direction do not generally constrain the rind displacement. The piston land and groove deformation in axial direction are on the order of $10\ \mu m$. The piston displacement due to secondary motion in axial direction is on the order of $100\ \mu m$. Therefore, both axial and radial directions are expected to be much smaller than the ring nominal radius. Due to ring stiffness, ring radial and axial displacement cannot change too rapidly. Hence we can assume that the derivatives of the axial and radial displacements of the ring neutral axis are taken of the same order as the axial and radial displacements respectively. This leads to the called small displacement assumption (2.13):

$$\frac{y}{R} \sim \frac{y'}{R} \sim \frac{y''}{R} \ll 1$$

$$\frac{z}{R} \sim \frac{z'}{R} \sim \frac{z''}{R} \ll 1$$

(2.13)

Using this assumption, simplified expressions of the curvature (2.14) and the torsion (2.15) can be obtained from the general ones (2.8) and (2.11) respectively:

$$\kappa = \frac{1}{R} - \frac{y + y''}{R^2}$$

(2.14)

$$\tau = \frac{z' + z^{(3)}}{R^2}$$

(2.15)

The small displacement assumption (2.13) can also be applied to simplify the expression (2.5) of the orientation of the neutral frame (2.16):

$$\alpha_n = -\frac{z''}{R}$$

(2.16)

The small displacement assumption is valid provided the rings are already assembled into the engine. However, this assumption is violated for the top two rings when closing them from their free shape to the nominal radius circular one since their radial displacement is on the order of several millimeters. Hence y cannot be considered much smaller than the nominal radius R.

2.2. Spline interpolation of ring geometry with Hermite polynomials

The first step in developing the curved beam finite element is discretizing the ring neutral axis geometry. The ring neutral axis is a continuous curve which is free to take any shape when it is deformed. Using spline interpolation, we can discretize it into a number of finite elements. Using carefully chosen shape functions, in order to obtain enough accuracy of the ring neutral axis geometry, this latter is interpolated from the nodal values of displacements and their derivatives. An example of spline interpolation of the ring radial displacement is presented in Figure 2.3.

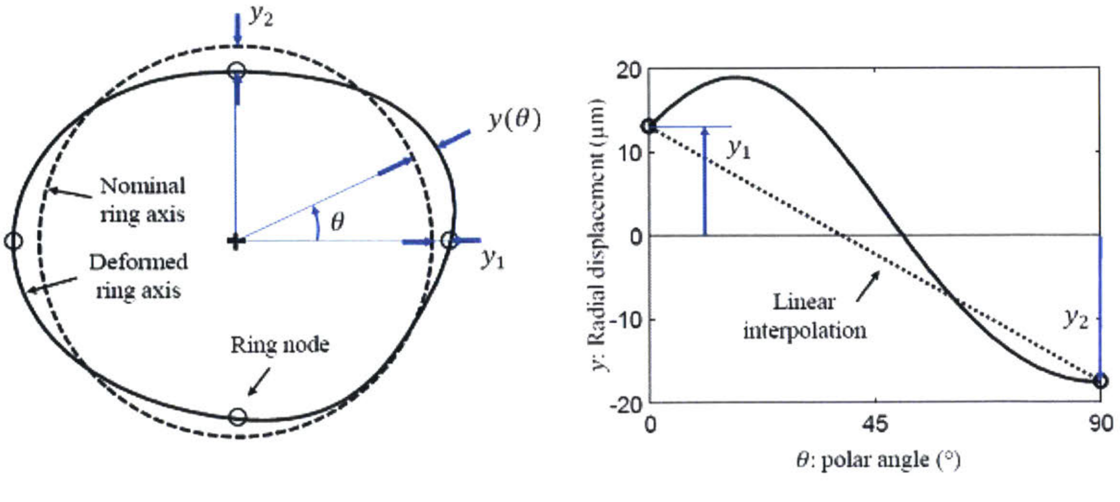

Figure 2.3 – Spline interpolation of ring radial displacement

In the right picture of Figure 2.3, the ring radial deformation (solid line) is approximated by a linear function (dotted line) which matches the actual deformation at node 1 and 2 located at the polar angles $\theta = 0°$ and $\theta = 90°$ respectively (2.17).

$$y(\eta) = y_1 + \eta(y_2 - y_1)$$

(2.17)

The interpolating function (2.17) is expressed as a function of the isoparametric variable η defined in equation (2.18).

$$\eta = \frac{\theta}{\theta_e}$$

(2.18)

In the last equation, θ_e is the angular length of a ring element. The isoparametric variable definition makes η vary linearly from $\eta = 0$ at node 1 to $\eta = 1$ at node 2. We can see the interpolation function (2.17) as a sum of two first order polynomials (2.19).

$$y(\eta) = (1 - \eta)y_1 + \eta y_2 = N_1 y_1 + N_2 y_2$$

(2.19)

In this equation, N_1 and N_2 are the shape functions of the ring element associated with the nodal displacements y_1 and y_2. (2.19) corresponds to a first order Hermitian interpolation of the ring radial displacement. The ring can be divided into several elements with each element associated with its own interpolation function defined by the displacements and the derivatives at its two nodes. When these functions are assembled together, we can recover the deformation of the ring around the entire circumference. By using first order Hermite polynomials, the continuity of the radial displacement at the nodes is guaranteed. Using (2.17) we can see that by definition $y(0) = y_1$ and $y(1) = y_2$. Higher order Hermite polynomials can be used if we want to guarantee the continuity of the derivatives of the interpolated functions. Using higher orders leads to higher interpolation accuracy but also to more nodal displacements.

To be interpolated, the ring deformation can be broken down into three components: the radial and axial displacements of the neutral axis and the orientation of the cross section (Figure 2.4).

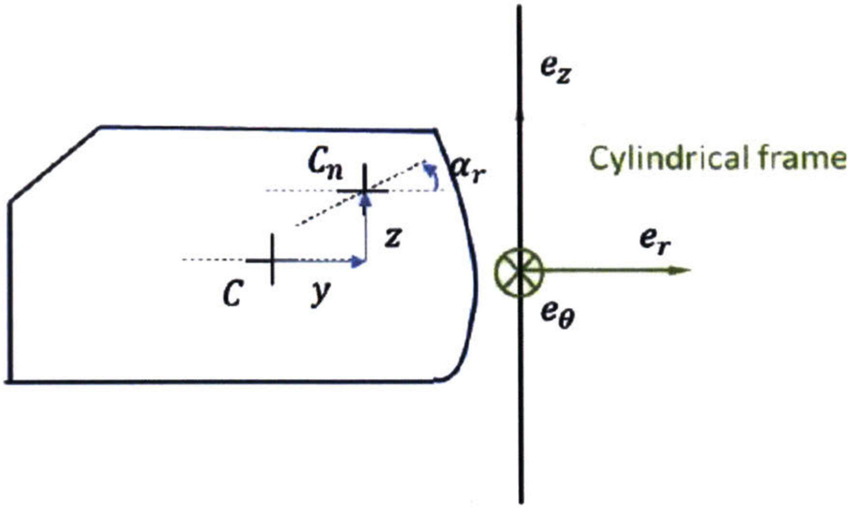

Figure 2.4 – Ring deformation: neutral axis displacement and cross section orientation

Baelden [31] developed the Hermite polynomial shape functions that we will use in the curved beam finite element method to interpolate the three components of the ring deformation. The radial and axial displacement of the ring neutral axis are interpolated using 5th order Hermite polynomial spline in order to guarantee the continuity of these displacements up to their second derivative. Hence the continuity of the curvature, which is the key variable for bending, follows. To carry out 5th order interpolation of the ring geometry deformation, nodal displacements must include the displacement, its first and second derivatives (Figure 2.5).

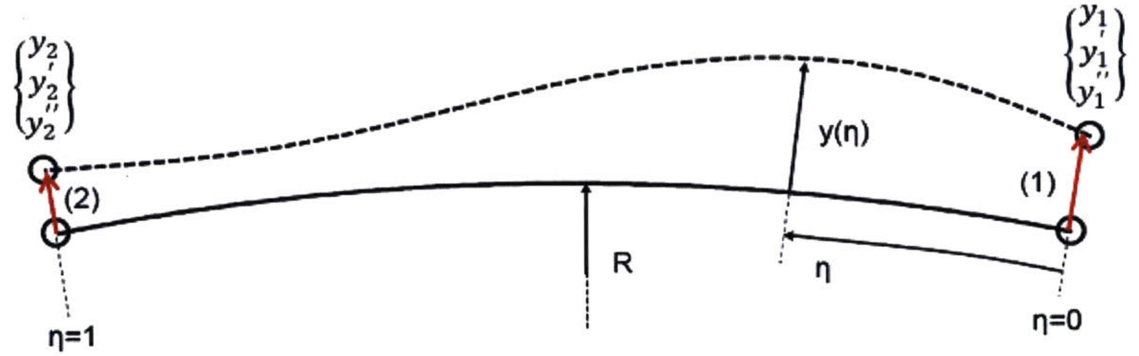

Figure 2.5 – Spline interpolation of ring radial displacement

$$y(\eta) = \sum_{k=1}^{6} N_k(\eta) u_{yk} \text{ where } \{u_y\} = \{u_{y1} \dots u_{y6}\}^T = \{y_1, y_1', y_1'', y_2, y_2', y_2''\}^T$$

(2.20)

$$z(\eta) = \sum_{k=1}^{6} N_k(\eta) u_{zk} \text{ where } \{u_z\} = \{u_{z1} \dots u_{z6}\}^T = \{z_1, z_1', z_1'', z_2, z_2', z_2''\}^T$$

(2.21)

The 5th order interpolation uses six shape functions $(N_k)_{k=1}^{k=6}$. The calculation details related to the determination of these shape functions can be found in Baelden thesis [29]. The resulting expressions are listed below.

$$N_1 = 1 - 10\eta^3 + 15\eta^4 - 6\eta^5$$

(2.22)

$$N_2 = \theta_e(\eta - 6\eta^3 + 8\eta^4 - 3\eta^5)$$

(2.23)

$$N_3 = \theta_e^2(\frac{\eta^2}{2} - \frac{3}{2}\eta^3 + \frac{3}{2}\eta^4 - \frac{\eta^5}{2})$$

(2.24)

$$N_4 = 10\eta^3 - 15\eta^4 + 6\eta^5$$

(2.25)

$$N_5 = \theta_e(-4\eta^3 + 7\eta^4 - 3\eta^5)$$

(2.26)

$$N_6 = \theta^2(\frac{\eta^3}{2} - \eta^4 + \frac{\eta^5}{2})$$

(2.27)

The first and second order derivatives of the displacement within each element can be calculated by deriving the shape functions and their expression are listed below.

$$y'(\eta) = \sum_{k=1}^{6} N_k'(\eta) u_{yk}$$

(2.28)

$$y''(\eta) = \sum_{k=1}^{6} N_k''(\eta) u_{yk}$$

(2.29)

$$z'(\eta) = \sum_{k=1}^{6} N_k'(\eta) u_{zk}$$

(2.30)

$$z''(\eta) = \sum_{k=1}^{6} N_k'(\eta) u_{zk}$$

(2.31)

Since the twisting moment is proportional to the derivative of the twist angle, a 3rd order polynomial interpolation is sufficient and requires only ring twist and its first derivative at the nodes (2.32).

$$\alpha_r(\eta) = \textstyle\sum_{k=1}^{4} N_{\alpha k}(\eta) u_{\alpha k} \text{ where } \{u_\alpha\} = \{u_{\alpha 1} \ldots u_{\alpha 4}\}^T = \{\alpha_{r1}, \alpha_{r1}', \alpha_{r2}, \alpha_{r2}'\}^T$$

(2.32)

The fours shape functions derived by Baelden [29] are listed below.

$$N_{\alpha 1} = 1 - 3\eta^2 + 2\eta^3$$

(2.33)

$$N_{\alpha 2} = \theta_e(\eta - 2\eta^2 + \eta^3)$$

(2.34)

$$N_{\alpha 3} = 3\eta^2 - 2\eta^3$$

(2.35)

$$N_{\alpha 4} = \theta_e(-\eta^2 + \eta^3)$$

(2.36)

The first order derivative of the twist angle within each element can be calculated by deriving the shape functions (2.37).

$$\alpha_r'(\eta) = \sum_{k=1}^{4} N_{\alpha k}'(\eta) u_{\alpha k}$$

(2.37)

This discretization of the ring deformation leads to 8 degrees of freedom per node: 3 for radial displacements, 3 for axial displacements and 2 for twist. All nodal displacements are assembled in one displacement vector (2.38).

$$\{u_k\} = \{y_k, y_k', y_k'', z_k z_k', z_k'', \alpha_{rk}, \alpha_{rk}'\}^T$$

(2.38)

2.3. Euler-Lagrange equations for ring's analysis

Baelden [31] derived the finite element equations of the piston ring model using Hamilton's principle. The Lagrangian L of any system is defined as the combination of its kinetic energy T, its strain energy U and the work of external forces applied on it W (2.39).

$$L = T + W - U$$

(2.39)

The Euler-Lagrange equations are obtained using the Hamilton's principle (2.40).

$$\frac{\partial}{\partial t}\left(\frac{\partial L}{\partial \dot{u}_i}\right) - \frac{\partial L}{\partial u_i} = 0 \text{ for } i = \{1 \dots n\}$$

(2.40)

The variable u_i represents the ith nodal displacement of the discretized ring and $\dot{u}_i$ the nodal speed. Each of them is a degree of freedom that defines the state of the system. Hamilton's principle can be applied to each element of the piston ring. First the kinetic energy, strain energy and work of external of forces applied on the ring must be calculated.

The motion of the ring cross section can be divided in three parts: the translations in the radial and axial directions and the rotation around the ring neutral axis. The ring neutral axis displacements (y, z, α) are measured in the reference frame of the piston. The zero displacement position corresponds to a ring centered in the piston groove and contacting a perfectly round cylinder. The kinetic energy of the ring element is calculated by integrating the kinetic energy of cross sections along the ring neutral axis (2.42).

$$dT^{(e)} = \frac{1}{2}\rho\left[A(\dot{y}^2 + \dot{z}^2) + I_p \dot{\alpha_r}^2\right]ds$$

(2.41)

$$T^{(e)} = \frac{1}{2}\int_0^{L_e} \rho\left[A(\dot{y}^2 + \dot{z}^2) + I_p \dot{\alpha_r}^2\right]ds$$

(2.42)

The notation e is used to refer to the ring element, for instance $T^{(e)}$ represents the kinetic energy of the ring element. The integration is carried out over the length of the ring element L_e. The density of the ring material is ρ, I_p is the polar moment of inertia of the cross section and A refers to the cross section area.

Strain energy is stored in the ring structure due to its deformation and is derived using the ring's bending and twisting moments along the curvature change and twist angle.

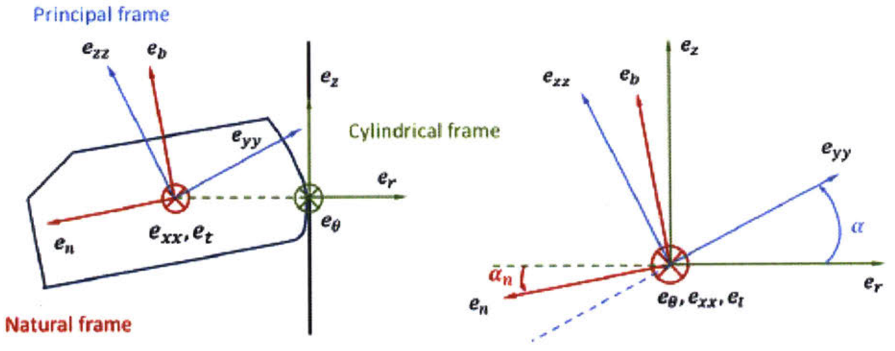

Figure 2.6 – Ring principle frame, Natural frame and Cylindrical frame

The curvature of the ring neutral axis falls in the plane fromed by the vectors $\boldsymbol{e_b}$ and $\boldsymbol{e_n}$ and aligns with the vector $\boldsymbol{e_t}$. In section 2.1, we proved that (2.16) $\alpha_n \approx -\frac{z''}{R}$. Therefore, we can derive the following expressions for the curvature corresponding to the radial and axial displacements.

$$\kappa_{yy} = \kappa\cos(\alpha - \alpha_n) = \kappa\cos\left(\alpha + \frac{z''}{R}\right)$$

(2.43)

$$\kappa_{zz} = \kappa \sin(\alpha - \alpha_n) = \kappa \sin\left(\alpha + \frac{z''}{R}\right)$$

(2.44)

The bending moment along the $\boldsymbol{e}_{zz}$ direction is proportional to the curvature change in the $\boldsymbol{e}_{yy}$ direction (2.45) and the bending moment in the $\boldsymbol{e}_{yy}$ is proportional to the curvature change in the $\boldsymbol{e}_{zz}$ direction (2.46). The ring twist angle contains two components (2.47): the torsion of the ring neutral axis τ and the rotation of the ring section per unit length $\frac{d}{ds}(\alpha_n - \alpha)$ as proved in Baelden thesis [29].

$$M_{zz} = EI_{zz}\left(\kappa_{yy} - \kappa_{yy0}\right)$$

(2.45)

$$M_{yy} = EI_{yy}(\kappa_{zz} - \kappa_{zz0})$$

(2.46)

$$M_{\theta} = GJ_t\left[\tau + \frac{d}{ds}(\alpha_n - \alpha)\right]$$

(2.47)

The strain energy of the ring element contains three components (2.54): the strain energy related to in plane bending (2.49), to out of plane bending (2.51) and to torsion (2.53). Each component is the integration of the corresponding contribution to the strain energy of the cross sections along the ring neutral axis (2.48), (2.50) and (2.52).

$$dU_{zz}^{(e)} = \frac{1}{2}M_{zz}\left(\kappa_{yy} - \kappa_{yy0}\right)ds = \frac{1}{2}EI_{zz}\left(\kappa_{yy} - \kappa_{yy0}\right)^2 ds$$

(2.48)

$$U_{zz}^{(e)} = \frac{1}{2}\int_0^{L_e} EI_{zz}\left(\kappa_{yy} - \kappa_{yy0}\right)^2 ds$$

(2.49)

$$dU_{yy}^{(e)} = \frac{1}{2}M_{yy}(\kappa_{zz} - \kappa_{zz0})ds = \frac{1}{2}EI_{yy}(\kappa_{zz} - \kappa_{zz0})^2 ds$$

(2.50)

$$U_{yy}^{(e)} = \frac{1}{2}\int_0^{L_e} EI_{yy}(\kappa_{zz} - \kappa_{zz0})^2 ds$$

(2.51)

$$dU_\theta^{(e)} = \frac{1}{2}M_\theta\left[\tau + \frac{d}{ds}(\alpha_n - \alpha)\right]ds = \frac{1}{2}GJ_t\left[\tau + \frac{d}{ds}(\alpha_n - \alpha)\right]^2 ds$$

(2.52)

$$U_\theta^{(e)} = \frac{1}{2}\int_0^{L_e} GJ_t\left[\tau + \frac{d}{ds}(\alpha_n - \alpha)\right]^2 ds$$

(2.53)

$$U^{(e)} = U_{zz}^{(e)} + U_{yy}^{(e)} + U_\theta^{(e)}$$

(2.54)

In order to complete the calculation of the piston ring Lagrangian, we need to compute the work of external forces. During engine operation, the ring is subject to the action of external forces making it deform and move with the piston groove. Ring tension forces the ring against the cylinder liner. Depending on the lubrication conditions, the liner apply a normal force and a friction one on the ring. Acceleration or deceleration of the piston pushes the ring against the upper or lower flank of the piston groove and another force contact is created between the ring and the groove. Pressurized piston grooves and lands result in axial and radial forces acting on the ring. Cross section resulting radial force f_r, axial force f_z and twisting moment m_θ shown in Figure 2.7 must be calculated to take into account all external forces. The calculation and resulting expressions of these forces will be derived in the next chapters. The quantities f_r, f_z and m_θ are forces and moment per unit length respectively.

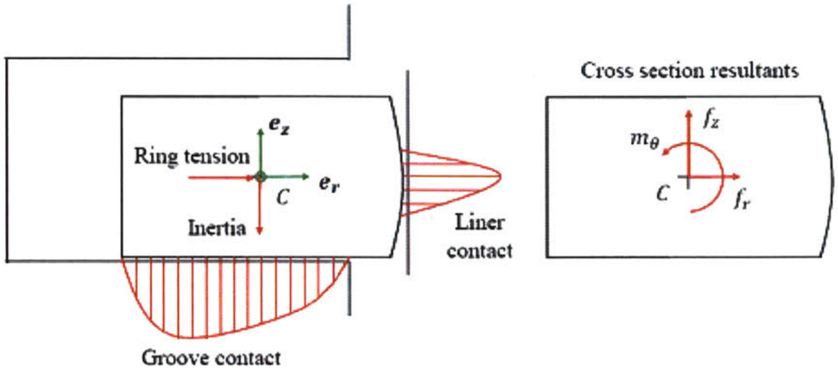

Figure 2.7 – External forces on ring cross section

The work of external forces is obtained by multiplying the cross section external forces with the corresponding displacements and integrating over the length of the ring element (2.55).

$$W^{(e)} = \int_0^{L_e} (f_r y + f_z z + m_t \alpha) ds$$

(2.55)

Applying (2.39) and (2.40) to the ring element, we obtain its Lagrangian (2.56) and its Euler-Lagrange equations (2.57):

$$L^{(e)} = T^{(e)} + W^{(e)} - U^{(e)}$$

(2.56)

$$\frac{\partial}{\partial t}\left(\frac{\partial L^{(e)}}{\partial \dot{u}_i}\right) - \frac{\partial L^{(e)}}{\partial u_i} = 0 \text{ for } i = \{1 \dots n\}$$

(2.57)

The variable u_i represents the ith degree of freedom of the system composed by the two nodes of the ring element and when assembled in one vector, form the displacements and their derivatives at those nodes (2.58). Subscripts 1 and 2 refer to the first and second node of the element respectively.

$$u^{(e)} = \{u_1, \dots, u_{16}\} = \{y_1, y_1', y_1'', z_1, z_1', z_1'', \alpha_1, \alpha_1', y_2, y_2', y_2'', z_2, z_2', z_2'', \alpha_2, \alpha_2'\}$$

(2.58)

(2.57) gives a matrix equation in $u^{(e)}$. When all the elements' matrices are assembled, we obtain a matrix equation to solve in order to obtain all the degrees of freedom of the ring (8 per node) and thus the full characterization of the ring state.

2.4. Ring gap closing

The simplified expressions of the curvature and torsion of the ring neutral axis (2.14) and (2.15) respectively are only valid under the assumption of small displacements. As mentioned previously, this assumption is violated when top two rings are closed from their free shape to the nominal bore radius radial state. During this process, the ring neutral axis is a planar curve and its axial displacement is zero but the radial displacement is in the order of several millimeters and cannot be assumed small. Therefore, we need to use the general expression of a planar curve (2.9) to calculate the curvature (2.59).

$$\kappa_{fs} = \frac{\left|r_{fs}^2 + 2r_{fs}'^2 - r_{fs}r_{fs}''\right|}{\left(r_{fs}^2 + r_{fs}'^2\right)^{\frac{3}{2}}}$$

(2.59)

In this equation, r_{fs} is the radial coordinate of each point of the ring, defined as the distance between that point and the center of the circle adjacent to the ring free shape at the point located at its back with a radius equal to the nominal bore radius (Figure 2.8).

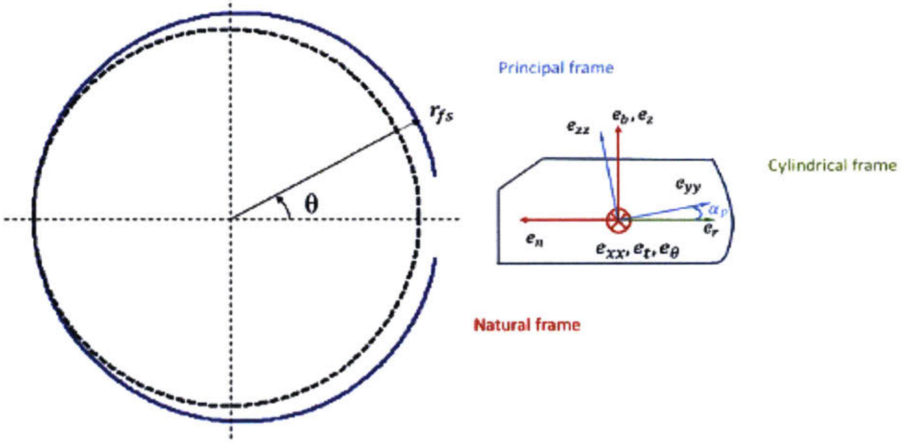

Figure 2.8 – Ring free shape and radial coordinate system

The calculation of the curvature change directly from the free shape state to the final state once the ring is subject to all the external forces inside the engine will be very complicated and non-linear. In order to simplify this calculation, we divide the process modeling into two parts: we close the ring from its free shape to the nominal radius circular state without twist (intermediate state), and then we model the curvature change with respect to the intermediate state introduced. For the second part, we can take advantage of the small displacement assumption.

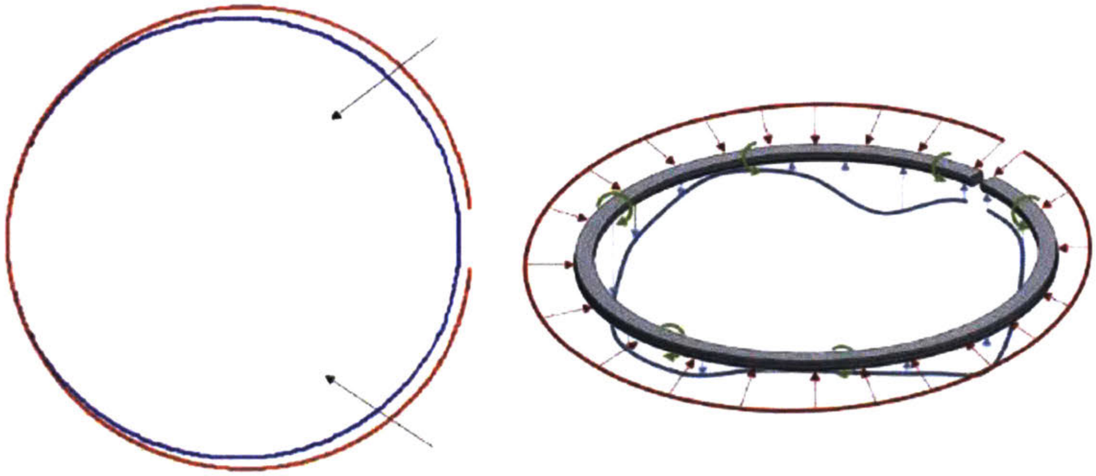

Figure 2.9 – Intermediate state and required preload

The left plot of Figure 2.9 shows the ring free shape (red line) and its close round shape (blue line, assuming there is no gap between the ring tips). The right plot demonstrates the required preload to close the ring from its free shape to its round shape. These preload will be considered later as initial forces in our model. Depending on the ring cross section symmetry, these preload can only be in the radial direction or they can include axial forces and twisting moments.

We apply Euler-Lagrange equations to determine the required preload to close the ring from its free shape to its round one. As demonstrated in Figure 2.8, due to the asymmetry of the ring's cross section, the principal and cylindrical frames do not align at the ring free state and the orientation angle α_p is called principal angle. Using Figure 2.6 and Figure 2.8 representing the different frames, we can derive the relation relating the ring cross section twist, the principal angle and the orientation angle of the natural frame (2.60).

$$\alpha_r = \alpha - \alpha_p$$

(2.60)

The curvature and torsion at the free state are determined as below.

$$\kappa_{yy0} = \kappa_{fs}\cos(\alpha_p)$$

(2.61)

$$\kappa_{zz0} = \kappa_{fs}\sin(\alpha_p)$$

(2.62)

$$\tau_0 = 0$$

(2.63)

$$\alpha_0 = \alpha_p$$

(2.64)

$$\alpha_{n0} = 0$$

(2.65)

Once the ring is closed at its nominal radius, the assumption of small displacement in both radial and axial directions is valid and (2.14) and (2.16) can be used.

$$\alpha_n \approx -\frac{z''}{R}$$

(2.14)

$$\kappa \approx \frac{1}{R} - \frac{y + y''}{R^2}$$

(2.16)

The curvature and torsion at the final state are calculated as follows using (2.14) and (2.15).

$$\kappa_{yy} = \kappa\cos(\alpha - \alpha_n) = \left(\frac{1}{R} - \frac{y + y''}{R^2}\right)\cos\left(\alpha + \frac{z''}{R}\right)$$

(2.66)

$$\kappa_{zz} = \kappa\sin(\alpha - \alpha_n) = \left(\frac{1}{R} + \frac{y + y''}{R^2}\right)\sin\left(\alpha + \frac{z''}{R}\right)$$

(2.67)

$$\tau = \frac{z' + z^{(3)}}{R^2}$$

(2.68)

Therefore, at the final state the three components of the strain energy (2.49), (2.51) and (2.53) can be expressed as below.

$$U_{zz}^{(e)} = \frac{1}{2}\int_0^{L_e} EI_{zz}\left(\kappa_{yy} - \kappa_{yy0}\right)^2 ds = \frac{L_e EI_{zz}}{2}\int_0^1 \left(\left(\frac{1}{R} - \frac{y + y''}{R^2}\right)\cos\left(\alpha + \frac{z''}{R}\right) - \kappa_{fs}\cos\left(\alpha_p\right)\right)^2 d\eta$$

(2.69)

$$U_{yy}^{(e)} = \frac{1}{2}\int_0^{L_e} EI_{yy}(\kappa_{zz} - \kappa_{zz0})^2 ds = \frac{L_e EI_{yy}}{2}\int_0^1 \left(\left(\frac{1}{R} - \frac{y + y''}{R^2}\right)\sin\left(\alpha + \frac{z''}{R}\right) - \kappa_{fs}\sin\left(\alpha_p\right)\right)^2 d\eta$$

(2.70)

$$U_{\theta}^{(e)} = \frac{1}{2}\int_0^{L_e} GJ_t\left(\tau + \frac{d}{ds}(\alpha_n - \alpha)\right)^2 ds = \frac{L_e GJ_t}{2}\int_0^1 \left(\frac{z' - R\alpha'}{R^2}\right)^2 d\eta$$

(2.71)

$$U^{(e)} = U_{zz}^{(e)} + U_{yy}^{(e)} + U_{\theta}^{(e)}$$

(2.54)

As introduced in section 2.2, the ring displacements can be interpolated using Hermite polynomials and the nodal displacements at the two nodes for each element as rewritten below.

$y(\eta) = \sum_{k=1}^{6} N_k(\eta) u_{yk}$ where $\{u_y\} = \{u_{y1} \dots u_{y6}\}^T = \{y_1, y_1', y_1'', y_2, y_2', y_2''\}^T$

(2.20)

$z(\eta) = \sum_{k=1}^{6} N_k(\eta) u_{zk}$ where $\{u_z\} = \{u_{z1} \dots u_{z6}\}^T = \{z_1, z_1', z_1'', z_2, z_2', z_2''\}^T$

(2.21)

$\alpha_r(\eta) = \sum_{k=1}^{4} N_{\alpha k}(\eta) u_{\alpha k}$ where $\{u_\alpha\} = \{u_{\alpha 1} \dots u_{\alpha 4}\}^T = \{\alpha_{r1}, \alpha_{r1}', \alpha_{r2}, \alpha_{r2}'\}^T$

(2.32)

Each ring element has two nodes and therefore 16 nodal displacements, 8 degree of freedoms per node. The displacement vector for an element is rewritten below.

$$u^{(e)} = \{u_1, \dots, u_{16}\} = \{y_1, y_1', y_1'', z_1, z_1', z_1'', \alpha_1, \alpha_1', y_2, y_2', y_2'', z_2, z_2', z_2'', \alpha_2, \alpha_2'\}$$

(2.58)

To select the appropriate shape function corresponding to the k^th nodal displacement within a ring element, we use the mapping function given below.

$$k_y = [1,2,3,9,10,11]$$

(2.72)

$$k_z = [4,5,6,12,13,14]$$

(2.73)

$$k_\alpha = [7,8,15,16]$$

(2.74)

$$k \longmapsto m(k)$$

$$[1,2,3,4,5,6,7,8,9,10,11,12,13,14,15,16] \longmapsto [1,2,3,1,2,3,1,2,4,5,6,4,5,6,3,4]$$

(2.75)

Using this mapping function, (2.20), (2.21) and (2.32) can be rewritten in a more compact form as follows.

$$y(\eta) = \sum_{k_y} N_{m(k_y)}(\eta) u_{k_y}$$

(2.76)

$$z(\eta) = \sum_{k_z} N_{m(k_z)}(\eta) u_{k_z}$$

(2.77)

$$\alpha_r(\eta) = \sum_{k_\alpha} N_{m(k_\alpha)}(\eta) u_{k_\alpha}$$

(2.78)

In order to apply the Hamilton's principle to the particular expressions of the strain energy components derived in (2.69), (2.70) and (2.71), we compute the derivatives of those quantities with respect to the different nodal displacements and their derivatives as presented in (2.79), (2.80) and (2.81).

$$\frac{\partial U^{(e)}}{\partial u_{k_y}} = \frac{\partial U^{(e)}_{zz}}{\partial u_{k_y}} + \frac{\partial U^{(e)}_{yy}}{\partial u_{k_y}}$$

$$= -L_e E I_{zz} \int_0^1 \left(\kappa_{yy} - \kappa_{yy0}\right) \frac{\cos\left(\alpha + \frac{z''}{R}\right)}{R^2} \left(N_{m(k_y)} + N''_{m(k_y)}\right) d\eta$$

$$-L_e E I_{yy} \int_0^1 (\kappa_{zz} - \kappa_{zz0}) \frac{\sin\left(\alpha + \frac{z''}{R}\right)}{R^2} \left(N_{m(k_y)} + N''_{m(k_y)}\right) d\eta$$

(2.79)

$$\frac{\partial U^{(e)}}{\partial u_{k_z}} = \frac{\partial U^{(e)}_{zz}}{\partial u_{k_z}} + \frac{\partial U^{(e)}_{yy}}{\partial u_{k_z}} + \frac{\partial U^{(e)}_{\theta}}{\partial u_{k_z}}$$

$$= L_e E I_{zz} \int_0^1 \left(\kappa_{yy} - \kappa_{yy0}\right) \left[-\frac{1}{R} + \frac{y + y''}{R^2}\right] sin\left(\alpha + \frac{z''}{R}\right) \frac{N''_{m(k_z)}}{R} \, d\eta$$

$$+L_e E I_{yy} \int_0^1 (\kappa_{zz} - \kappa_{zz0}) \left[\frac{1}{R} - \frac{y + y''}{R^2}\right] cos\left(\alpha + \frac{z''}{R}\right) \frac{N''_{m(k_z)}}{R} \, d\eta + L_e G J_t \int_0^1 \frac{(z' - R\alpha')}{R^2} \frac{N'_{m(k_z)}}{R} \, d\eta$$

(2.80)

$$\frac{\partial U^{(e)}}{\partial u_{k_\alpha}} = \frac{\partial U^{(e)}_{zz}}{\partial u_{k_\alpha}} + \frac{\partial U^{(e)}_{yy}}{\partial u_{k_\alpha}} + \frac{\partial U^{(e)}_{\theta}}{\partial u_{k_\alpha}}$$

$$= L_e E I_{zz} \int_0^1 \left(\kappa_{yy} - \kappa_{yy0}\right) \left[-\frac{1}{R} + \frac{y + y''}{R^2}\right] sin\left(\alpha + \frac{z''}{R}\right) \frac{N'_{\alpha m(k_\alpha)}}{R} \, d\eta$$

$$+L_e E I_{yy} \int_0^1 (\kappa_{zz} - \kappa_{zz0}) \left[\frac{1}{R} - \frac{y + y''}{R^2}\right] cos\left(\alpha + \frac{z''}{R}\right) \frac{N'_{\alpha m(k_\alpha)}}{R} \, d\eta$$

$$+ L_e G J_t \int_0^1 \frac{(z' - R\alpha')}{R^2} \left(-\frac{N'_{\alpha m(k_\alpha)}}{R}\right) d\eta$$

(2.81)

We obtain the required load to close the ring gap without any out of plane bending nor twist by substituting (2.79), (2.80) and (2.81) into Euler-Lagrange equation which gives the following initial load components.

$$F_{initial,k_y}^{(e)} = \frac{\partial U^{(e)}}{\partial u_{k_y}}\Big|_{\substack{y=0,y'=0,y''=0\\ z=0,z'=0,z''=0\\ \alpha=\alpha_p,\alpha'=0}}$$

$$= -L_e EI_{zz}\int_0^1 \left(\frac{1}{R}-\kappa_{fs}\right)\frac{\cos^2(\alpha_p)}{R^2}\left(N_{m(k_y)}+N''_{m(k_y)}\right)d\eta$$

$$-L_e EI_{yy}\int_0^1 \left(\frac{1}{R}-\kappa_{fs}\right)\frac{\sin^2(\alpha_p)}{R^2}\left(N_{m(k_y)}+N''_{m(k_y)}\right)d\eta$$

(2.82)

$$F_{initial,k_z}^{(e)} = \frac{\partial U^{(e)}}{\partial u_{k_z}}\Big|_{\substack{y=0,y'=0,y''=0\\ z=0,z'=0,z''=0\\ \alpha=\alpha_p,\alpha'=0}}$$

$$= -L_e EI_{zz}\int_0^1 \left(\frac{1}{R}-\kappa_{fs}\right)\frac{cos(\alpha_p)\sin(\alpha_p)}{R^2}N''_{m(k_z)}d\eta + L_e EI_{yy}\int_0^1 \left(\frac{1}{R}-\kappa_{fs}\right)\frac{sin(\alpha_p)\cos(\alpha_p)}{R^2}N''_{m(k_z)}d\eta$$

(2.83)

$$F_{initial,k_\alpha}^{(e)} = \frac{\partial U^{(e)}}{\partial u_{k_\alpha}}\Big|_{\substack{y=0,y'=0,y''=0\\ z=0,z'=0,z''=0\\ \alpha=\alpha_p,\alpha'=0}}$$

$$= -L_e EI_{zz}\int_0^1 \left(\frac{1}{R}-\kappa_{fs}\right)\frac{cos(\alpha_p)\sin(\alpha_p)}{R^2}N'_{\alpha m(k_\alpha)}d\eta + L_e EI_{yy}\int_0^1 \left(\frac{1}{R}-\kappa_{fs}\right)\frac{sin(\alpha_p)\cos(\alpha_p)}{R^2}N'_{\alpha m(k_\alpha)}d\eta$$

(2.84)

Once we derived these required forces to close the ring to its nominal radius, we can solve the ring deformations starting from this intermediate state by applying these required loads as preloads or initial forces $\{F_{initial}\}$.

2.5. Derivation of stiffness and load matrices

Very similarly to the study conducted by Baelden [31] on twin land oil control ring, in this section we will develop the stiffness and load finite element matrices for the top two rings. We do not focus on the mass matrix here since our study is carried out for the static case. Once we apply the initial load derived in the latter section, the ring gap is closed without out of plane bending nor twist. This state in which the ring has a round shape with its nominal radius, will be referred to as initial state with preload $F_{initial}$ for the following analyses.as stated before, once the ring gap is closed, small displacement assumption is valid and can be used to compute the curvature and torsion of the ring neutral axis.

$$\kappa_{yy0} = \frac{\cos(\alpha_p)}{R} \approx \frac{1}{R}$$

(2.85)

$$\kappa_{zz0} = \frac{\sin(\alpha_p)}{R} \approx \frac{\alpha_p}{R}$$

(2.86)

$$\tau_0 = 0$$

(2.87)

$$\alpha_0 = \alpha_p$$

(2.88)

$$\alpha_{n0} = 0$$

(2.89)

$$\kappa_{yy} \approx \left[\frac{1}{R} - \frac{y + y''}{R^2}\right] \cos\left(\alpha + \frac{z''}{R}\right) \approx \frac{1}{R} - \frac{y + y''}{R^2}$$

(2.90)

$$\kappa_{zz} \approx \left[\frac{1}{R} - \frac{y + y''}{R^2}\right] \sin\left(\alpha + \frac{z''}{R}\right) \approx \frac{\alpha + \frac{z''}{R}}{R}$$

(2.91)

$$\tau = \frac{z' + z^{(3)}}{R^2}$$

(2.92)

$$\alpha_n \approx -\frac{z''}{R}$$

(2.93)

When we calculate the curvature change along the $\boldsymbol{e}_{zz}$ direction, we will see that there will be a term $\alpha - \alpha_p$ which equals the ring twist α_r defined previously. Since the difference between α and α_p is constant and equal to the principal angle α_p, their derivatives with respect to θ are the same.

Combining the expression of the three components of the strain energy (2.49), (2.51) and (2.53) with the expression derived above for the different curvatures, torsion and the natural frame orientation angle we obtain the following expressions for the different components of the strain energy for the final state.

$$U_{zz}^{(e)} = \frac{1}{2}\int_0^{L_e} EI_{zz}\left(\kappa_{yy} - \kappa_{yy0}\right)^2 ds = \frac{L_e EI_{zz}}{2}\int_0^1 \left(\left(\frac{1}{R} - \frac{y + y''}{R^2}\right) - \frac{1}{R}\right)^2 d\eta$$
$$= \frac{L_e EI_{zz}}{2R^4}\int_0^1 \left(\sum_{k \in k_y} \left(N_{m(k)} + N''_{m(k)}\right) u_k\right)^2 d\eta$$

(2.94)

$$U_{yy}^{(e)} = \frac{1}{2}\int_0^{L_e} EI_{yy}(\kappa_{zz} - \kappa_{zz0})^2 ds = \frac{L_e EI_{yy}}{2}\int_0^1 \left(\frac{\alpha - \alpha_p}{R} + \frac{z''}{R^2}\right)^2 d\eta$$
$$= \frac{L_e EI_{yy}}{2R^4}\int_0^1 \left(\sum_{k \in k_z} N''_{m(k)} u_k + R \sum_{k \in k_\alpha} N_{\alpha m(k)} u_k\right)^2 d\eta$$

(2.95)

$$U_{\theta}^{(e)} = \frac{1}{2}\int_0^{L_e} GJ_t \left(\tau + \frac{d}{ds}(\alpha_n - \alpha)\right)^2 ds = \frac{L_e GJ_t}{2}\int_0^1 \left(\frac{z' - R\alpha'}{R^2}\right)^2 d\eta$$
$$= \frac{L_e GJ_t}{2R^4}\int_0^1 \left(\sum_{k \in k_z} N'_{m(k)} u_k - R \sum_{k \in k_\alpha} N'_{\alpha m(k)} u_k\right)^2 d\eta$$

(2.96)

$$U^{(e)} = U_{zz}^{(e)} + U_{yy}^{(e)} + U_{\theta}^{(e)}$$

(2.54)

Since the strain energy corresponding to the ring element is a bilinear form of the nodal displacements and their derivatives, we can write it in a matrix form (2.97).

$$U^{(e)} = \frac{1}{2}\{u\}^{(e)^T}[K]^{(e)}\{u\}^{(e)}$$

(2.97)

$[K]^{(e)}$ is called the stiffness matrix and its terms (2.98) are determined by comparing the matrix for of the strain energy (2.97) to its developed expression (2.94), (2.95), (2.96) and (2.54).

$$K_{ij}^{(e)} = \begin{cases} \dfrac{L_e E I_{zz}}{R^4}\displaystyle\int_0^1 \big(N_{m(i)} + N''_{m(i)}\big)\big(N_{m(j)} + N''_{m(j)}\big)d\eta & for\ \{i,j\} \in k_y \\ \dfrac{L_e}{R^2}\displaystyle\int_0^1 \big(EI_{yy}N_{\alpha m(i)}N_{\alpha m(j)} + GJ_t N'_{\alpha m(i)}N'_{\alpha m(j)}\big)d\eta & for\ \{i,j\} \in k_\alpha \\ \dfrac{L_e}{R^4}\displaystyle\int_0^1 \big(EI_{yy}N''_{m(i)}N''_{m(j)} + GJ_t N'_{m(i)}N'_{m(j)}\big)d\eta & for\ \{i,j\} \in k_z \\ \dfrac{L_e}{R^3}\displaystyle\int_0^1 \big(EI_{yy}N''_{m(i)}N_{\alpha m(j)} - GJ_t N'_{m(i)}N'_{m(j)}\big)d\eta & for\ (i,j) \in k_z \times k_\alpha\ or\ (i,j) \in k_\alpha \times k_z \\ 0 & otherwise \end{cases}$$

(2.98)

The following expression (2.99) gives the work of external forces as a function of the nodal displacements and their derivatives.

$$W^{(e)} = L_e \int_0^1 \left[f_r \sum_{k\in k_y} N_{m(k)}u_k + f_z \sum_{k\in k_z} N_{m(k)}u_k + m_t \sum_{k\in k_\alpha} N_{\alpha m(k)}u_k \right] d\eta = \{u\}^{(e)^T}\{F\}^{(e)}$$

(2.99)

The load vector terms (2.100) are equal to the integration of the product between the shape functions and the cross section resulting forces.

$$F_{ext,i}^{(e)} = \begin{Bmatrix} \int_0^{L_e} f_r N_{m(i)} ds & for\ i \in k_y \\ \int_0^{L_e} f_z N_{m(i)} ds & for\ i \in k_z \\ \int_0^{L_e} m_t N_{\alpha m(i)} ds & for\ i \in k_\alpha \end{Bmatrix}$$

(2.100)

The finite element equation of motion (2.101) is given by the Euler-Lagrange equation

$$[K]^{(e)}\{u\}^{(e)} = \{F_{ext}\}^{(e)} - \{F_{initial}\}^{(e)}$$

(2.101)

2.6. Assembly of finite element matrices

In order to obtain the finite element equations for the complete ring, we have to assemble the stiffness matrices and the load vectors corresponding to the different elements. The same process is used for conventional finite element models. Below, we give an example of two ring elements matrix assembly.

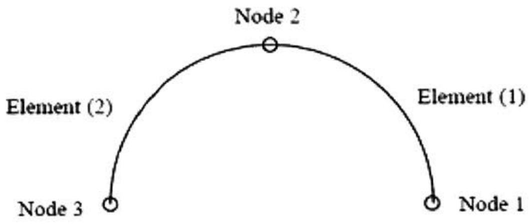

Figure 2.10 – Example of finite element matrix assembly for a two elements ring mesh

In this example, the ring mesh has two elements and three nodes. Element (1) and element (2) share node (2). The displacement vector corresponding to element (1) is given by (2.102) and the one corresponding to element (2) by (2.103).

$$\{u\}^{(1)} = \left\{u_1^{(1)}, u_2^{(1)}, \dots, u_{15}^{(1)}, u_{16}^{(1)}\right\}$$
$$= \{y_1, y_1', y_1'', z_1, z_1', z_1'', \alpha_1, \alpha_1', y_2, y_2', y_2'', z_2, z_2', z_2'', \alpha_2, \alpha_2'\}^T$$

(2.102)

$$\{u\}^{(2)} = \left\{u_1^{(2)}, u_2^{(2)}, \dots, u_{15}^{(2)}, u_{16}^{(2)}\right\}$$

$$= \{y_2, y_2', y_2'', z_2, z_2', z_2'', \alpha_2, \alpha_2', y_3, y_3', y_3'', z_3, z_3', z_3'', \alpha_3, \alpha_3'\}^T$$

(2.103)

The two elements stiffness matrices are given below (2.104). the exponent (k) refers to the element k and the index I refers to node i. as proven in the latter section, for each element we have a stiffness matrix that we can write into 4 sub-matrices form.

$$[K]^{(1)} = \begin{bmatrix} K_{11}\, K_{12} \\ K_{12}\, K_{22}^{(1)} \end{bmatrix}$$

(2.104)

$$[K]^{(2)} = \begin{bmatrix} K_{22}^{(2)}\, K_{23} \\ K_{23}\, K_{33} \end{bmatrix}$$

(2.105)

K_{11} is the sub-matrix containing the terms of the stiffness matrix related to the displacement of node 1. In the ring finite element model developed in this section and that will be used in the conformability analysis (Part 3 of this thesis) and the free shape, force distribution and ovality analysis (Part 5 of this thesis), each node has 8 degrees of freedom. Therefore the stiffness matrix is of dimension [16x16] and the submatrices like K_{11} is an [8x8] matrix. Hence, the half ring has 24 nodal displacements for its 3 nodes. The global stiffness matrix $[K]$ is obtained by assembling $[K]^{(1)}$ and $[K]^{(2)}$ (2.106).

$$[K] = \begin{bmatrix} K_{11} & K_{12} & 0 \\ K_{12} & K_{22}^{(1)} + K_{22}^{(2)} & K_{23} \\ 0 & K_{23} & K_{33} \end{bmatrix}$$

(2.106)

When we assemble the element matrices, we sum the contributions of both elements to the stiffness in node (2). The same process is used to assemble the global vector load. The finite element equations can be written using the global matrices (2.107) where $\{u\}$ (2.108) is the global displacement vector obtained as the assembly of the different nodal displacement vectors. In (2.108), n is the total number of nodes for the whole ring.

$$[K]\{u\} = \{F_{ext}\} - \{F_{intiial}\}$$

(2.107)

$$\{u\} = \left\{u_1^{(1)}, \dots, u_8^{(1)}, u_1^{(2)}, \dots, u_8^{(2)}, \dots, u_1^{(n-1)}, \dots, u_8^{(n-1)}, u_1^{(n)}, \dots, u_8^{(n)}\right\}^T$$

(2.108)

(2.107) is a non-linear system in $\{u\}$ to solve since $\{F_{ext}\}$ depends non-linearly on $\{u\}$. We use Newton-Raphson algorithm to solve that system.

2.7. Conclusion

The dual grid curved beam finite element model developed by Baelden [31] for the twin land oil control ring is mostly applicable to the top two rings except an additional step closing the ring. The finite element method is well adapted to the mechanics of the piston rings which are thin curved structures experiencing small deformation inside the engine. The key issue is the necessity to couple ring deformation to contact interaction with piston and liner although structural deformation and contact forces are on different length scales. The method of separation of structural mesh and contact grid using the element shape functions is efficient in solving this problem.

However, unlike TLOCR, the top two rings at their free state present free shapes which have several millimeters displacement with respect to the nominal bore radius. Therefore, the small displacement assumption required for Baelden's model to hold is no longer valid. To address this problem, an intermediate state is considered in which the single piece ring is closed at its nominal radius with a preload. Starting from this intermediate state as the initial one, we can conduct the single piece static analysis based on the finite element model developed in sections 2.5 and 2.6. indeed, the small displacement assumption is valid in this case since each point's displacement, when the ring deforms from the centered position in the piston groove and contacting a perfectly round cylinder with a nominal radius, is small compared to the bore radius.

The curved beam finite element method developed in sections 2.5 and 2.6 and summarized in (2.107) provide a numerical framework for the study of the ring conformability studied in part 3. This framework will be extended for the study of the ring static twist in part 4 by considering more degrees of freedom per node since we add the tapping force related unknowns. In order to maintain a close system, we will also add more equations based on the ID or OD clearances constraint. Besides, the framework developed in this section will also be used in part 5 to derive the force distribution in radial final shape and the ovality, both from ring's free shape, by considering the appropriate external forces in each case.

3. Conformability analysis

In this chapter we apply the curved beam finite element model presented in the previous section to study the ring conformability with the groove and the liner. We also used the method introduced to handle large displacement when closing the ring starting from its free shape to its nominal radius. As proved in L. Liu works [26], [27] and [30] and in Y. Liu thesis [33], many useful analyses can be carried out without including ring's dynamics. This study includes contact force distribution relations, ring interaction with a distorted bore and ring interaction with gas pressures. We also include in our work the effect of oil lubrication on the groove flanks and liner, the non-zero gap effect and the modeling of the thermal moment introduced by the temperature gradient between the ring's ID and OD.

In this chapter, a comprehensive analytical tool based on the curved beam finite element model is developed. It evaluates the ring-liner and ring-groove conformability under different boundary conditions and studies the relation between local contact behavior and global structural deformation and stress distributions. The advantage of the model is that it enables the study of the force generation mechanisms along the ring circumference depending on the local lubrication conditions, the local thermal effects, the bore distortion and the ring gap effect with the own length scale related to these conditions and at the same time gives accurate results for the ring structural response with enough flexibility and low computation cost compared to the dynamic study.

The derivation of the ring-liner and ring-groove contact forces for the different boundary conditions to be used in the finite element equations was developed in Y. Liu [33] work. We present here the calculation details for the sake of clarity and to have a more complete work and comprehensible model. We also explain the methods we opted to in order to consider the thermal moment effect and the existence of ring gap.

In engine cycles, the piston rings have different forces applied. Besides inertia, when assembled into piston, the top two rings are closed from their free shape and as described in the previous section, the change of curvature and torsion of their neutral axes create internal stress which is considered in our model as initial force. Pressured gas flows around the ring pack system and contributes to pressure force in both radial and axial directions. The liner provides dry or hydrodynamic contact force in the radial direction and friction force in the axial one. The ring-groove interaction includes dry contact force, oil pressure force due to squeezing and also gas pressure force if gas flows through the ring-groove clearance. Figure 3.1 represents all the forces acting on the ring.

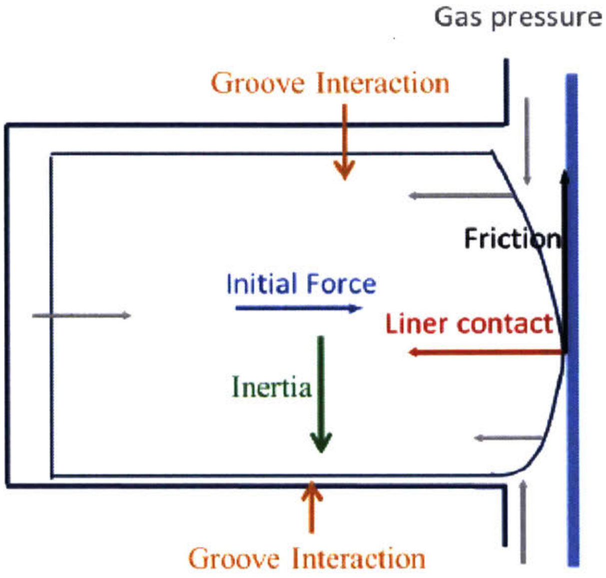

Figure 3.1 – Forces acting on ring

The resultant forces include three components: the radial force, the axial one and the twisting moment. These components are used to compute the external load vector in the governing equations derived in the previous section for the finite element curved beam model. Figure 3.2 shows the coordinate system that we uses and which determines the signs of the different components of the resultant forces.

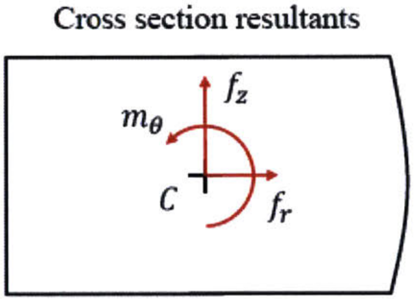

Figure 3.2 – Resultant forces and coordinate system

3.1. Ring-liner sub-model

Ring-liner interaction includes dry-contact force, hydrodynamic force from the oil film between the ring and the liner and gas pressure force. The ring-liner interaction sub-model is based on the curved beam finite element model and thus is able to include global as well as local processes. Piston rings conform to the distorted bore and groove due to tangential load and gas pressure which results in the contact pressure distribution. Thus, we obtain a local force generation depending on oil supply. In reality, circumferential gas flow causes local oil accumulation on piston lands which creates local oil supply to the top two rings via bridging [42], [44], [45]. Besides, in the direct injection engine, fuel may be sprayed sporadically to the liner, which affects the ring-liner interaction by changing the local oil film viscosity.

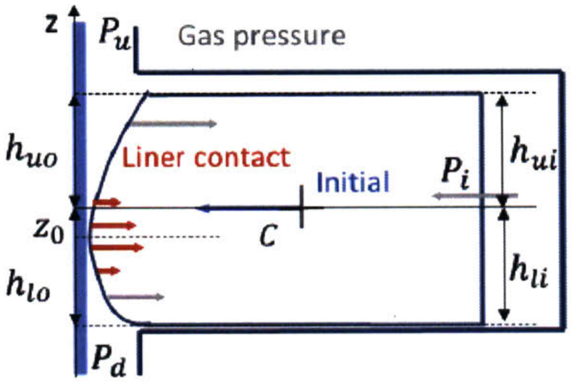

Figure 3.3 – Ring-liner interaction

Figure 3.3 shows the radial forces involved in the ring-liner interaction. They include the gas pressures which changes in time and in the circumferential direction. Gas inside the ring groove pushes the ring toward the liner and gas from the piston upper and lower lands pushes it inwards. The force and moments per unit length created by the gas pressure in the radial direction and to be used in the finite element curved beam model are given below. For the rest of this thesis, the pressure acting in the regions above the minimum point (defined as the point on the ring running surface that is closest to the liner) is assumed to be the piston upper land pressure P_u and the pressure below the minimum point is assumed to the piston lower land pressure P_d, as shown in Figure 3.3. The location of the minimum point shifts with ring twist and is called dynamic minimum point, z_0. The minimum point when ring is in free state is called original minimum point, rbn.

$$f_{r,gas} = P_i(h_{ui} + h_{li}) - P_u(h_{uo} - z_0) - P_d(h_{lo} + z_0)$$

(3.1)

$$m_{r,gas} = -\frac{1}{2}P_i h_{ui}^2 + \frac{1}{2}P_i h_{li}^2 + \frac{1}{2}P_u(h_{uo}^2 - z_0^2) - \frac{1}{2}P_d(h_{lo}^2 - z_0^2)$$

(3.2)

Besides we also have to consider the initial radial force which was derived in the previous section. For the top two rings, this force comes from the rings' strain energy created after closing them from their free shape. Once they are closed and assembled inside the cylinder, the rings expands and are pushed toward the liner. Equation (2.82) provides the expression of that force as reminded below.

$$F_{initial,k_y}^{(e)} = \frac{\partial U^{(e)}}{\partial u_{k_y}} \bigg|_{\substack{y=0,y'=0,y''=0 \\ z=0,z'=0,z''=0 \\ \alpha=\alpha_p,\alpha'=0}}$$

$$= -L_e E I_{zz} \int_0^1 \left(\frac{1}{R} - \kappa_{fs}\right) \frac{\cos^2(\alpha_p)}{R^2} \left(N_{m(k_y)} + N''_{m(k_y)}\right) d\eta$$

$$-L_e E I_{yy} \int_0^1 \left(\frac{1}{R} - \kappa_{fs}\right) \frac{\sin^2(\alpha_p)}{R^2} \left(N_{m(k_y)} + N''_{m(k_y)}\right) d\eta$$

(2.82)

Finally, we have to consider the contact force between the liner and the ring. This force includes two different contact models. One of them is the dry contact force which is computed using the Greenwoods-Tripp model and the other one is hydrodynamic pressure which can be calculated using the correlations determined by Chen, Y. Liu and Li etc [35] [36]. For the hydrodynamic lubrication model we also differentiate between the fully flooded the partially flooded conditions.

3.1.1. Ring-liner dry-contact

The radial reference position is such the ring is in contact with the non-distorted cylinder. For this configuration, the distance between the centroid of the ring cross section and the nominal bore is y_c. The ring's profile is considered as parabolic and the running surface of the ring is estimated as barrel shape with the following expression:

$$y_{barrel} = a_0 + a_1(z - rbn) + a_2)(z - rbn)^2$$

(3.3)

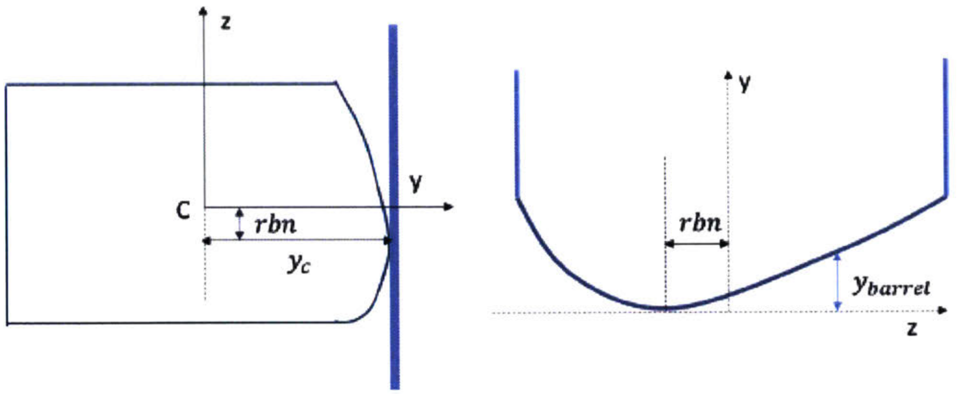

Figure 3.4 – Ring profile

The ring-liner minimum point is defined as the point on the ring running surface which is the closest to the liner. When the ring is in free state with no twist, the axial location of the minimum point is rbn. The barrel drop of the ring profile has a magnitude of the order of $100\ \mu m$. The radial position of ring's running surface point using the reference introduced above is $y = y_c - y_{barrel}$.

Ring twist will move its running surface to a new position. Since the ring twist around is centroid is characterize by α_r, the new position after the rotation is determined by the following equation:

$$\begin{bmatrix} y' \\ z' \end{bmatrix} = \begin{bmatrix} \cos(\alpha_r) & -\sin(\alpha_r) \\ \sin(\alpha_r) & \cos(\alpha_r) \end{bmatrix} \begin{bmatrix} y \\ z \end{bmatrix}$$

(3.4)

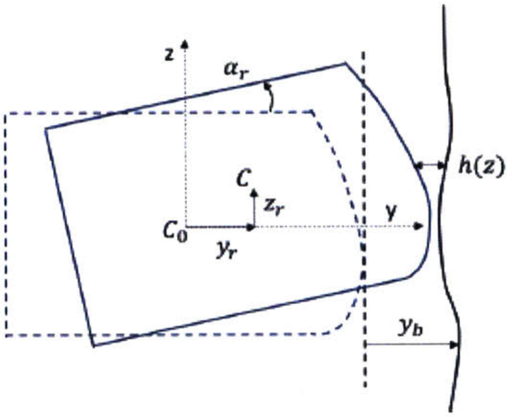

Figure 3.5 – Ring-liner relative position

As shown in Figure 3.5, we note the ring's radial displacement relative to its reference position by y_r and the radial displacement of the cylinder from its nominal position due to bore distortion by y_b. The local clearance between the ring and liner is therefore given by:

$$h(z) = y_b - y_r + y_c - y' = y_b - y_r + y_{barrel} + \alpha_r z$$

(3.5)

The asperity contact used in this thesis, for the ring-liner contact as well as the ring-groove one, is derived from Greenwood and Tripp work on rough surfaces contact [37]. More precisely we will use the simplified formulation derived by Hu [38].

$$P_c = \begin{cases} 0 & \frac{h}{\sigma} \geq \Omega \\ P_k \left(\Omega - \frac{h}{\sigma}\right)^z & \frac{h}{\sigma} \leq \Omega \end{cases}$$

(3.6)

P_c is the asperity contact pressure, h is the local ring-liner clearance (ring-groove clearance when used in section 3.1.2) and σ the standard deviation of the liner roughness (groove flank roughness when used in section 3.1.2). Ω is the threshold that determines the clearance under which the asperity contact is generated. A typical value for this threshold is 4. The correlation constant P_k depends on the properties of the ring and the liner material (groove flank materials when used in section 3.1.2).

$$P_k = \frac{2KA}{\frac{1 - \nu_l^2}{E_l} + \frac{1 - \nu_r^2}{E_r}}$$

(3.7)

E_l, E_r, ν_l and ν_r are the Young's modulus and Poisson ratio of the liner (of the groove flanks when used in section 3.1.2) and the ring respectively. K, A and z are universal constants determined by Hu [38].

$$K = 1.198 \times 10^{-4}, A = 4.4068 \times 10^{-5} \; and \; z = 6.804$$

(3.8)

Finally, we obtain the force and moment per unit length corresponding to the ring-liner dry contact by integrating the local pressure and the corresponding local moment along the ring-liner contact region CR that satisfies the dry contact force existence and by substituting the ring-liner clearance in (3.6).

The axial component of the force contact is obtained using a proportional relation with the radial one. A typical value for the friction coefficient f_c is around 0.1.

$$f_{cL} = \int_{CR} -P_k\left(\Omega - \frac{y_b - y_r + y_{barrel} + \alpha_r z'}{\sigma_p}\right)^z dz'$$

(3.9)

$$f_{z,cL} = sign(V) f_c f_{cL}$$

(3.10)

$$m_{cL} = sign(V) f_c f_{cL} y_c + \int_{CR} P_k\left(\Omega - \frac{y_b - y_r + y_{barrel} + \alpha_r z'}{\sigma_p}\right)^z [\alpha_r(y_c - y_{barrel}) + z']dz'$$

(3.11)

V represents the ring sliding speed. $sign(V) = 1$ is V is positive and -1 if it is negative. The negative sign in f_{cL} is conform to the coordinate system adopted since the liner contact force acts on the ring inwards.

3.1.2. Hydrodynamic lubrication models

The piston-ring sliding generates hydrodynamic pressure within the oil film covering the liner. This pressure can be estimated based on Reynolds equation. Classic lubrication models estimate the hydrodynamic pressure without considering the surface roughness, although this assumption may give biased estimations. The top two rings have profiles which could help generate hydrodynamic pressure. However, their oil supply is mostly determined by the oil control ring. When the supplied oil has a thickness to the level of the surface roughness, we expect the oil film thickness between the top two rings and the liner to also be at the same level. Therefore, our model should consider the roughness geometry effect since it is a significant factor in determining the hydrodynamic pressure generated.

Different mechanisms determine the oil supply to the top two rings. The oil film thickness on the liner in most of the areas traveled by the top two rings is controlled by the oil control ring. In this case, the oil supply is partially flooded and the deterministic correlations of the top two rings can be used to determine the hydrodynamic pressure and the shear stress (Section 3.1.2.2). However, bridging can increase the amount of oil by bringing it from the piston lands to the liner. Based on the timing and the location of the bridging, this accumulated amount of oil may counter the top two rings and interact with them. This situation corresponds to the fully flooded case and the correlations presented in Section 3.1.2.1 can be used to evaluate the hydrodynamic pressure and shear stress between the top two rings and the liner.

3.1.2.1. Partially flooded case

For the partially flooded boundary conditions, we use the deterministic model that gives the hydrodynamic pressure between the top two rings and the liner and developed by Chen [35]. Surface roughness as well as ring profile are taken into consideration in this model. It uses the oil film thickness fed into the ring. Chen has also developed a correlation relating the hydrodynamic pressure, the minimum clearance between the corresponding ring and the liner and the OCR ring-liner clearance. The shear stress related to the hydrodynamic pressure is also given below.

$$P_{hydro} = \left(\frac{h_{OCR}}{h_{prof}}\right)^{K_p} \frac{\mu V}{(\mu V)_0} \left(a_p P_{0,OCR}\right) \left(\frac{h_{prof}}{\sigma_p}\right)^{-K_{OCR}}$$

(3.12)

$$\tau_{hydro} = \frac{F_0(\mu V)}{h_{prof}} \left(\frac{h_{OCR}}{h_{prof}}\right)^{K_f}$$

(3.13)

$P_{0,OCR}$ and K_{OCR} are coefficients from the OCR deterministic correlation [39], μ and V represent oil dynamic viscosity and ring sliding speed respectively. $(\mu V)_0$ corresponds to the reference value of μV used in the simulation. h_{OCR} is the OCR-liner clearance and h_{prof} is the minimum clearance between the top two rings and liner. The filling effect is taken into account via the term $\left(\frac{h_{OCR}}{h_{prof}}\right)^{K_p}$. Since the rate of filling effect varies depending on the oil supply, K_p and K_f is not a constant and we correlate it using first order approximation as a linear function of $\frac{h_{OCR}}{\sigma_p}$. The ring profile effect is modeled by the term a_p. This term is constant for a given liner finish and a ring profile. F_0 is a friction coefficient.

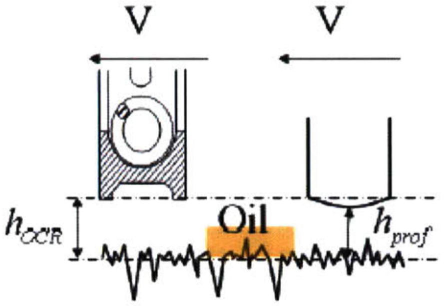

Figure 3.6 – Ring clearances for partially flooded case

In this case, the radial and axial forces as well as the moment per unit length to be used in the finite element curved beam model for the external force are given by the following equations, where r_w is the ring width in the axial direction.

$$f_{r,hydro} = -P_{hydro} r_w$$

(3.14)

$$f_{z,hydro} = -\tau_{hydro} r_w$$

(3.15)

$$m_{hydro} = -f_{r,hydro} z_0 + f_{z,hydro} y_c = P_{hydro} r_w z_0 - \tau_{hydro} r_w y_c$$

(3.16)

The negative signs are conform to the coordinate system adopted and z_0 here refers to the minimum ring-liner clearance point axial location considering ring's profile and its twist (As represented in Figure 3.5).

3.1.2.2. Fully flooded case

Oil supply to the top two rings does not always come solely from the oil film left by the oil control ring. In some cases, around the top or bottom dead centers of the liner, bridging may occur and this brings additional amount of oil from the piston to the liner. This extra oil bypasses the oil control ring and encounters directly the top two rings. Therefore, the boundary condition of the top two rings changes to fully flooded. Bridging brings an additional amount of oil with a thickness of the order of $10\ \mu m$ which exceeds the correlating range of the partially flooded condition. Besides, the large oil film thickness implies that the surface roughness does not have significant effect anymore. Therefore, we can determine the hydrodynamic force using Reynolds equation for a given ring profile and a smooth liner.

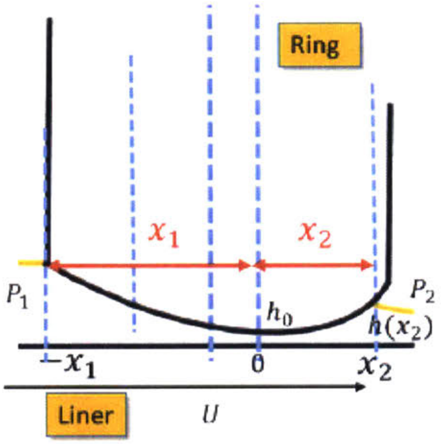

$$h = h_0 + ax^2$$

Figure 3.7 – Ring and liner geometry

Oil supply is sufficient in this case at the leading edge x_1 which is an input to our model. The trailing edge which corresponds to the end of the wetting area is referenced as x_2. At that point we apply the boundary condition $\frac{\partial P}{\partial x}|_{x_2} = 0$. x_2 depends on the leading edge length x_1 and the ring-liner minimum clearance h_0. The ambient pressure is the atmospheric one. The boundary gas pressure effect is not included here since we already considered it in (3.1) and (3.2). We also assume that oil squeezing effect is negligible and thus we can used the steady state Reynolds equation which can be written as:

$$\frac{dP}{dx} = \frac{6\mu U}{h^3}\left(h - h(x_2)\right)$$

(3.17)

where we used the boundary condition $\frac{\partial P}{\partial x}|_{x_2} = 0$.

Applying ambient pressure boundary condition, we obtain:

$$\int_{-x_1}^{x_2} \frac{dP}{dx}\,dx = \int_{-x_1}^{x_2} \frac{6\mu U}{h^3}\left(h - h(x_2)\right) dx = 0$$

(3.18)

This gives us the following relation relating $x_1$and x_2:

$$h(x_2) = \frac{\int_{-x_1}^{x_2} \frac{dx}{h^2}}{\int_{-x_1}^{x_2} \frac{dx}{h^3}}$$

(3.19)

The radial hydrodynamic force per unit length in this case is equal to $f_{r,hydro} = \int_{-x_1}^{x_2} P\, dx$. Doing an integration by part we obtain:

$$f_{r,hydro} = \int_{-x_1}^{x_2} x \frac{dP}{dx} dx = \int_{-x_1}^{x_2} x \frac{6\mu U}{h^3} \left(h - h(x_2)\right) dx$$

(3.20)

Solving (3.19) and (3.20) numerically with $h = h_0 + ax^2$, Li has developed a correlation that gives an explicit expression of $f_{r,hydro}$ as a function the ring-liner minimum clearance h_0 and the leading edge length x_1.

$$f_{r,hydro} = \frac{12\mu V}{a h_0} c \left(\frac{1 + \tanh\left(\frac{\log_{10}(a x_1^2 / h_0\,) + d}{e} \right)}{2} \right)^b$$

(3.21)

a is the ring profile shape factor that appears in the expression $h = h_0 + ax^2$ for the ring profile and b, c, d and e are universal constants.

Considering oil as a Newtonian fluid, we determine the corresponding shear stress and the moment per unit length to be included in our finite element curved beam model.

$$f_{z,hydro} = \int_{-x_1}^{x_2} \frac{\mu V}{h} dx = \frac{\mu V}{\sqrt{a h_0}} \left[\arctan\left(\sqrt{\frac{a}{h_0}} x_2 \right) + \arctan\left(\sqrt{\frac{a}{h_0}}\, x_1 \right) \right]$$

(3.22)

$$m_{hydro} = -f_{r,hydro} z_0 + f_{z,hydro} y_c$$

(3.23)

3.2. Ring-groove sub-model

Ring-groove interaction includes the asperity contact force, oil pressure force due to squeezing, hydrostatic force and gas pressure force. We assume that there is a uniform oil layer on both groove flanks. This assumption let us obtain a qualitatively accurate estimation of the acting force from oil squeezing effect.

3.2.1. Ring-groove geometry

Due to piston tilting, the piston groove moves axially and is also tilted as shown in Figure 3.8. Since the piston tilt angle β_p is small (~$0.1°$), we can use small displacement assumption and approximate the tilted angle of the groove and its axial displacement by first order interpolations which results in linear form of β_p.

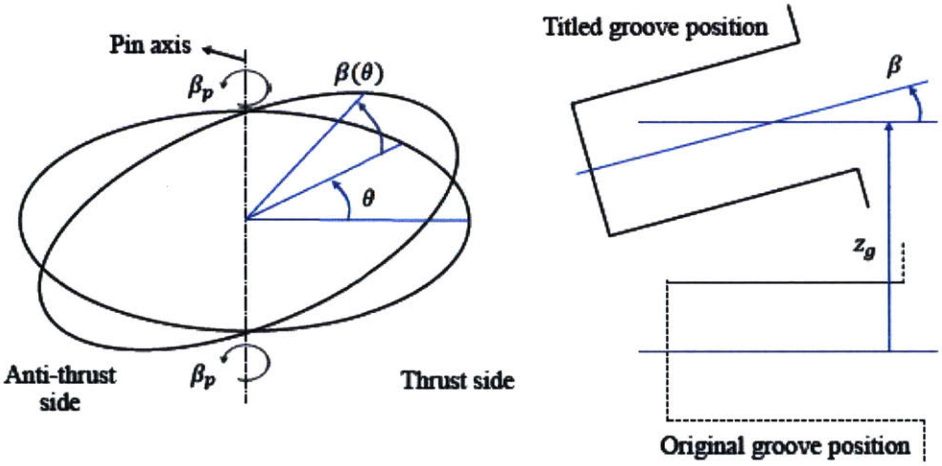

Figure 3.8 – Groove displacement within a tilted piston

The rotation of the groove located at the polar angle θ can be approximated by the following expression, where $\theta = 0$ is set at the thrust side.

$$\beta = \cos(\theta)\beta_p$$

(3.24)

Always using the small displacement assumption, the groove axial displacement can be calculated as follows:

$$zg = (Rcos(\theta) - off)\beta_p$$

(3.25)

off represents the piston offset (it is positive when the pin axis is moved towards the thrust side) and R is the ring radius. Our model also considers the thermal deformation of the piston groove.

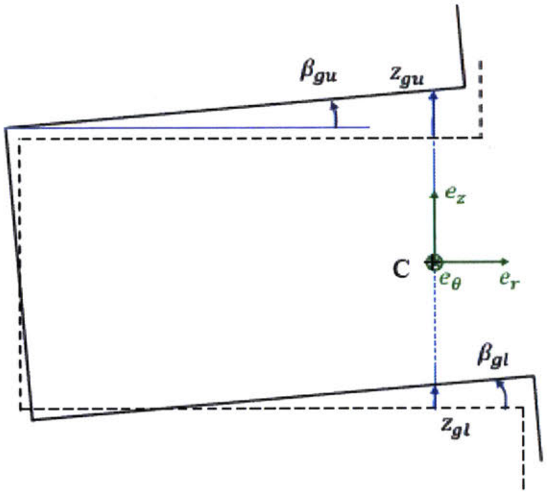

Figure 3.9 – Piston groove thermal deformation

The axial displacements of the upper and lower groove flanks due to thermal distortion are z_{gu} and z_{gl} respectively. They are measured at the radial location of the ring cross section centroid C. β_{gu} and β_{gl} are the groove tilt angles due to thermal distortion.

The clearances between the ring and the groove flanks at the radial location y is calculated by considering ring displacement, piston tilt and piston thermal distortion. The reference point is the radial location of the cross section centroid C. h_g is the axial clearance between the ring and the groove flank. The ring-groove upper flank clearance is calculated as follows:

$$h_{gu}(y) = \frac{h_g}{2} + z_g + z_{gu} - z_r + y(\beta + \beta_{gu} - \alpha_r)$$

(3.26)

The ring-groove lower flank clearance is determined by the following expression:

$$h_{gl}(y) = \frac{h_g}{2} - z_g - z_{gl} + z_r + y(\alpha_r - \beta - \beta_{gl})$$

(3.27)

3.2.2. Ring-groove dry contact

As for the ring-liner interaction, the ring-groove dry contact is modeled using the simplified formulation of the Greenwood and Tripp pressure contact formula (3.6) by integrating it over the contact area as shown in Figure 3.10.

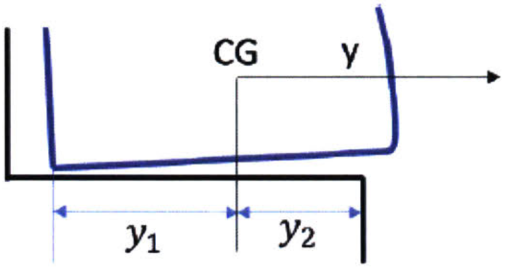

Figure 3.10 – Ring-groove (lower flank) contact area

By noting the ring-groove upper flank clearance at the centroid h_{gu0}, and using the equation (3.26), we derive the following expression for h_{gu0} and we express $h_{gu}(y)$ at any radial location y using h_{gu0}.

$$h_{gu0} - \frac{h_g}{2} + z_{gu} + z_g - z_r$$

(3.28)

$$h_{gu}(y) = h_{gu0} + y(\beta + \beta_{gu} - \alpha_r)$$

(3.29)

Using this formula for the local clearance in equation (3.6) and integrating it over the ring-groove upper flank contact area, we obtain the following expressions for the axial contact force and moment per unit length associated with this contact interaction. In that expression and for the correlation constant P_k, we consider the surface roughness standard deviation, the Yong's modulus and Poisson ration corresponding to the groove flanks. Considering the ring upper flank angle α_{gu} as shown in Figure 3.11, we also obtain the radial component of the ring-groove dry force where we assumed small magnitude for α_{gu}.

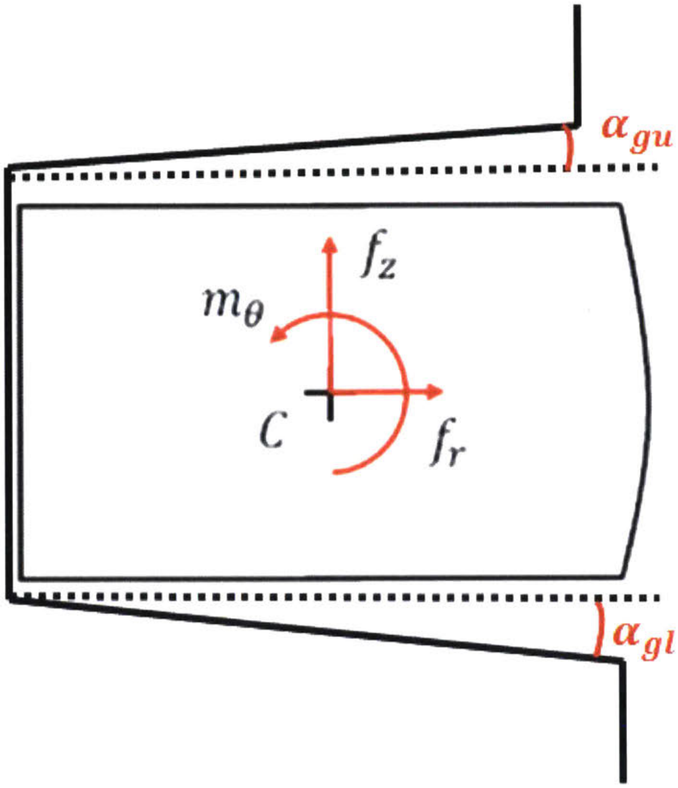

Figure 3.11 – Groove upper and lower flank angles

$$f_{c,gu} = \int_{y_1}^{y_2} -P_k \left[\Omega - \frac{h_{gu0} + y\left(\beta + \beta_{gu} - \alpha_r\right)}{\sigma_g}\right]^z dy$$

$$= -\frac{P_k \sigma_g}{(z+1)\left(\alpha_r - \beta - \beta_{gu}\right)}\left[\left(\Omega - \frac{h_2}{\sigma_g}\right)^{z+1} - \left(\Omega - \frac{h_1}{\sigma_g}\right)^{z+1}\right]$$

(3.30)

$$f_{r,gu} = -\alpha_{gu} f_{c,gu}$$

(3.31)

$$m_{c,gu} = \alpha_{gu} h_{ui} f_{c,gu} + \int_{y_1}^{y_2} -P_k \left[\Omega - \frac{h_{gu0} + y\left(\beta + \beta_{gu} - \alpha_r\right)}{\sigma_g}\right]^z y\, dy$$

$$= \alpha_{gu} h_{ui} f_{c,gu} + \frac{P_k \sigma_g}{(z+1)(z+2)\left(\alpha_r - \beta - \beta_{gu}\right)^2} \left\{ \left(\Omega - \frac{h_1}{\sigma_g}\right)^{z+1} \left[\left(h_{gu0} - h_1\right)(z+1) + h_{gu0} - \Omega\sigma_g\right] - \left(\Omega - \frac{h_2}{\sigma_g}\right)^{z+1} \left[\left(h_{gu0} - h_2\right)(z+1) + h_{gu0} - \Omega\sigma_g\right] \right\}$$

(3.32)

y_1 is the left end of the contact area whose value may be negative if it is at the left side of the centroid C and y_2 is the right end of the contact area and its value may also be negative if it is at the left side of the centroid C. h_1 and h_2 are the local clearances at those two points. The negative sign inside the integrals in (3.30) and (3.32) implies that the direction of the force is downward. Besides, the negative sign in the radial force, so that the result is positive since $f_{c,gu}$ is negative, is coherent with the coordinate system chosen since that force is acting outwards and thus must be positive.

Similarly, we obtain the following expressions for the forces and the moment per unit length acting on the ring from the groove lower flank.

$$h_{gl0} \frac{h_g}{2} - z_{gl} - z_g + z_r$$

(3.33)

$$h_{gl}(y) = h_{gl0} + y(\alpha_r - \beta - \beta_{gl})$$

(3.34)

$$f_{c,gl} = \int_{y_1}^{y_2} P_k \left[\Omega - \frac{h_{gl0} + y\left(\alpha_r - \beta - \beta_{gu}\right)}{\sigma_g}\right]^z dy$$

$$= -\frac{P_k \sigma_g}{(z+1)\left(\alpha_r - \beta - \beta_{gu}\right)} \left[\left(\Omega - \frac{h_2}{\sigma_g}\right)^{z+1} - \left(\Omega - \frac{h_1}{\sigma_g}\right)^{z+1}\right]$$

(3.35)

$$f_{r,gu} = \alpha_{gl} f_{c,gl}$$

(3.36)

$$m_{c,gu} = \alpha_{gl} h_{li} f_{c,gl} + \int_{y_1}^{y_2} P_k \left[\Omega - \frac{h_{gl0} + y\left(\alpha_r - \beta - \beta_{gu}\right)}{\sigma_g}\right]^z y\, dy$$

$$
= \alpha_{gl} h_{li} f_{c,gl} + \frac{P_k \sigma_g}{(z+1)(z+2)\left(\alpha_r - \beta - \beta_{gu}\right)^2} \left\{ \left(\Omega - \frac{h_2}{\sigma_g}\right)^{z+1} \left[\left(h_{gl0} - h_2\right)(z+1) + h_{gl0} - \Omega\sigma_g\right] \right.
$$

$$
\left. - \left(\Omega - \frac{h_1}{\sigma_g}\right)^{z+1} \left[\left(h_{gl0} - h_1\right)(z+1) + h_{gl0} - \Omega\sigma_g\right] \right\}
$$

(3.37)

3.2.3. Oil squeezing and ring-groove hydrostatic force

No experimental data about the oil film thickness on the groove flanks is available. However, as suggested by Tian [40], provided it is assumed that the oil film thickness is on the order of a few microns. The oil flow between the ring and the groove flanks has Reynolds number on the order of one and the angle between the ring and the groove is on the order of $0.01\ rad$. Therefore we can apply the Reynolds equation. Tian also pointed out that the ring's moving away from the groove starts from a certain point and then gradually extends to the entire part of the ring. Thus, the possibility of suction or negative pressure is negligible.

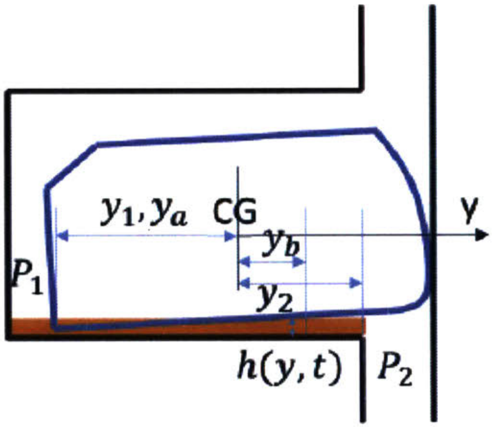

Figure 3.12 – Ring groove lubrication

As shown in Figure 3.12, considering the lower flank first, y_1 and y_2 are the two end points of the ring-lower groove interacting region and y_a and y_b are the two end points where ring touches the oil film on the groove lower flank. The squeezing pressure in the oil film can be determined using Reynolds equation.

$$
\frac{1}{12\mu_{oil}} \frac{\partial}{\partial y}\left(h^3 \frac{\partial P_{oil}}{\partial y}\right) = \frac{\partial h}{\partial t}
$$

(3.38)

P_{oil} is the pressure in the oil film due to squeezing and μ_{oil} is the oil dynamic viscosity. In the general case, since the possibility of suction or negative pressure is negligible, the term $\frac{\partial h}{\partial t}$ is set equal to zero when its value is greater than zero. In our study since we consider the static case this derivative is taken equal to zero. We keep this term in the following equations just for the sake of generalities toward dynamic studies. Integrating (3.38) gives the following equation.

$$\frac{\partial P_{oil}}{\partial t} = \frac{1}{h^3}(12\mu_{oil}J(y) + c_1)$$

(3.39)

With

$$J(y) = \int_a^y \frac{\partial h}{\partial t} dy'$$

(3.40)

$$c_1 = \frac{P_d - P_i - 12\mu_{oil}\int_a^b \frac{J(y)}{h^3} dy}{\int_a^b \frac{dy}{h^3}}$$

(3.41)

Integrating (3.39) by parts gives us the squeezing force and the corresponding moment per unit length for the ring groove

$$f_{oil,gl} = \int_a^b P_{oil} dy = P_d(y_b - y_a) - \int_a^b (y - y_a)\frac{\partial P_{oil}}{\partial y} dy$$

$$= P_d(y_b - y_a) - 12\mu_{oil}\int_a^y \frac{(y - y_a)J(y)}{h^3} dy - c_1 \int_a^b \frac{y - y_a}{h^3} dy$$

(3.42)

$$m_{oil,gl} = \int_a^b P_{oil} y dy = \frac{P_d(y_b^2 - y_a^2)}{2} - \frac{1}{2}\int_a^b (y - y_a)^2 \frac{\partial P_{oil}}{\partial y} dy$$

$$= \frac{P_d(y_b^2 - y_a^2)}{2} - 6\mu_{oil}\int_a^y \frac{(y^2 - y_a^2)J(y)}{h^3} dy - \frac{c_1}{2}\int_a^b \frac{y^2 - y_a^2}{h^3} dy$$

(3.43)

The ring-groove interacting area is not always the same as the ring-oil contact area. Thus, gas will fill in the space between the ring and the oil film generating hydrostatic pressure force. The corresponding force and moment per unit length are given below:

$$f_{hydro-static,gl} = (y_a - y_1)P_i + (y_2 - y_b)P_d$$

(3.44)

$$m_{hydro-static,gl} = \frac{1}{2}\left[(y_a^2 - y_1^2)P_i + \left(y_2^2 - y_b^2\right)P_d\right]$$

(3.45)

Considering groove lower flank angles, we obtain the following components corresponding to the axial force and the additional moment term per unit length.

$$f_{zoil,gl} = \left(f_{oil,gl} + f_{hydro-static,gl}\right)\alpha_{gl}$$

(3.46)

$$m_{zoil,gl} = \left(f_{oil,gl} + f_{hydro-static,gl}\right)h_{li}\alpha_{gl}$$

(3.47)

Similarly, we obtain the following expressions for the forces and moment per unit length acting on the ring from the groove upper flank. y_1 and y_2 are the two end points of the ring-upper groove interacting region and y_a and y_b are the two end points where ring touches the oil film on the groove upper flank. The expression of $J(y)$ is still the same.

$$c_1 = \frac{P_u - P_i - 12\mu_{oil}\int_a^b \frac{J(y)}{h^3}dy}{\int_a^b \frac{dy}{h^3}}$$

(3.48)

$$f_{oil,gu} = -\int_a^b P_{oil}dy = -P_u(y_b - y_a) + \int_a^b (y - y_a)\frac{\partial P_{oil}}{\partial y}dy$$

$$= -P_u(y_b - y_a) + 12\mu_{oil}\int_a^y \frac{(y - y_a)J(y)}{h^3}dy + c_1\int_a^b \frac{y - y_a}{h^3}dy$$

(3.49)

$$m_{oil,gu} = -\int_a^b P_{oil} y dy = -\frac{P_u\left(y_b^2 - y_a^2\right)}{2} + \frac{1}{2}\int_a^b (y - y_a)^2 \frac{\partial P_{oil}}{\partial y} dy$$

$$= -\frac{P_u\left(y_b^2 - y_a^2\right)}{2} + 6\mu_{oil}\int_a^y \frac{(y^2 - y_a^2)J(y)}{h^3} dy + \frac{c_1}{2}\int_a^b \frac{y^2 - y_a^2}{h^3} dy$$

(3.50)

$$f_{hydro-static,gu} = -(y_a - y_1)P_i - (y_2 - y_b)P_u$$

(3.51)

$$m_{hydro-static,gu} = -\frac{1}{2}\left[(y_a^2 - y_1^2)P_i + \left(y_2^2 - y_b^2\right)P_u\right]$$

(3.52)

$$f_{zoil,gu} = -\left(f_{oil,gu} + f_{hydro-static,gu}\right)\alpha_{gu}$$

(3.53)

$$m_{zoil,gu} = \left(f_{oil,gu} + f_{hydro-static,gu}\right)h_{ui}\alpha_{gu}$$

(3.54)

3.2.4. Ring-groove gas pressure force

When the ring-groove clearance is larger than the oil film thickness on the groove, gas will flow driven by pressure difference. As studied by Tian [40], this gas flow through the ring-groove clearance can be treated as laminar flow. In reality. Convection and unsteady effects can be significant when the ring is in transition, especially when it flutters. Since dynamic study and detailed characterization of the gas flow through the ring-groove clearance is beyond the scope of this work, we limit the description of the gas flow to be qualitatively accurate and we rely on an analytical solution to a from a fast engineering model.

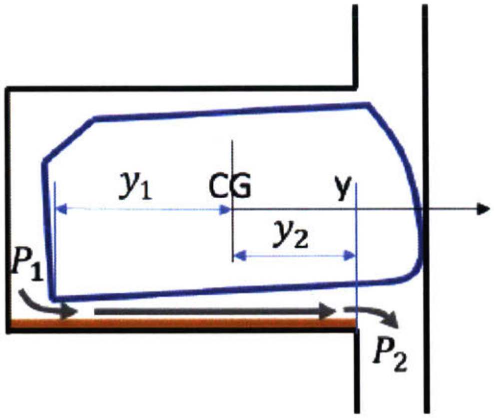

Figure 3.13 – Ring groove gas flow

The groove-ring channel is represented in Figure 3.13. We approximate the gas flow through the ring-groove clearance as a fully-developed, quasi-steady and locally-parallel flow. Due to the very small viscosity of gas, we neglect the pumping and squeezing effect due to the ring-groove relative motion.

For Poiseuille flow, the local velocity is given by:

$$u(y,z) = \frac{1}{2\mu}\frac{dP_{gas}}{dy} z\left(z - h_c(y)\right)$$

(3.55)

$$h_c(y) = h(y) - h_{oil}$$

(3.56)

The gas pressure satisfies the following equation using the Reynolds one and the quasi-steady assumption:

$$\frac{d}{dy}\left(h_c^3 \frac{dP_{gas}}{dy}\right) = 0$$

(3.57)

Integrating this equation with the boundary conditions $P(y_1) = P_1$ and $P(y_2) = P_2$ gives the following relation for the lower groove flank:

$$\frac{dP_{gas}}{dy} = \frac{P_d - P_i}{h_c^3 \int_{y_1}^{y_2} \frac{dy}{h_c^3}}$$

(3.58)

The axial force and moment per unit length at each cross section can be expressed as follows:

$$f_{gaz,gl} = \int_{y_1}^{y_2} P_{gas} dy = P_d(y_b - y_a) - \int_{y_1}^{y_2} (y - y_a) \frac{dP_{gas}}{dy} dy$$

(3.59)

$$m_{gas,gl} = \int_{y_1}^{y_2} P_{gas} y dy = \frac{P_d(y_b^2 - y_a^2)}{2} - \frac{1}{2} \int_{y_1}^{y_2} (y^2 - y_a^2) \frac{dP_{gas}}{dy} dy$$

(3.60)

Substituting (3.58) into (3.59) and (3.60), we obtain the following forms for the force and moment:

$$f_{gaz,gl} = \int_{y_1}^{y_2} P_{gas} dy = P_i \frac{\int_{y_1}^{y_2} \frac{y - y_1}{h_c^3} dy}{\int_{y_1}^{y_2} \frac{dy}{h_c^3}} + P_d \frac{\int_{y_1}^{y_2} \frac{y_2 - y}{h_c^3} dy}{\int_{y_1}^{y_2} \frac{dy}{h_c^3}}$$

(3.61)

$$m_{gas,gl} = \int_{y_1}^{y_2} P_{gas} y dy = \frac{1}{2} P_i \frac{\int_{y_1}^{y_2} \frac{y^2 - y_1^2}{h_c^3} dy}{\int_{y_1}^{y_2} \frac{dy}{h_c^3}} + \frac{1}{2} P_d \frac{\int_{y_1}^{y_2} \frac{y_2^2 - y^2}{h_c^3} dy}{\int_{y_1}^{y_2} \frac{dy}{h_c^3}}$$

(3.62)

Considering groove lower flank angles, we obtain the following components corresponding to the axial force and the additional moment term per unit length.

$$f_{zgas,gl} = f_{gaz,gl} \alpha_{gl}$$

(3.63)

$$m_{zgas,gl} = f_{gaz,gl} h_{li} \alpha_{gl}$$

(3.64)

Similarly, we obtain the following expressions for the forces and moment per unit length acting on the ring from the groove upper flank.

$$f_{gaz,gu} = -P_i \frac{\int_{y_1}^{y_2} \frac{y - y_1}{h_c^3}\, dy}{\int_{y_1}^{y_2} \frac{dy}{h_c^3}} - P_u \frac{\int_{y_1}^{y_2} \frac{y_2 - y}{h_c^3}\, dy}{\int_{y_1}^{y_2} \frac{dy}{h_c^3}}$$

(3.65)

$$m_{gas,gu} = -\frac{1}{2} P_i \frac{\int_{y_1}^{y_2} \frac{y^2 - y_1^2}{h_c^3}\, dy}{\int_{y_1}^{y_2} \frac{dy}{h_c^3}} - \frac{1}{2} P_u \frac{\int_{y_1}^{y_2} \frac{y_2^2 - y^2}{h_c^3}\, dy}{\int_{y_1}^{y_2} \frac{dy}{h_c^3}}$$

(3.66)

$$f_{zgas,gu} = -f_{gaz,gu} \alpha_{gu}$$

(3.67)

$$m_{zgas,gu} = f_{gaz,gu} h_{ui} \alpha_{gu}$$

(3.68)

In addition to gas flow the ring-groove channel, gas pressure also exists beyond the groove wetting region and thus generates force and moment on the ring. Besides, some types of top two rings present a cut on the back of the ring and this also creates axial force. In the ring-liner sub-model, we considered only the radial gas force, while in this sub-model it is the axial one that will be considered. Gas pressure in the land-liner clearance provides both axial and radial force on the ring. The axial contribution is included in the expression that we will develop soon.

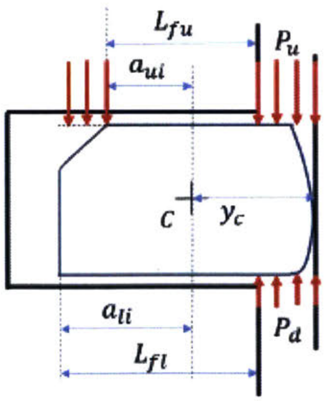

Figure 3.14 – Pressure gas acting on the ring in the axial direction

As shown in Figure 3.14, the axial force and corresponding moment per unit length generated by the gas pressure in ring-liner and ring-groove clearance can be calculated as follows:

$$f_{zgas} = -P_u\left(y_c + a_{ui} - L_{fu}\right) + P_d\left(y_c + a_{li} - L_{fl}\right) - P_i(a_{li} - a_{ui})$$

(3.69)

$$m_{zgas} = -\frac{1}{2}P_u\left(y_c + L_{fu} - a_{ui}\right)\left(y_c + a_{ui} - L_{fu}\right) + \frac{1}{2}P_d\left(y_c + L_{fl} - a_{li}\right)\left(y_c + a_{li} - L_{fl}\right)$$
$$+\frac{1}{2}P_i(a_{li} + a_{ui})(a_{li} - a_{ui})$$

(3.70)

3.3. Thermal moment

In general, during engine operation, the temperature increase of the ring is higher at ring ID than at ring OD, creating a temperature gradient in the radial direction. This temperature difference tends to decease the curvature of the ring. Piston rings producing tip contact concentration under thermal stresses was first studied by Mierbach [41] and his results were used by L. Liu [30]. In that model, the effect of thermal stresses on ring shape was considered equivalent to the effect that would result from applying a bending moment on the ring tip in the axial direction. That explains the high contact pressure and thus the heavy wear that usually occurs around the ring tips. In our study, we compared that modeling to the introduction of the thermal effect along the whole ring, since the temperature gradient between the ID and OD exists all around the ring and not only at the tip. That comparison is given in the results part, under section 3.4.2. To do so, we modified the curvature of the ring appropriately so that we consider the thermal effect before modeling the ring's conformability within the piston, which is different from L. Liu [30] model where he considered the thermal moment as an external force acting only at the ring tips.

As presented in section 2.3, the bending moment along the $\boldsymbol{e}_{zz}$ direction is proportional to the curvature change in the $\boldsymbol{e}_{yy}$ direction (2.45).

$$M_{zz} = EI_{zz}\left(\kappa_{yy} - \kappa_{yy0}\right)$$

(2.45)

Therefore we modify the ring's free shape curvature κ_{yy0}, which is an input to our model by subtracting the term corresponding to the thermal moment effect which gives us the following new ring curvature to consider:

$$\kappa_{yy0}^{n} = \kappa_{yy0} - \frac{M_t}{EI_{zz}}$$

(3.71)

M_t is the thermal moment caused by the non-uniform temperature change in the radial direction. For a ring with a rectangular cross-section as shown in Figure 3.15, the thermal moment can be expressed by the following equation:

$$M_t = \int_{-\frac{a}{2}}^{\frac{a}{2}} y\alpha\Delta T(y)Ebdy$$

(3.72)

$\Delta T(y)$ represents the temperature change at the radial location y compared to the design temperature at that location. α is the ring thermal expansion coefficient and E the ring Young's modulus.

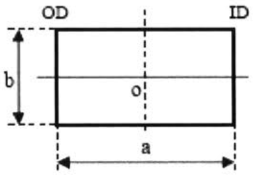

Figure 3.15 – Rectangular ring-cross section dimensions

A linear temperature distribution is assumed along the ring radial direction in our work and the resultant thermal moment is given by the following relation:

$$M_t = \frac{1}{12}\alpha Eba^2(\Delta T_{ID} - \Delta T_{OD})$$

(3.73)

ΔT_{ID} and ΔT_{OD} are the temperature changes at the ring ID and OD respectively.

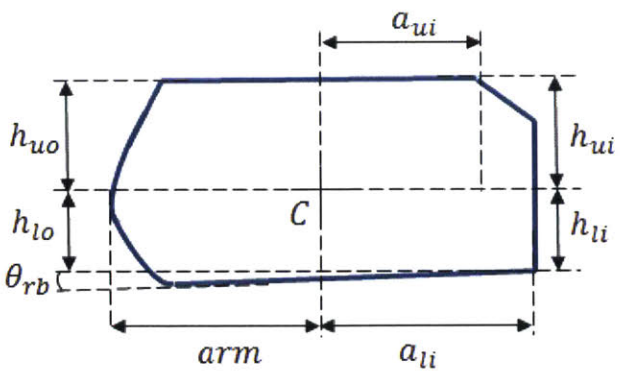

Figure 3.16 – Ring-cross section dimensions

We have all the necessary equations (3.71) and (3.73) to model the thermal moment effect, except that these results are for rectangular cross section rings. For more general geometries as the one presented in Figure 3.16, we still apply the equations (3.71) and (3.73) where we make the approximation of substituting a and b by the following expressions:

$$a = arm + \max(ali, aui)$$

(3.74)

$$b = h_{ui} + a_{ui}\theta_{rt} + h_{li} + a_{li}\theta_{rb}$$

(3.75)

All the geometric variables are presented in Figure 3.16. θ_{rb} and θ_{rt} are the ring lower and upper flank angles respectively and are assumed to be small enough to apply the first order approximation in equation (3.75).

3.4. Sample results

We use the conformability model to study the effects of different features. We analyze the effect of the gap location inside distorted bore in terms of the ring-liner conformability. This will give us an idea on one of the reasons behind increasing the ring-liner clearance knowing that ring rotation is generally very limited in working engine conditions. In addition, we compare the results of our modeling of the thermal moment, where we modify the ring free shape curvature, and the modeling of the thermal effect by applying a bending moment on the ring tips in the axial direction, which was introduced by Mierbach [41] and used by L. Liu [30]. Besides, we study the effect of introducing local oil distributions on liner and groove flanks and their effect on the ring deformation. Finally, we look at the ring groove conformability depending on the gas pressure force and the friction one when they have opposite directions. The magnitude of these two forces determine the equilibrium position of the ring within the groove: either stable on the lower or upper flank.

3.4.1. Gap location effect inside distorted bore

When the bore experiences thermal and mechanical stresses, it distorts to a non-circular shape with local minimum and maximum radial distances with its initial nominal center. It is customary to describe the geometry of a distorted bore with a discrete Fourier series used to interpolate the deformation of sections of the cylinder perpendicular to the cylinder axis as presented by equation (3.76).

$$y_b(\theta) = A_0 + \sum_{k=1}^{n} A_k \sin[k(\theta + \phi_k)]$$

(3.76)

y_b represents the radial displacement of the distorted cylinder from the nominal cylinder, k is the order of distortion and A_k and ϕ_k are the magnitude and phase of distortion of order k respectively. A cylinder distortion of order 0 corresponds to a change of radius that is uniform along the cylinder circumference due to the expansion of the cylinder when the engine block is heated under operation. The 1st order distortion gives eccentricity to the cylinder (displacement of its axis). The 2nd order quantifies the ovality of the distorted cylinder. A 3rd order distortion has three lobes of deformation equally spaced around the circumference, the 4th order has four and so on. For engines with 4 in-line cylinders for instance, the outside of the block is cooler than the center resulting in the 2nd and 3rd order thermal distortions. When the 4 bolts surrounding the cylinder are tightened to assemble the engine block, it results in mechanical deformations corresponding 4th order distortion. Fourier series provides a convenient way of separating different contributions of the shape of the distorted bore. These distortions can be obtained from thermal-mechanical finite element simulations of the engine block whose boundary conditions take into account the fastening of the engine block and the heat contribution from combustion and cooling of the block. Most sever conditions for bore distortion are obtained for open-deck engines under high load and high speed conditions. Generally, cylinder deformation occurs at distortion orders between 0 and 4. Higher order distortions get closer to the liner roughness scale and the limit of precision of the finite element simulation is reached.

In our simulation, we model a diesel engine with a nominal bore radius equal to $95.25\ mm$. We use a ring with a rectangular cross section of dimensions $4mm\ x\ 2\ mm$ and a parabolic profile at the running face. The ring has a free shape designed to have uniform pressure distribution at a round shape with a ring tension of $25.4N$.The cylinder and ring are chosen in stainless steel. We consider no oil on the groove flanks and an incoming uniform oil film on the liner with a thickness equal to $5\sigma_p = 1.5\ \mu m$, where σ_p is the liner surface roughness standard deviation. The oil viscosity as a function of the liner temperature considered uniform and equal to $150^\circ\ C$ is given by our sponsor from Shell. We consider a liner speed equal to $10\ ms^{-1}$ and directed upward with a zero acceleration. Based on the notation used in Figure 3.3 we take $P_u = 96200\ Pa$, $P_i = 96200\ Pa$ and $P_d = 90670\ Pa$. We consider bore distortion up to 4th order: the 0 order amplitude is of order of $100\ \mu m$, the second one of order of $20\ \mu m$, the third one of $10\ \mu m$ and the fourth one of $1\ \mu m$.

Based on the location of the ring gap with respect to the cylinder, the ring liner clearance presents different profiles. We refer to the angular position for the ring gap within a fix coordinate system with respect to the cylinder directed from thrust side (0°) to thrust side (360°). Using that coordinate system, in Figure 3.17 we plot the radial distance of the distorted bore and the two ring tips (the left side corresponds to the tip that one observes at the left when located at the bore center and directed towards the ring gap and respectively for the right side) with respect to the nominal non distorted bore radius. When the gap is located in the vicinity of a cylinder point with a local maximum radial coordinate, the ring is well conform to the liner as we can see in Figure 3.17 and in Figure 3.18 and 3.19 for a gap location at the angles 165° and 201° respectively with ring-liner clearances less than $1.5\ \mu m$ and $3\ \mu m$ respectively. For the radial plots we use a magnification coefficient of 1500 for the bore distortion and ring deformation.

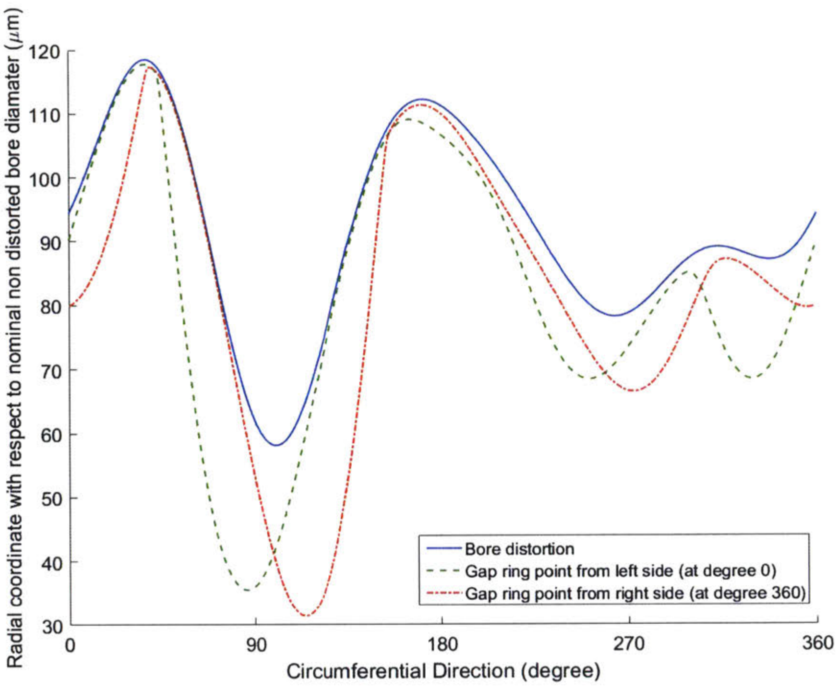

Figure 3.17 – Ring tips radial coordinates for different ring gap locations

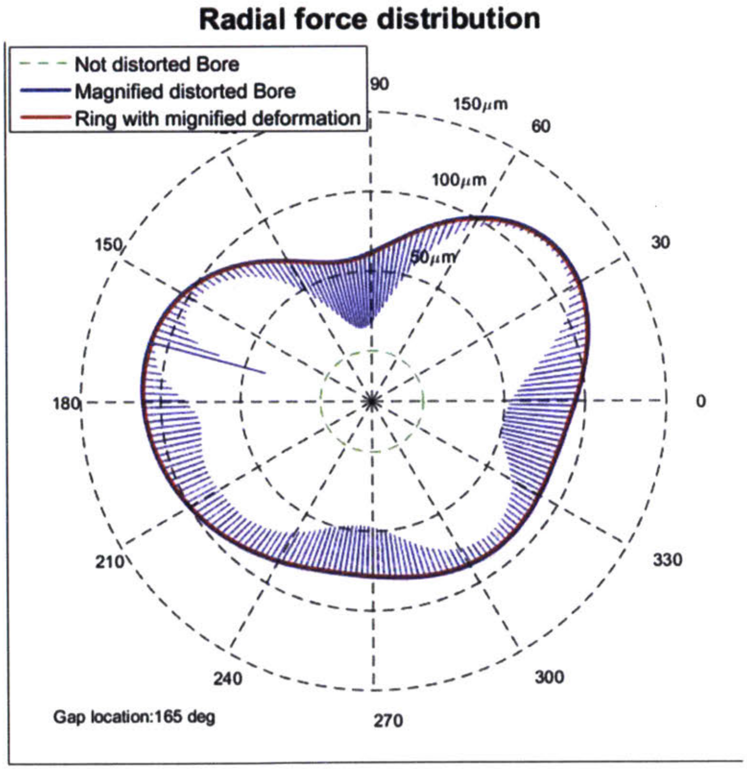

Figure 3.18 – Ring and bore in radial coordinate for a gap located at 165°

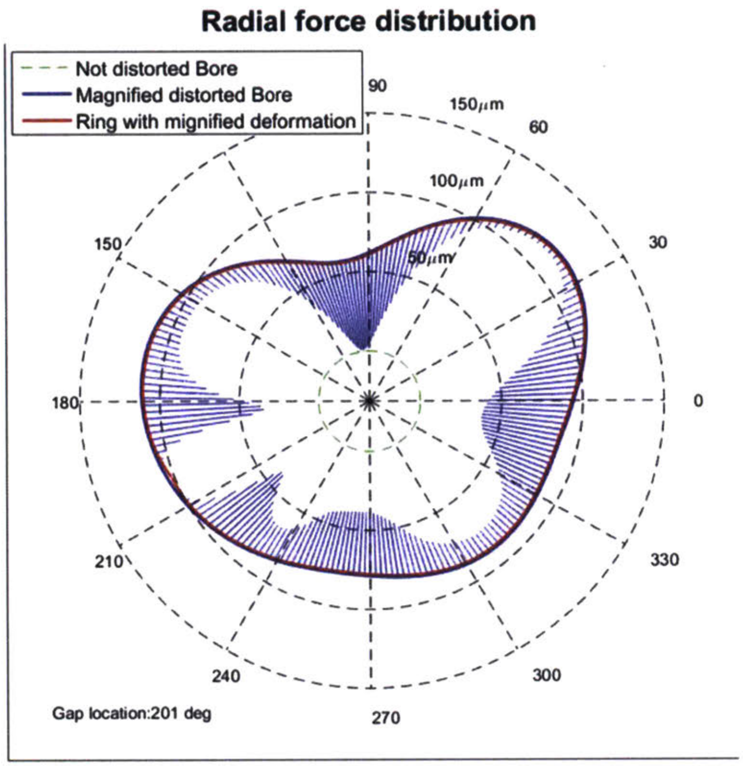

Figure 3.19 – Ring and bore in radial coordinate for a gap located at 201°

On the other hand, when the ring gap is located in the vicinity of a cylinder point with a local minimum radial coordinate, the ring presents a high clearance with the cylinder since its stiffness does not let it conform well with the local curvature of the cylinder as we can see in Figure 17 and in Figure 3.20, 3.21 and 3.22 for a gap location at the angles 90°, 98° and 118° respectively with maximum ring-liner clearances around $20\ \mu m$. For the radial plots we use a magnification coefficient of 1500 for the bore distortion and ring deformation. These clearances compared to the oil film thickness considered of $1.5\ \mu m$ show very limited oil control performances and a major reason of oil consumption increase. Since ring rotation along the circumferential direction is limited, its insertion within the cylinder should be done carefully so that its gap is in the vicinity of a cylinder point with a local maximum radial coordinate or even with a global maximum since bore distortion can be estimated in advance, within a certain error, based on its thermal and mechanical deformations causing these distortions.

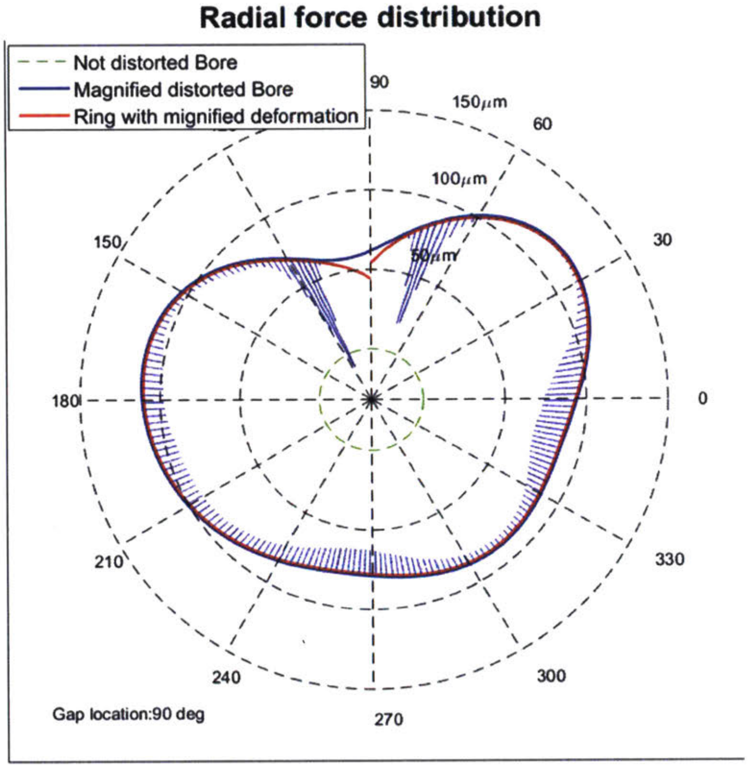

Figure 3.20 – Ring and bore in radial coordinate for a gap located at 90°

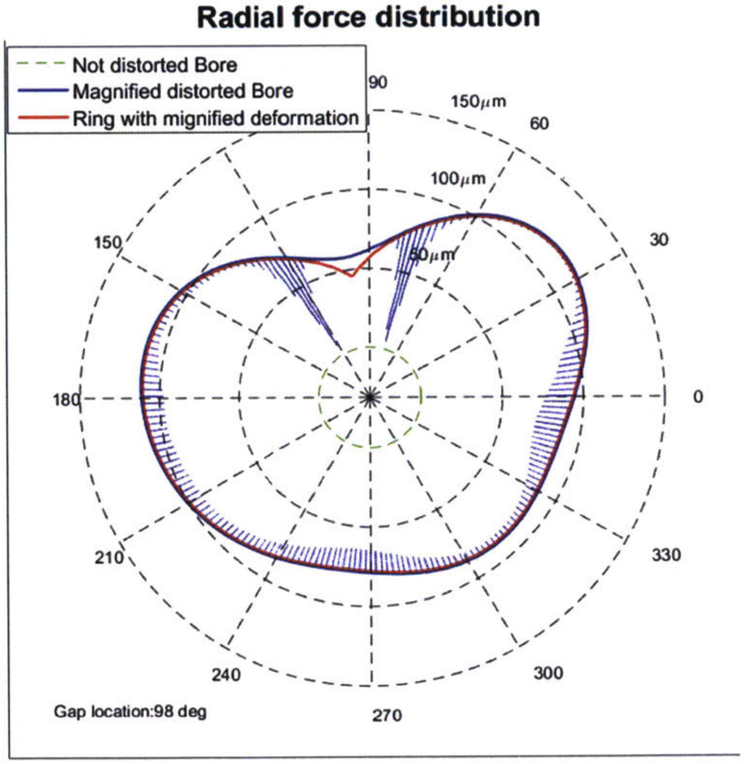

Figure 3.21 – Ring and bore in radial coordinate for a gap located at 98°

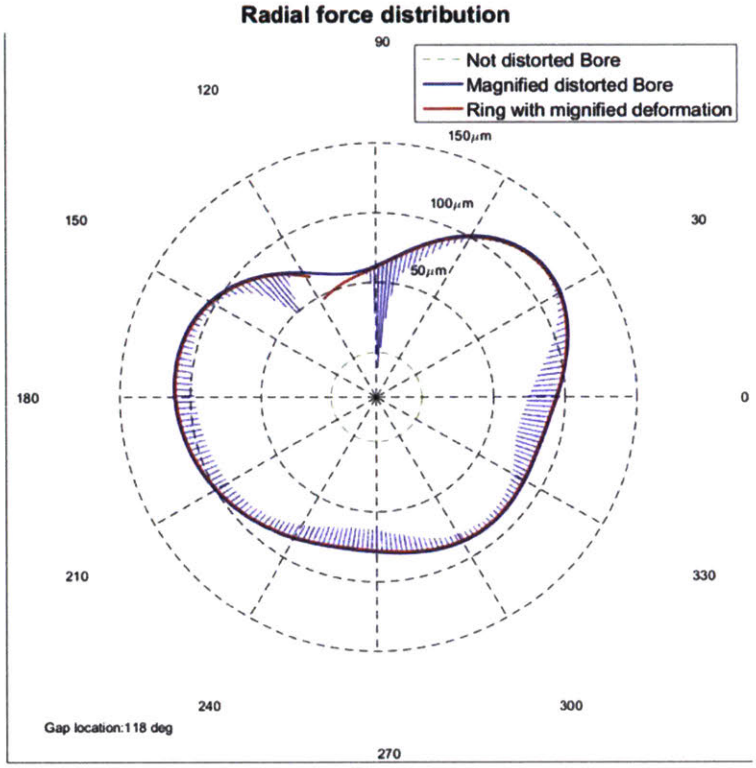

Figure 3.22 – Ring and bore in radial coordinate for a gap located at 118°

For the rest of this section 3, all graphs presenting variables as a function of the circumferential direction are given with respect to a coordinate system defined based on the ring: angles 0° and 360° correspond to the ring tips and 180° corresponds to the ring back. The ring gap static position also affects the radial force distribution. When the ring is not well conform to the liner, we have larger regions of no-contact. Therefore in these regions, the ring running face is submitted to the gas pressure (the highest among the upper and lower one) which is the same as the gas pressure in the inner groove region which is noted by P_i. Therefore the overall radial force in these regions is zero. However the average radial force along the ring circumference is almost the same for all the cases corresponding to different ring gap locations and is around the theoretical constant pressure needed to close the ring gap. Therefore larger no-contact regions mean higher radial force peaks to have the same average value. Thus, for gap location where the ring-liner clearance is high, apart from the oil control issues mentioned previously, we have high local contact forces and thus wear problems. This is confirmed by Figures 3.23 and 3.24 where we plotted the radial force and local stress distributions (at upper/lower ID/OD points for each cross section) respectively for the static position obtained when the ring gap is located at 98° (higher clearance and thus higher radial force and higher local stresses) and 201° (lower clearance and thus lower radial force and lower local stresses).

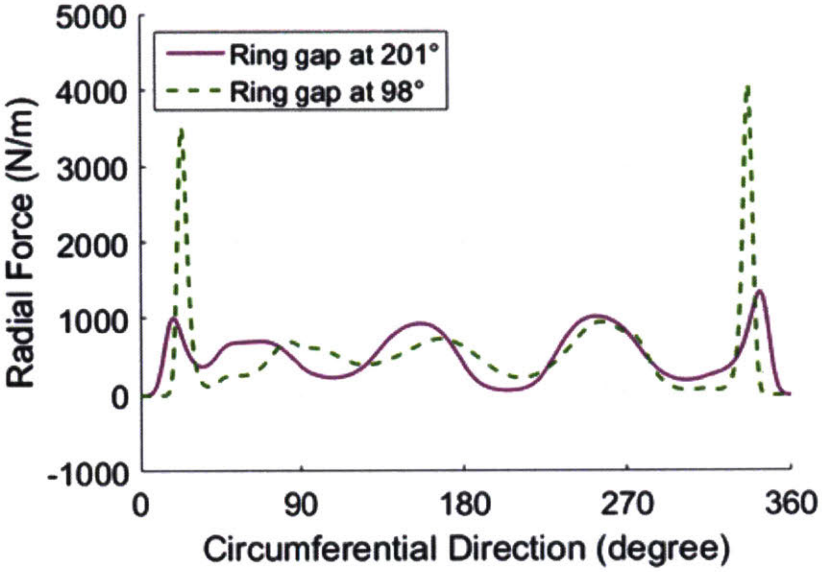

Figure 3.23 – Force distribution comparison for a gap located at 98° and 201°

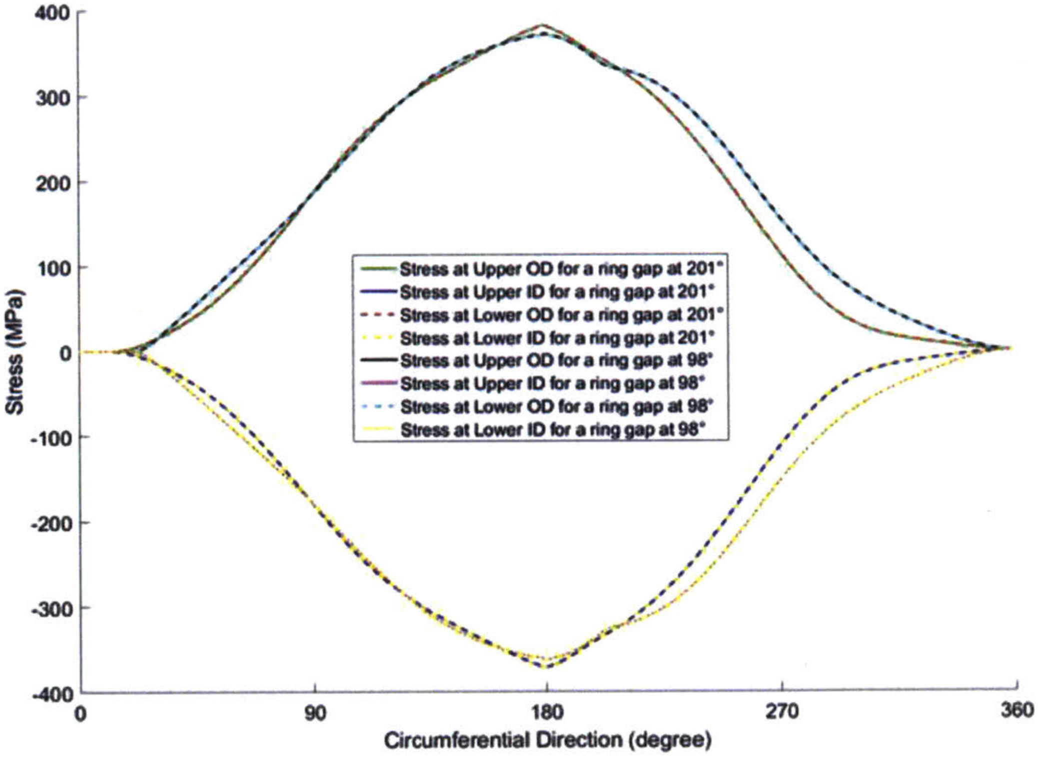

Figure 3.24 – Stress distribution comparison for a gap located at 98° and 201°

3.4.2. Thermal moment effect

In this section we compare the results obtained with our modeling of the thermal moment introduced in section 3.3, where we modify the free shape curvature as expressed by equation (3.71), and the modeling used by L. Liu [30] where the thermal moment effect is only introduced at the ring tips.

In our simulation, we model the same diesel engine considered in section 3.4.1 with the exact same conditions. The ring gap location is taken equal to 192° so that the ring liner clearance is less than the oil film thickness ($1.5\ \mu m$) along almost the whole ring circumference, which guarantees the ring liner contact and creates the radial temperature gradient. We present the results obtained with the two models for a uniform radial ring temperature gradient equal to $15^\circ C$ and compare them to the results obtained without radial temperature gradient.

Figure 3.25 shows the ring liner clearance obtained with two models. Close to the ring tips the two models give the same results which proofs the equivalence between modifying the ring free shape curvature based on the thermal moment and introducing it as an external load. However the old model only consider the thermal moment effect close to the ring tips. This is a good approximation provided that the ring is well conform to the liner along its whole circumferential direction apart from the tips regions. However when the ring liner clearance is high enough at any point along the ring circumference, the old model is likely to give biased results as we can see in Figure 3.25 around the local maximum clearance reached between angles 180° and 270°. In fact the radial temperature gradient exists all around the ring especially when its clearance with the liner is small enough to have lubrication or dry contact with the liner, which is the case here. Thus, thermal moment effect has to be considered along the whole circumference direction and in particular in the region around the local maximum clearance occurring between 180° and 270°. Indeed the old model gives exactly the same solution obtained without temperature gradient while our model takes into account the thermal bending moment and gives a lower clearance with the liner. It is true that the difference between the two models in this case is small enough and could be neglected but in some extreme cases where we have high bore distortions and large ring-liner clearances in points far from the ring tips, the thermal moment effect can be significant in those regions and the results obtained with the old model will not be accurate. Besides, computationally our model is slightly more advantageous since we do not have to evaluate the external thermal load at each iteration of the Newton-Raphson algorithm but we just change the free shape curvature and the initial loads accordingly before iterating.

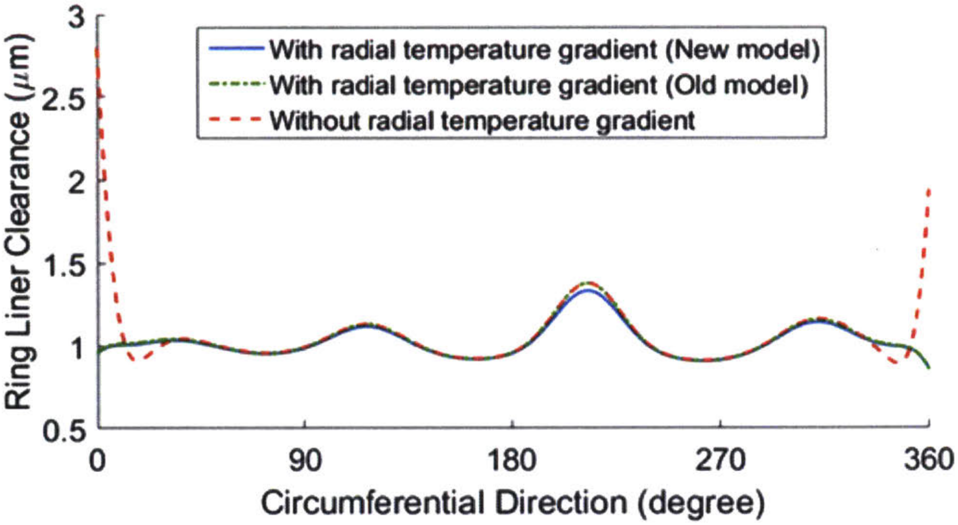

Figure 3.25 – Ring-liner clearance with and without radial temperature gradient

We also verify the results obtained for the radial force distribution given in Figure 3.26. As expected, since the thermal moment results in a ring expansion decreasing the ring liner clearance, we obtain higher radial force in regions where the clearance has been affected the most which corresponds to points close to the ring tips. Figure 3.27 gives the stress distributions obtained at the upper/lower ID/OD points of each cross section with the temperature gradient using our new model and without the temperature gradient and as for the radial force distribution we verify that we have higher stresses (in absolute values) when we have a non-zero temperature gradient. The difference between the two stresses correspond to the thermal stress.

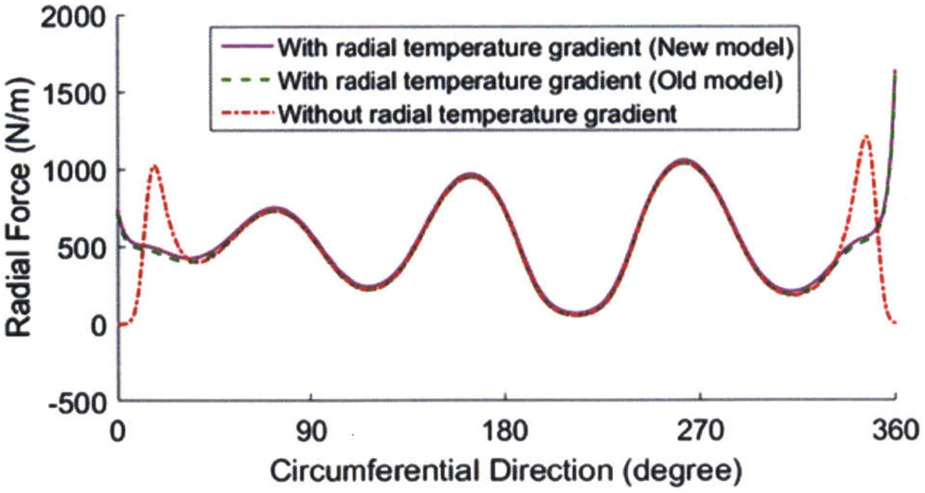

Figure 3.26 – Radial force distribution with and without radial temperature gradient

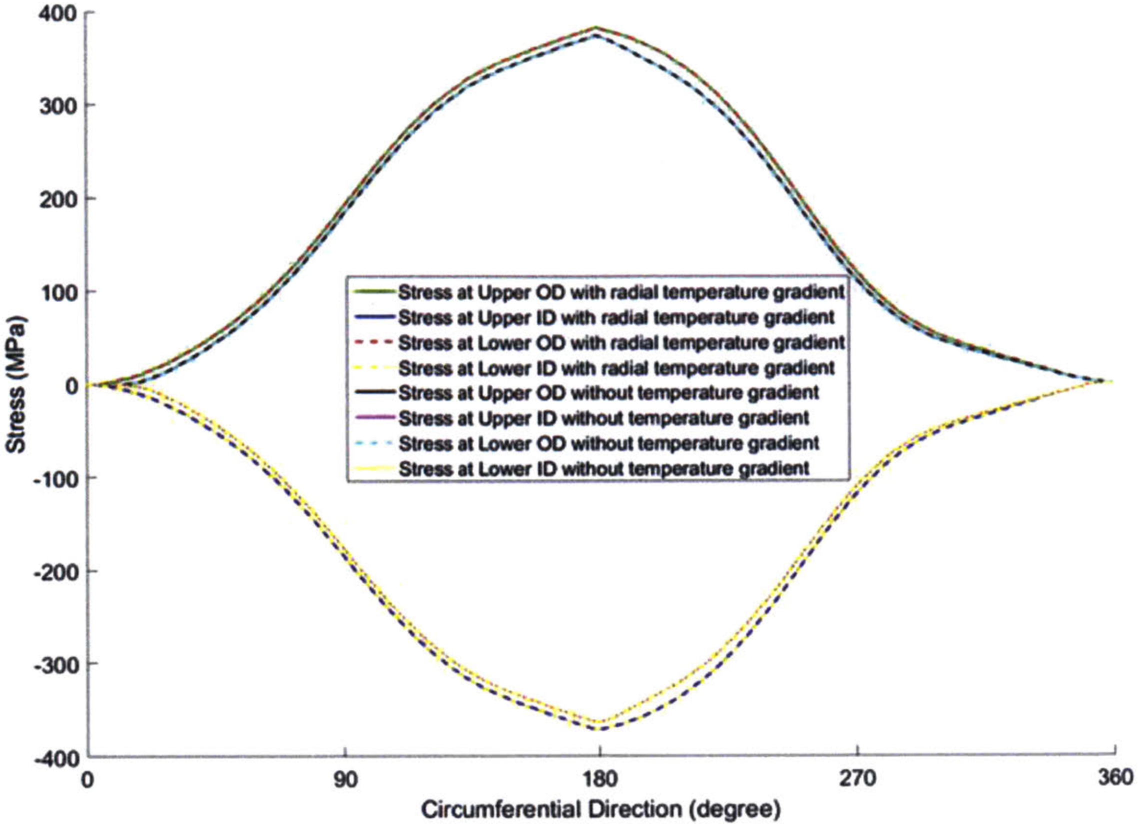

Figure 3.27 – Stress distributions with and without radial temperature gradient

In the rest of this section we keep using the same parameters mentioned previously except for the ring free shape that is no longer designed to have uniform pressure distribution at a round shape with a ring tension of $25.4N$ but instead we use the TC design developed by Mahle and studied by Tomanik [47]. The corresponding free shape and curvature are given in Figure 3.28.

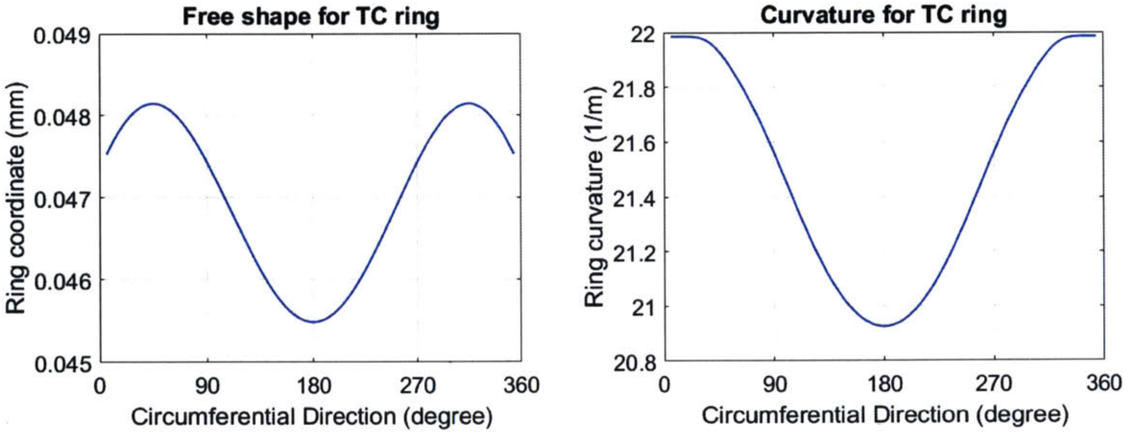

Figure 3.28 – TC ring free shape and curvature

As we can see this ring is designed to have the highest curvature at the tips and a decreasing radial coordinate when we are close to them. This is intended to make the ring-clearance higher at the tips and thus decrease the wear effect which is maximum in general at these location. Besides, when experiencing radial temperature gradient, this design is intended to give the ring a shape close to the circular one once inserted in the cylinder. Using the same distorted bore as in Section 3.4.1 and the previous part of this section, we verify the performance of this design by looking at the ring-liner clearance and radial force for different temperature gradients. We also simulate the same ring with the same parameters but without bore distortion. For the distorted bore the ring gap is located at the angle 98° as we can see in Figure 3.32 where the bore distortion and ring deformation are magnified with a coefficient of 3000. This coefficient has also been used for the rest of radial plots given in this section. For that ring tip location the clearances, and thus the forces generated, at the two ring tips are almost the same. Figure 3.29 show the radial force at the ring tip for different radial temperature gradient for the two simulations. As we can see, the TC ring does well prevent high force generation at the ring tips when it is inside the distorted bore up to high temperature gradients, around $50^\circ C$ since its gap is well located in the vicinity of a cylinder point with a local minimum radial coordinate (here it is a global one) making the clearance at the gap even higher than what is obtained thanks to the ring design as explained in Section 3.4.1. However, then the ring is inserted in a non-distorted bore, the force generation at the tips increased significantly even for temperature gradients of the order of $8^\circ C$. This shows that the TC design is well suited to prevent high force generation at the tips, provided it is coupled with bore distortion effects as we can see from Figures 3.30 and 3.31 showing the radial plots of the ring without temperature gradient for the two cases.

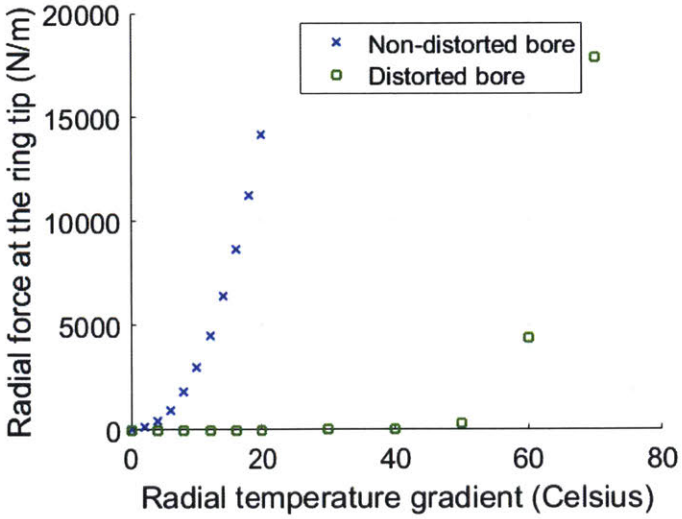

Figure 3.29 – Temperature gradient influence on radial force at the ring tip for the TC design

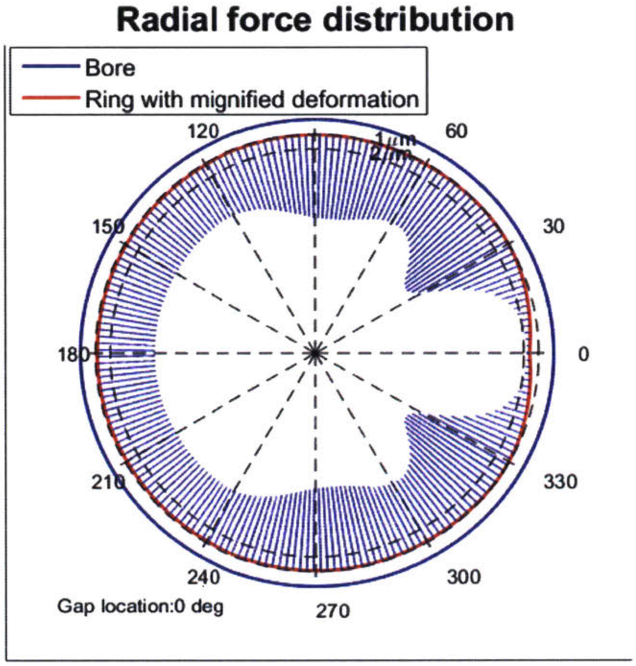

Figure 3.30 – Radial plot of the TC ring within non-distorted bore and without temperature gradient

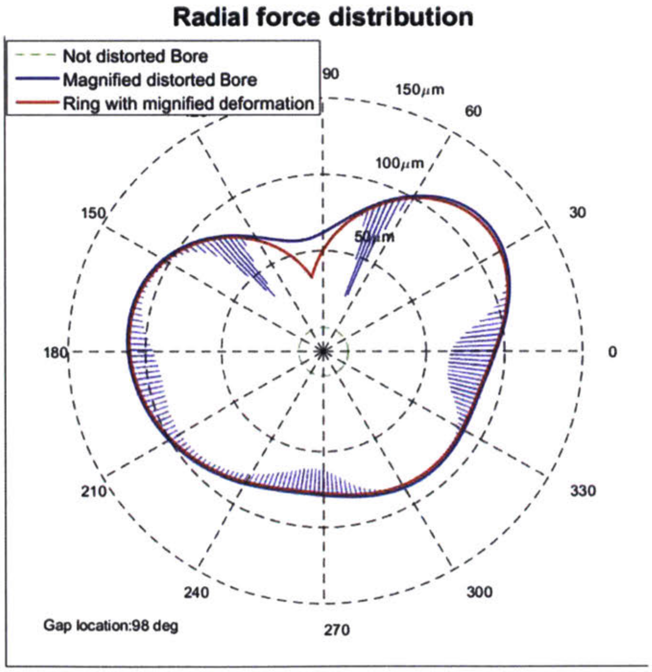

Figure 3.31 – Radial plot of the TC ring within distorted bore and without temperature gradient

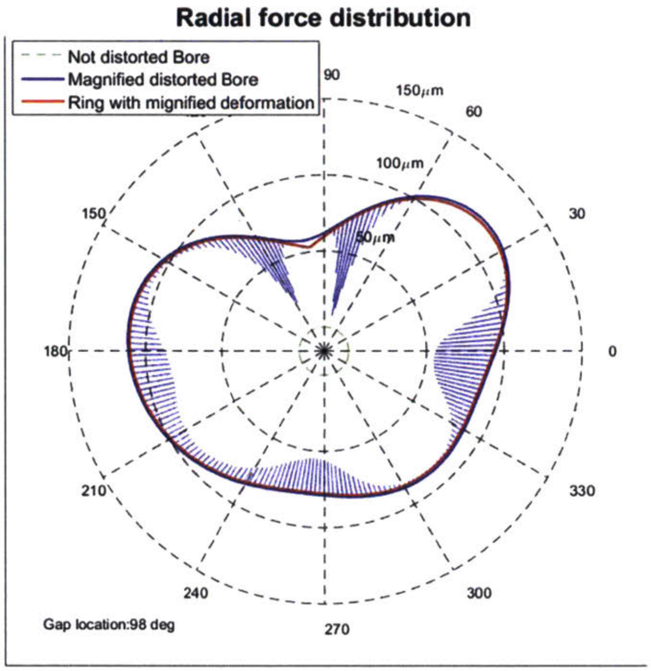

Figure 3.32 – Radial plot of the ring within distorted bore and with a temperature gradient equal to 30°C

Nevertheless, we should keep in mind that we are using relatively large cylinder and ring making the thermal effect more significant than what we should obtain for smaller engines. Figure 3.33 gives the ring-liner clearance at the tip for the same temperature gradients considered in Figure 3.29 for the two simulations. We can see that the clearance decreases less fast within the distorted bore which is coherent with the observations made for the force generation.

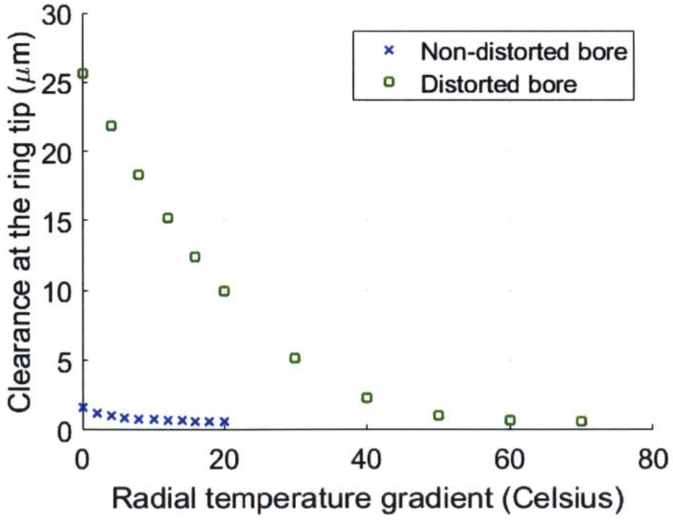

Figure 3.33 – Temperature gradient influence on ring-liner clearance at the tip for the TC design

For the non-distorted bore, the clearance without temperature gradient is already small compared to the length scale of the relative ring-liner clearance generating the contact force. Thus even for small temperature gradient, the force generated at the tips is already high. Figure 3.30 and 3.34 give the radial plot of the ring without bore distortion for a zero temperature gradient and a gradient of $6^\circ C$ respectively. In Figure 3.34, we see that the tip orientation has already changed unlike the behavior observed in Figure 3.32 for a higher temperature gradient ($30^\circ C$) but with a distorted bore.

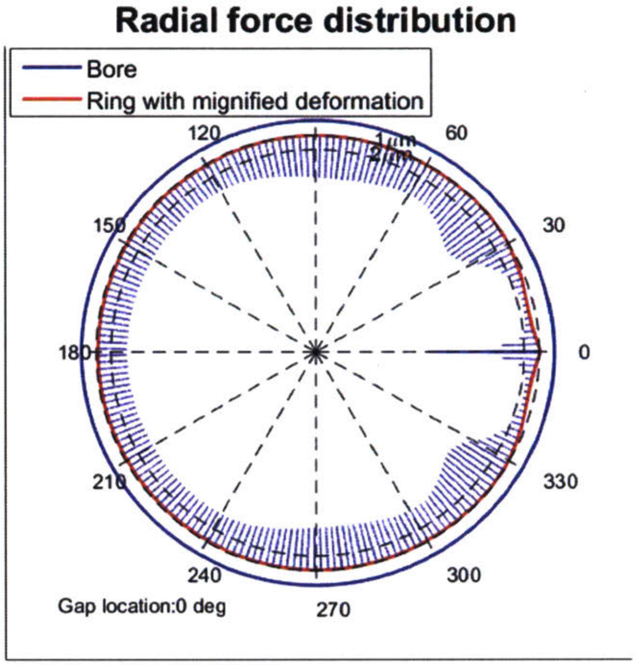

Figure 3.34 – Radial plot of the TC ring within non-distorted bore and with a temperature gradient equal to 6°C

Figure 3.35 gives the ring-liner clearance and radial force along the ring circumference for a non-distorted bore with temperature gradients equal to $0^\circ C$, $4^\circ C$ and $6^\circ C$, while Figure 3.36 gives the same plots for a distorted bore with temperature gradients equal to $0^\circ C$, $30^\circ C$ and $6^\circ C$. We observe that the non-contact region only exists for the distorted bore case and shrinks when the radial temperature gradient increases till vanishing for a gradient around $50^\circ C$, while this non-contact region is inexistent for the non-distorted bore case. The TC design prevents well high force generation at the tips when submitted to radial temperature gradients provided the gap is located in the vicinity of a cylinder point with a local minimum radial coordinate. Otherwise the force generation is likely to start even with relatively low temperature gradient, especially for large piston rings.

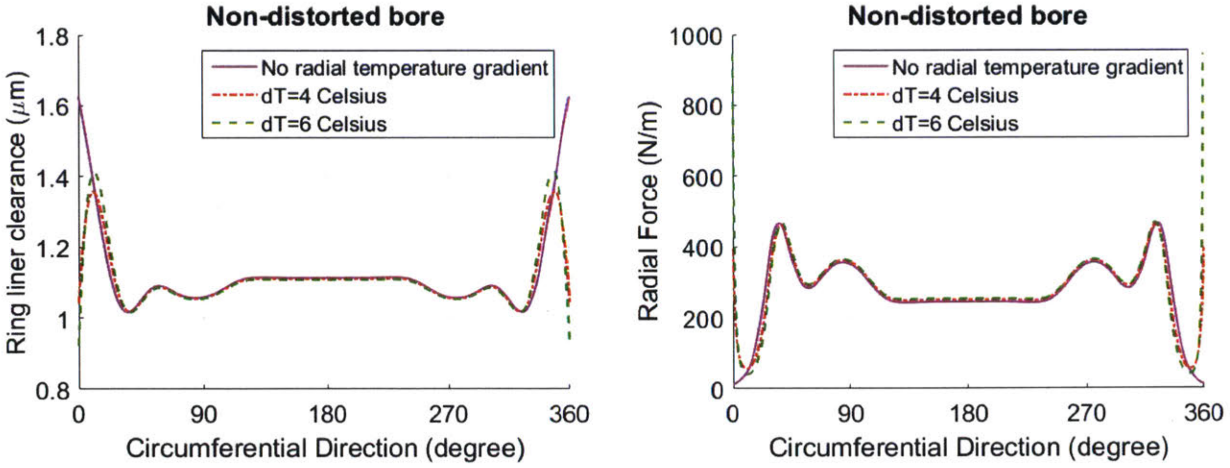

Figure 3.35 – Ring-liner clearance and radial force for the TC ring within non-distorted bore for different temperature gradients

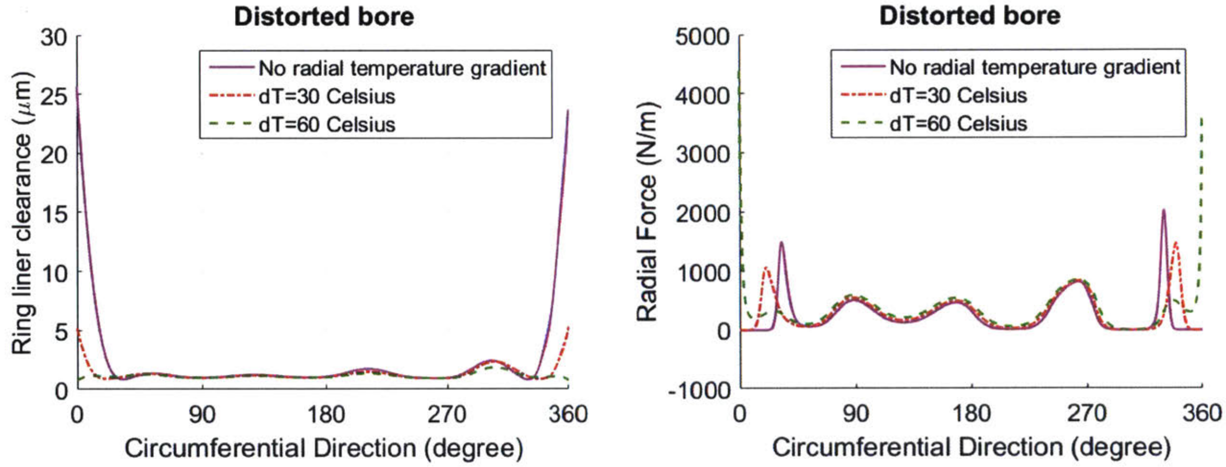

Figure 3.36 – Ring-liner clearance and radial force for the TC ring within distorted bore for different temperature gradients

3.4.3. Local oil distribution

In this section we study the effect of variable oil distributions on the liner and/or groove flanks with local peaks. As we will see, the effect of these distributions varies depending on the location of the peaks with respect to the ring gap position.

In the simulations run for this section 3.4.3, we model a diesel engine with a nominal bore radius equal to 95.25 mm. We use a ring with a rectangular cross section of dimensions $4mm\ x\ 2\ mm$ and a parabolic profile at the running face. The ring has a free shape designed to have uniform pressure distribution at a round shape with a ring tension of $25.4N$. The cylinder and ring are chosen in stainless steel. We consider a liner and groove surface roughness standard deviations equal to $\sigma_p = 0.3\ \mu m$. The oil viscosity as a function of the liner temperature considered uniform and equal to $150°\ C$ is given by our sponsor from Shell. We consider a liner speed equal to $10\ ms^{-1}$ and directed upward with a zero acceleration. Based on the notation used in Figure 3.3 we take $P_u = 1.1\ Bar$, $P_i = 1.1\ Bar$ and $P_d = 1\ Bar$. We consider a circular bore with no distortions.

3.4.3.1. Local oil distribution on liner

We compare the ring-liner clearance and radial force for different variable oil distributions on the liner with a uniform one of a thickness equal to $0.54\ \mu m$. The variable oil distributions are Gaussian functions with a plateau value equal to $0.54\ \mu m$ and a maximum value of $0.84\ \mu m$ as shown in Figure 3.37. The difference between these oil distributions is the location of the peak. As mentioned earlier the angle $0°$ corresponds to the ring gap location.

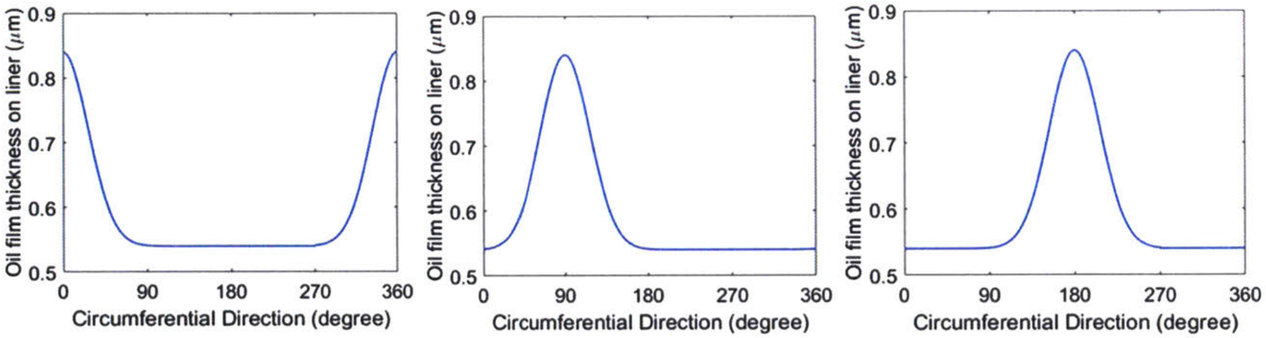

Figure 3.37 – Variable oil distributions on the liner

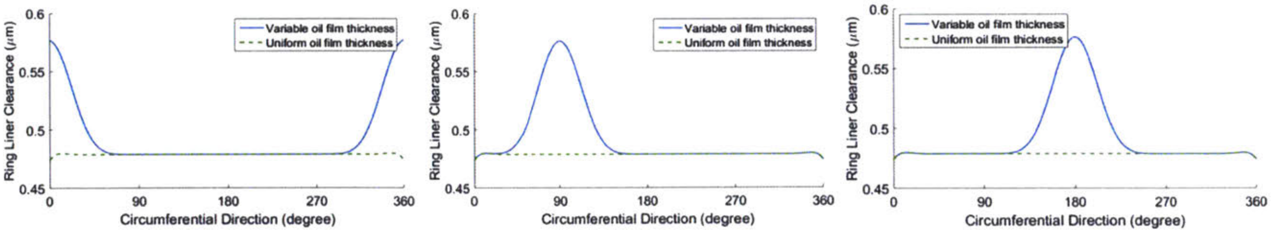

Figure 3.38 – Ring-liner clearance for variable oil distributions on the liner with peaks at 0° (left), 90° (center) and 180° (right)

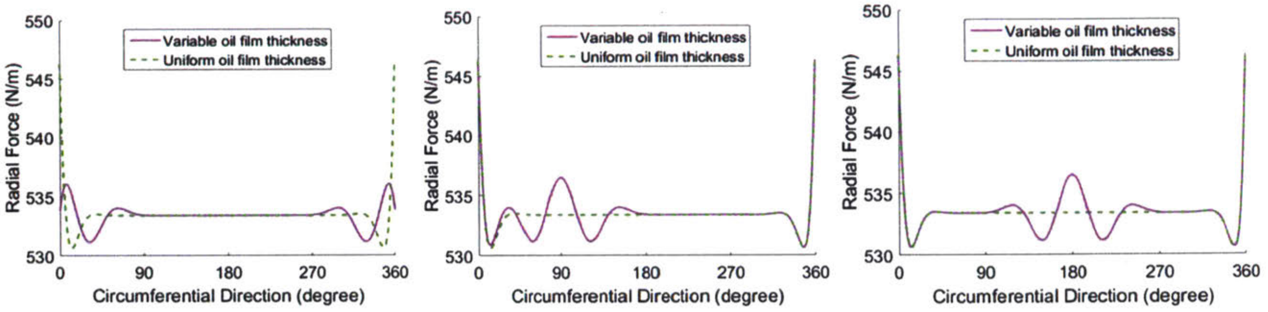

Figure 3.39 – Radial force for variable oil distributions on the liner with peaks at 0° (left), 90° (center) and 180° (right)

As we can see from Figure 3.38, the increase in the ring-liner clearance due to the variable oil distribution is independent of the location of the oil distribution peak. However the radial force distribution does depend on that location. If the peak is not at the ring gap, we have a certain fluctuation in the force distribution around the peak as we can see in the center and right graphs of Figure 3.39 and the force is not changed around the ring tips compared to the uniform oil film thickness case. For these two cases, we obtain a higher force at the exact location of the oil peak since we have a higher hydrodynamic force due to the larger oil film thickness but then we reach lower values around it since the average force along the circumferential direction has to be the same as in the uniform oil film thickness case. When the oil peak is located at the ring tips, the ring-liner clearance changes from reaching a minimum value at the tips to a maximum one as we can see in the left graph of Figure 3.38. For the uniform oil film thickness, the radial force increase close to the tips is governed by the dry contact one. Therefore, when we have an oil thickness peak at the ring gap, the radial force will become more dominated by the hydrodynamic one than by the dry contact one. Given the oil film thickness, the final radial force presents a lower value at the ring tips when it is dominated by the hydrodynamic force. As a conclusion, the oil distribution with a peak at the ring gap gives a smoother radial force distribution and prevents reaching high values at the ring tips. This is advantageous for the wear effect that is usually more significant at the tips than in other regions along the ring circumference. However, since the ring gap is non-zero, this peak oil distribution will increase oil consumption.

The curved beam model is useful in the sense that it relates the global and local behavior of the ring while depending on different length scales. As we have seen in section 3.4.1, our static model determines the ring structural response under the effect of bore distortion, which represents the global behavior. The local behavior is determined by the response of the ring to different local contact boundary conditions such as bridging and lube-fuel interaction. In this part, we will focus on the ring response to bore distortion and local oil accumulation on the liner which affects the global and local behavior of the ring respectively.

In the simulations run for the rest of this section 3.4.3.1, we model an engine with a nominal bore radius equal to $82.51\ mm$. We use a ring with a rectangular cross section of dimensions $3\ mm\ x\ 1.5\ mm$ and a parabolic profile at the running face. The cylinder and ring are chosen in stainless steel. We consider a liner surface roughness standard deviation equal to $\sigma_p = 0.07\ \mu m$. The oil viscosity as a function of the liner temperature considered uniform and equal to $150^\circ\ C$ is given by our sponsor from Shell. Based on the notation used in Figure 3.3 we take $P_u = 1.1\ Bar$, $P_i = 1.1\ Bar$ and $P_d = 1\ Bar$. We consider bore distortions up to 4th order with a 0th order distortion of magnitude equal to $80\ \mu m$, a 2nd order one equal to $10\ \mu m$ and a 4th one equal to $2\ \mu m$. Local oil accumulation on the liner can happen around the bottom dead center during the intake and expansion strokes and around the top dead center during the compression and exhaust strokes and may result in bridging. Inertial and viscous forces bring oil from the piston to the liner causing this local oil accumulation and its range varies from sub-millimeters to tens of millimeters [42] [43] [44] [45].

In our case we consider a local oil accumulation centered at 90° away from the thrust side which coincides with the ring gap and with a width of 20°. Outside of this accumulation region, oil thickness if fixed to the value of: $2\sigma_p = 0.14\ \mu m$ as plotted in Figure 3.40.

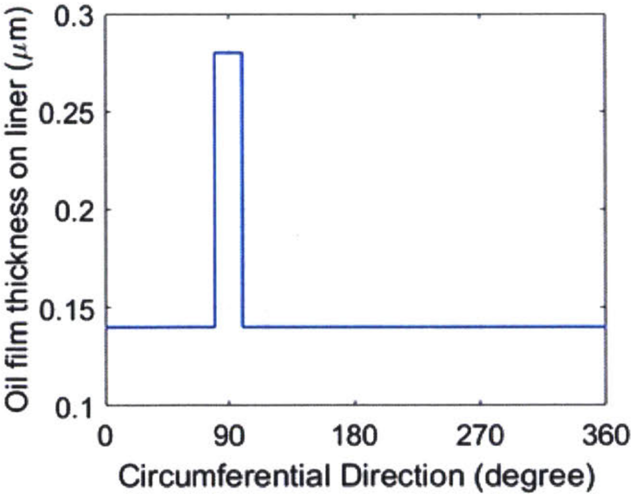

Figure 3.40 – Local oil accumulation on the liner for partially flooded case

We vary the oil film thicknesses at the peak and change the liner velocity correspondingly so that to have the same local Reynolds number within the oil accumulation region. Therefore we can determine the change in the liner force and in the ring-liner clearance depending on the oil film thickness at the peak. We plot the difference between the maximum and minimum of the force distribution within the region where we have the oil accumulation and the maximum ring liner clearance obtained within that region as function of the difference between the oil film thickness in the accumulation region and the rest of the liner. The difference between the force values is divided by the average of the ring-liner force which is constant here since the gas pressure in the inner region is the same in all the simulation and thus this average value only depends on the ring stiffness, its free shape and the liner surface roughness standard deviation which are all maintained the same. Besides the difference between the oil film thicknesses and the maximum ring-liner clearance are also made non dimension by dividing them with respect to the liner surface roughness standard deviations. Figure 3.41 and 3.42 show the difference considered for the liner force that is introduced by the local oil accumulation corresponding to Figure 3.40 and the ring liner clearance obtained respectively. These results represent a partially flooded case. The tradeoff is first arbitrary and defined as a ratio between the oil film thickness and the liner surface roughness standard deviation above which we reach the fully flooded boundary condition. In our simulations we fixed at 10 first. Figure 3.43 shows the liner force distribution and the ring liner clearance obtained for fully flooded boundary condition within the oil accumulation region corresponding to Figure 3.44. In this case, the hydrodynamic pressure generation ability of the ring increases compared to the partially flooded case and thus results in a higher ring-liner clearance at the oil peak location. The region where we have the increase in the ring-liner clearance around 90° corresponds to the bridging area. As for the partially flooded case, the discontinuous oil supply generates a discontinuous liner force distribution. Since the dry contact force and hydrodynamic one are very sensitive to the ring-liner clearance at small oil film thickness, we obtain large spikes around the boundary of the bridging area. Because of the stiffness, the ring neutral axis cannot change rapidly. While the ring is able to conform to the bore when we have partially flooded boundary condition, around the bridging area we obtain a narrow range where the ring loses contact with the liner in the fully flooded case. The effect of bridging and local oil accumulation in general stays locally and does not affect significantly the ring neutral axis deformation or the liner force distribution outside the oil accumulation region.

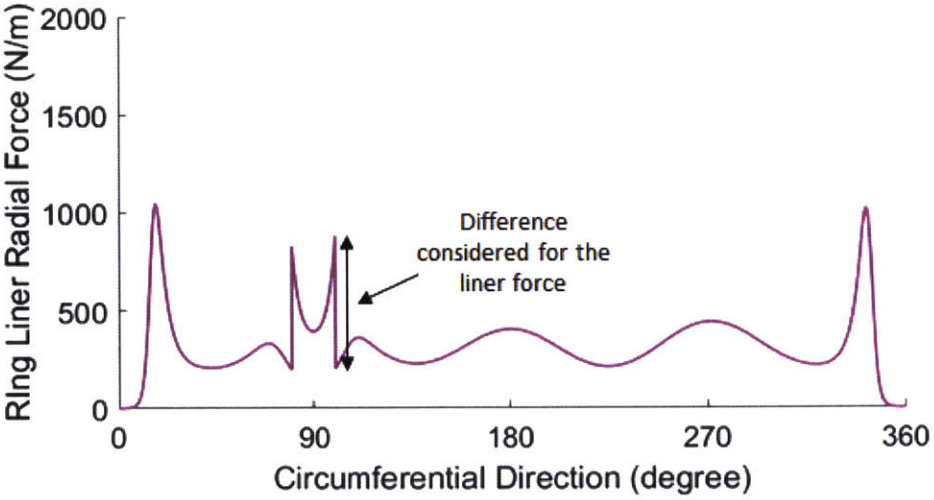

Figure 3.41 – Liner force distribution for partially flooded boundary condition

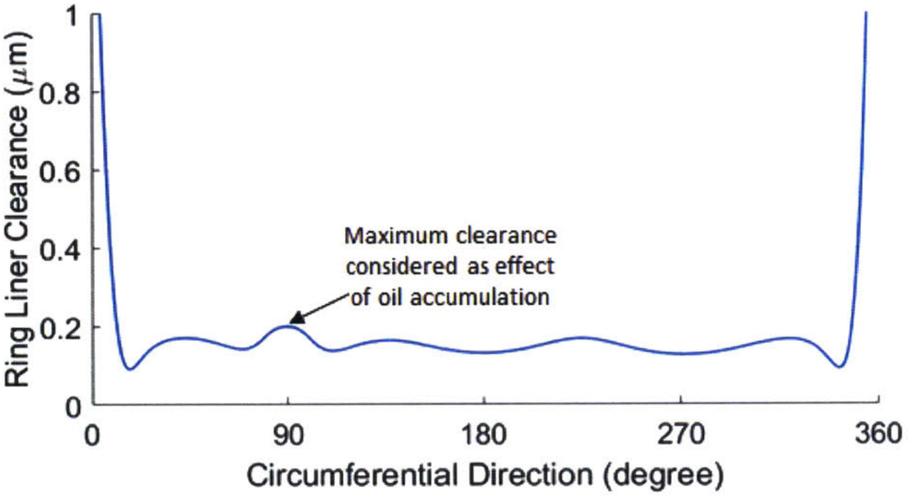

Figure 3.42 – Ring-liner clearance distribution for partially flooded boundary condition

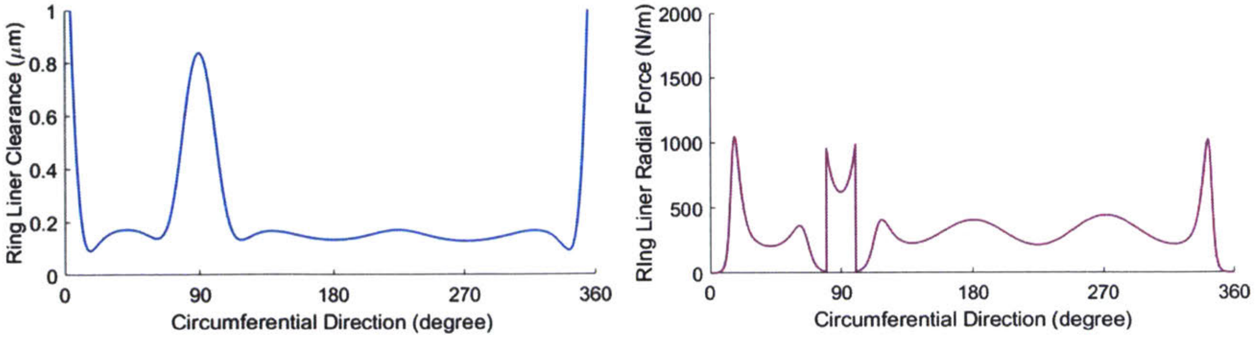

Figure 3.43 – Ring-liner clearance and liner force distributions for fully flooded boundary condition

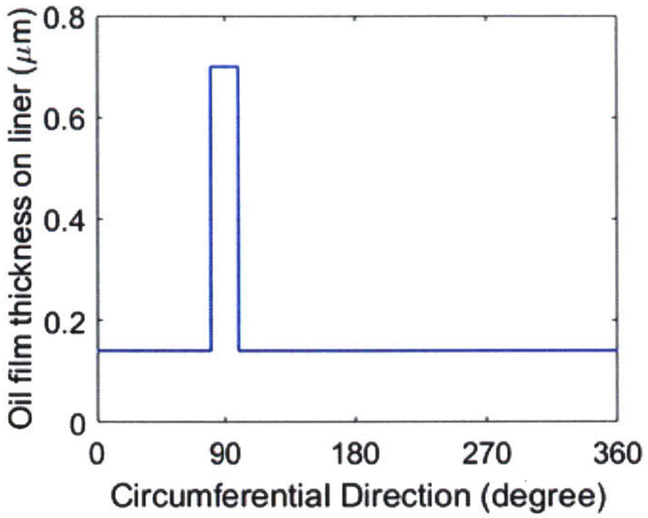

Figure 3.44 – Local oil accumulation on the liner for fully flooded case

Figures 3.45 and 3.46 shows the results obtained for the different oil film thicknesses at the peak. We distinguish three regions. The first one is for small peaks where $\frac{\Delta h}{\sigma_p} < 1$ where Δh is the oil film thickness difference between the peak and the rest of the oil film. In this region the resulting force distribution does not depend considerably on the oil film thickness difference. The effect of oil accumulation only emerges starting from $\frac{\Delta h}{\sigma_p} \geq 1$. We observe that the difference introduced for the liner force depends linearly on the oil film thickness difference provided $\frac{\Delta h}{\sigma_p}$ is not big enough. Beyond a certain value $\left(\frac{\Delta h}{\sigma_p}\right)_c$ we start losing the linear dependency. At the same time, beyond that same value we obtain force distributions those maximum exceed those obtained in the fully flooded case. Therefore we conclude that our tradeoff to distinguish the partially and fully flooded boundary conditions was over estimated. The more appropriate tradeoff should be $\frac{h_{max}-h_{\min}}{\sigma_p} \geq 3$ and since $h_{min} = 2\sigma_p$ we obtain $h_{max} \geq 5$ instead of the 10 chosen arbitrarily at the beginning. Beyond that critical value of $\frac{\Delta h}{\sigma_p}$ we reach the fully flooded boundary condition and the effect of the oil accumulation is independent of the oil film thickness as we can see in Figure 3.45 for $\frac{\Delta h}{\sigma_p} = 8$ and 10.

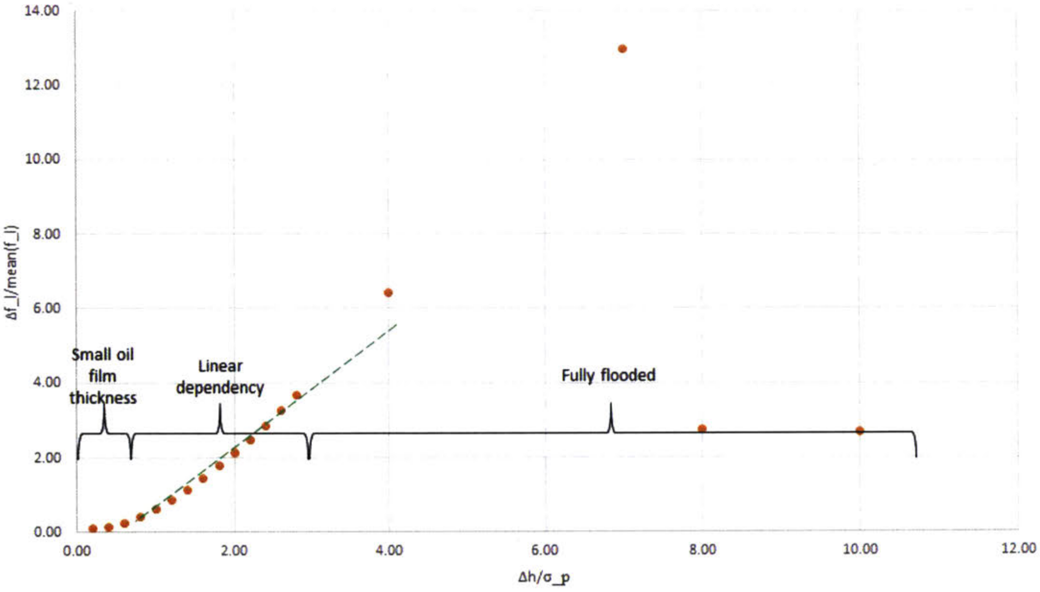

Figure 3.45 – Liner force difference with respect to the oil film thickness difference

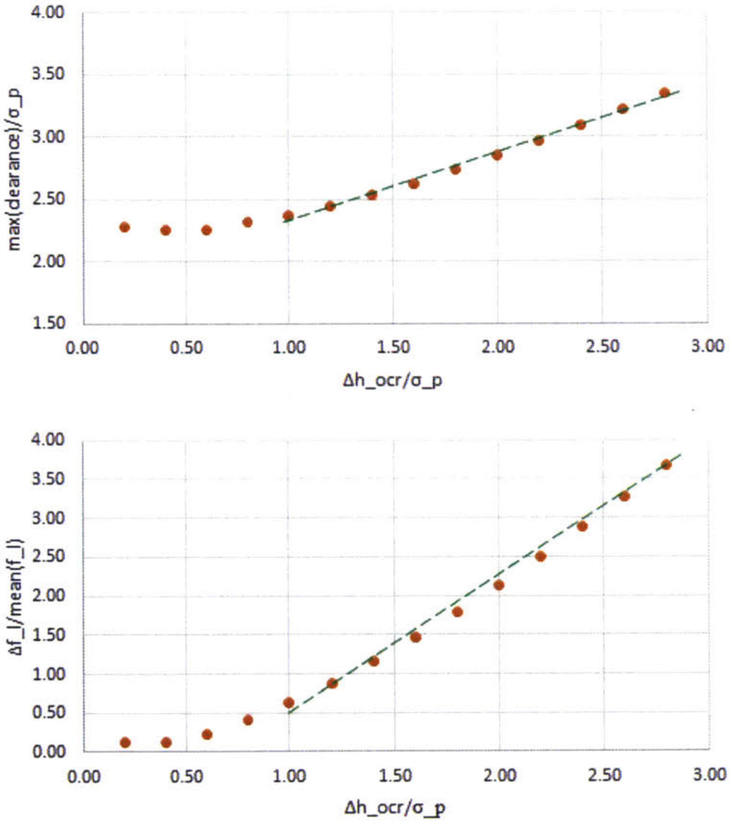

Figure 3.46 – Liner force difference and maximum ring-liner clearance with respect to the oil film thickness difference for partially flooded boundary condition at the oil peak

In the same manner as for the liner force difference, we also obtain a comparable behavior for the maximum ring-liner clearance at the oil peak location. For $\frac{\Delta h}{\sigma_p} < 1$, the resulting maximum clearance does not vary much with Δh. For $\frac{\Delta h}{\sigma_p} \geq 1$, we obtain again a linear dependence.

When characterizing the effect of oil accumulation we tried to use non-dimensional variables. The force difference one takes into account the ring tension. The maximum clearance and the oil film thickness difference consider the liner surface roughness standard deviation. The results obtained still depend on the ring stiffness (cross section and Young's modulus) as well as on its free shape. It is also affected by the bore diameter, its distortions and the gas pressure considered. Further analyses are needed if one wants to generalize the effect of these variables on the results that we obtained.

3.4.3.2. Local oil distribution on groove flanks

In section we look at the effect of having a variable oil film thickness on the lower groove flank. Given the pressure values which are coherent with those encountered in most of working engine conditions, the ring is well conform to the groove lower flank. Therefore we study the effect of introducing an oil distribution within the groove clearance with that flank. We run simulations for different oil distributions on the liner: uniform one with a thickness equal to $0.54\ \mu m$ and distributions as Gaussian functions with a plateau value equal to $0.54\ \mu m$ and a maximum value of $0.84\ \mu m$ at different locations of the ring. For each of these distributions of oil on the liner, we consider oil distributions on the groove flank as Gaussian functions with a plateau value equal to $0\ \mu m$ and a maximum value of $0.72\ \mu m$ and compare the results obtained with no oil on the groove flank. The maximum value of $0.72\ \mu m$ for the oil film thickness was chosen based on the minimum value of ring groove clearance obtained with no oil on the groove flank which is equal to $0.7\ \mu m$.

The oil distribution on the groove affected the ring neutral axis lift and the axial force. The ring radial coordinates and forces were not affected. Besides these modifications did not depend on the oil distribution on the liner. This is mainly due to the ring cross section geometry which is rectangular. Therefore we will present the results obtained for the uniform oil distribution on the liner and the conclusions drawn are still valid for the other oil distributions on the liner since in this section we would like to focus on the effect of variable oil distribution on the groove flanks.

Figure 3.47 gives the ring neutral axis lift for the three different locations of the oil peak: at 0°, 90° and 180° from the left to the right respectively. We see that the squeezing effect due to the pressure difference is more significant when the oil peak is not located at the gap since the oil peak magnitude considered is the same for the three different cases but the change in ring natural axis lift is more important when the peak is located at the gap. This is due to the free ring tip boundary condition which makes the ring less stiff at the gap than in other locations. The effect on the ring neutral axis once the oil peak is not located at the ring gap is the same wherever that peak is.

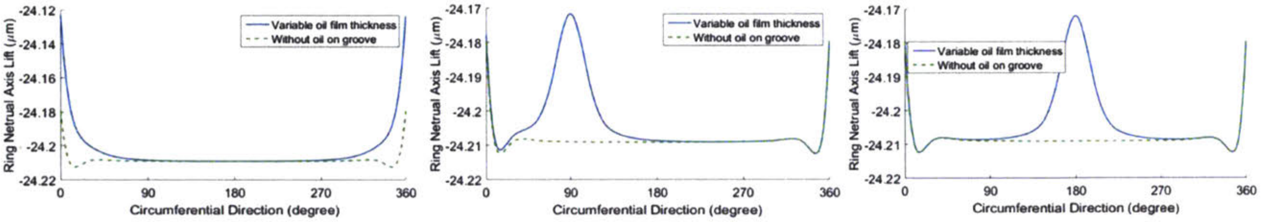

Figure 3.47 – Ring neutral axis lift for variable oil distributions on the groove flank with peaks at 0° (left), 90° (center) and 180° (right)

3.4.4. Ring-groove conformability

In this section we look at the effect of the gas pressure and friction forces to determine the ring groove conformability in terms of the axial location of the static position of the ring with respect to the groove flanks. In our simulations, we model the same diesel engine considered previously with a nominal bore radius equal to $95.25\,mm$. We use a ring with a rectangular cross section of dimensions $4mm\ x\ 2\ mm$ and a parabolic profile at the running face. The ring has a free shape designed to have uniform pressure distribution at a round shape with a ring tension of $25.4N$. The cylinder and ring are chosen in stainless steel. We consider no oil on the groove flanks and an incoming uniform oil film on the liner with a thickness equal to $2.5\sigma_p = 0.75\,\mu m$, where σ_p is the liner surface roughness standard deviation. The oil viscosity as a function of the liner temperature considered uniform and equal to $150^\circ\,C$ is given by our sponsor from Shell. Based on the notation used in Figure 3.3 we take $P_u = 96200\ Pa$, $P_i = 96200\ Pa$ and $P_d = 9500\ Pa$. We consider a circular bore with no distortions.

First of all, we consider a liner speed equal to $10\ ms^{-1}$ and directed downwards with a zero acceleration. In this case the gas pressure force is directed downward and the friction force from the liner is upward. For these numerical values we obtain a stable position where the ring is conform to the groove lower flank as presented in Figure 3.48 and 3.49. However when we increase the liner speed to a value of

$25\ ms^{-1}$ and always directed downwards with a zero acceleration and with the same pressure values, we obtain a stable position where the ring is conform to the groove upper flank as presented in Figure 3.50 and 3.51. In both cases the ring axial stable position is governed by the gas pressure and friction forces: in the first simulation the gas pressure one is dominant and in the second one it is the friction one that has a more significant effect.

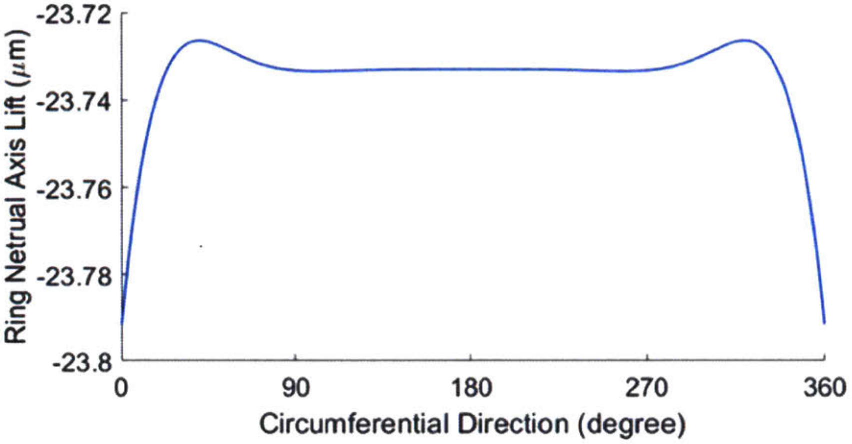

Figure 3.48 – Ring neutral axis lift for a 10 ms^{-1} downward liner speed

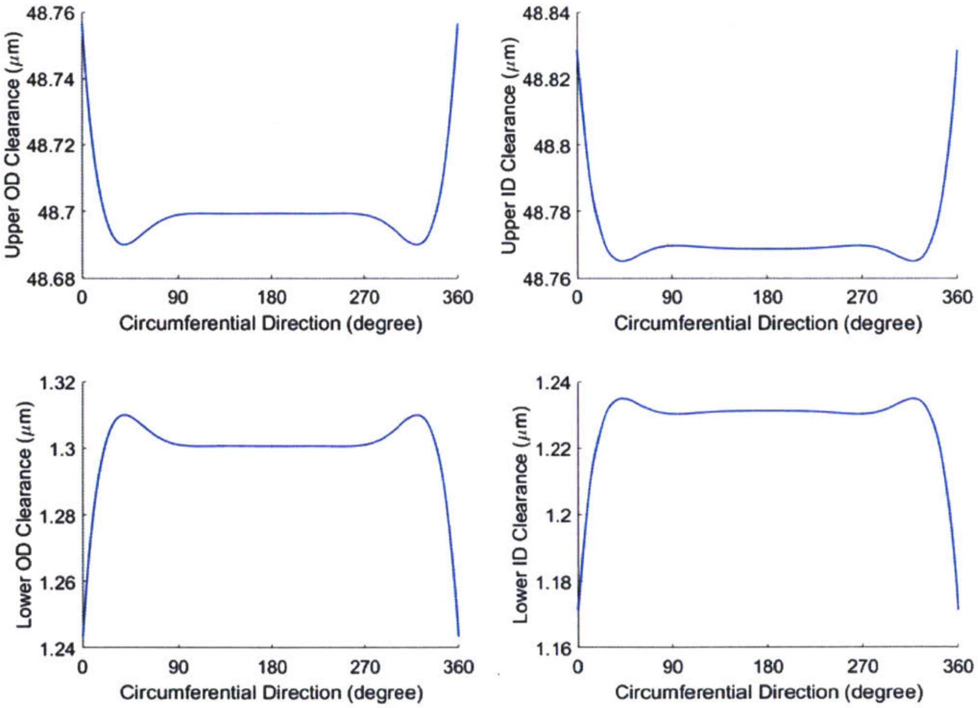

Figure 3.49 – Upper/lower ID/OC clearances for a 10 ms^{-1} downward liner speed

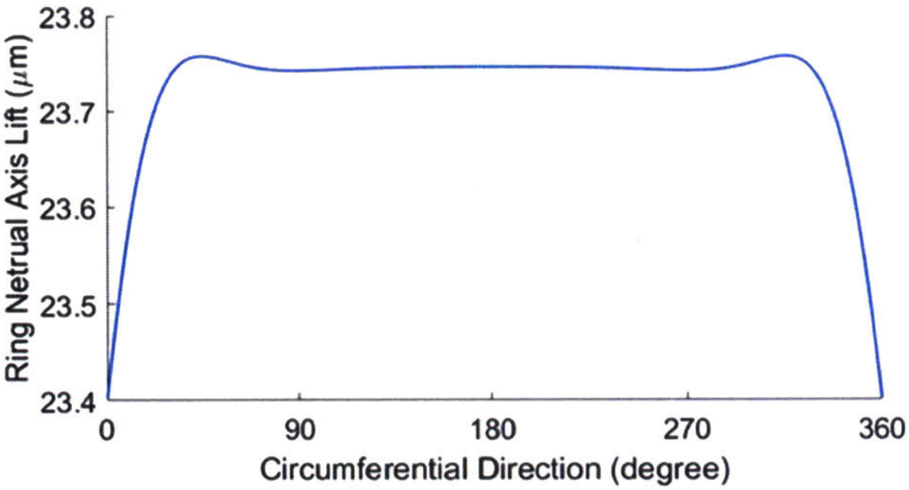

Figure 3.50 – Ring neutral axis lift for a 25 ms^{-1} downward liner speed

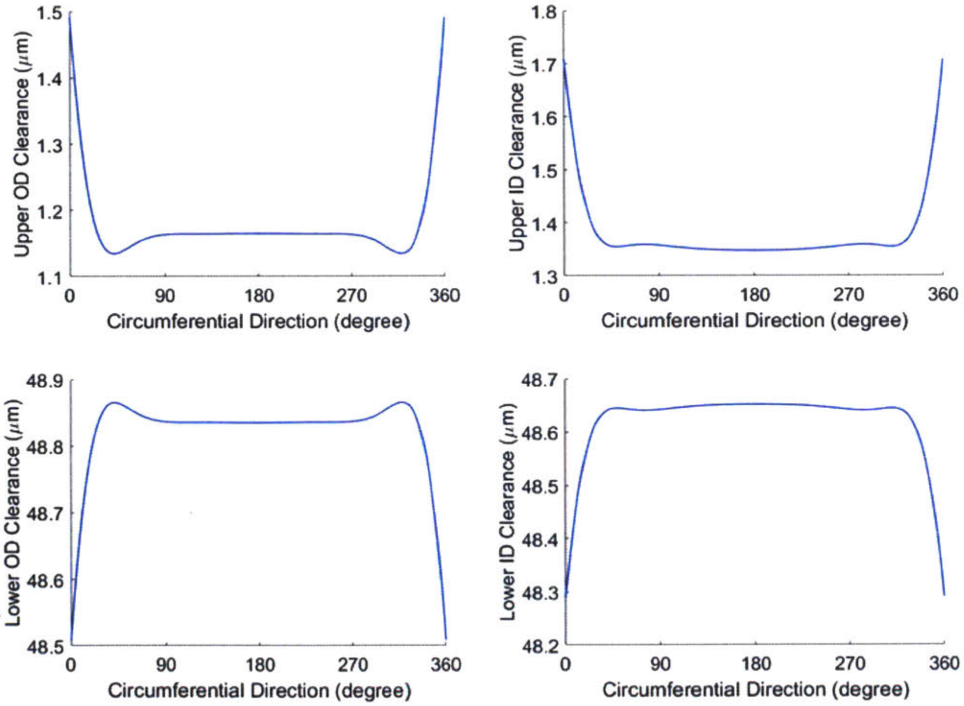

Figure 3.51 – Upper/lower ID/OC clearances for a 25 ms^{-1} downward liner speed

Considering the same ring and bore as in the previous simulation, we consider different gas pressure configurations using the dynamic model developed by Y. Liu [33] for the compression ring (top ring). We keep the same lubrication conditions. We look at the static state for different crank angles. In this case, besides the gas and friction force, we also consider the inertial one since the piston has a non-zero acceleration. The piston slides up and down in the cylinder. Its reciprocating motion is translated in rotation of the crank through the connecting rod as shown in Figure 3.52.

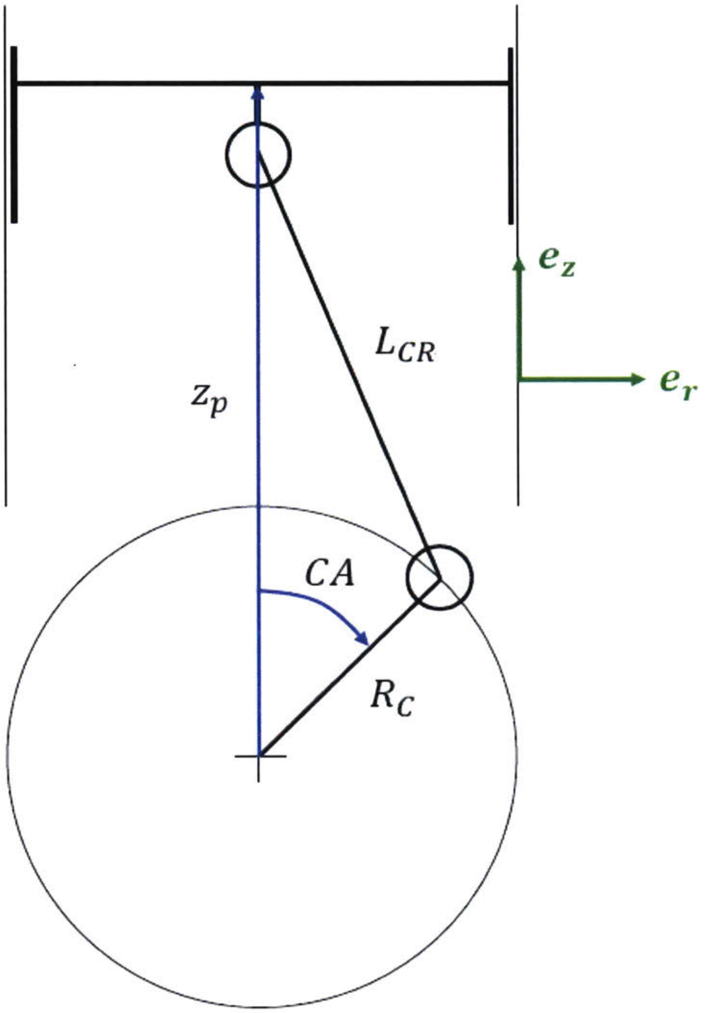

Figure 3.52 – Piston kinematics

z_p is the axial position of the piston, CA the crank angle, R_C the crank radius and L_{CR} the connecting rod length. Based on the geometry of the crank rod mechanism, the piston position can be expressed based on the crank angle as follows:

$$z_p = R_C \cos(CA) + \sqrt{(L_{CR}^2 - R_C^2 \sin^2(CA)}$$

(3.77)

The speed and acceleration of the piston in steady state operation can be computed by considering the first and second derivative with respect to time of equation (3.77) respectively. The angular velocity of the crank is given by equation (3.78). We can relate it to the engine speed expressed in rotation of the crank per minute RPM as shown in equation (3.79).

$$\omega = \frac{dCA}{dt}$$

(3.78)

$$\omega = \frac{2\pi RPM}{60}$$

(3.79)

The expressions of the piston velocity and acceleration are given by equations (3.80) and (3.81) respectively.

$$V_p = \omega\left(-R_C\sin(CA) - \frac{R_C^2\sin(CA)\cos(CA)}{\sqrt{L_{CR}^2 - R_C^2\sin^2(CA)}}\right)$$

(3.80)

$$A_p = \omega^2\left(-R_C\cos(CA) - \frac{R_C^2[\cos^2(CA)-\sin^2(CA)]}{\sqrt{L_{CR}^2-R_C^2\sin^2(CA)}} - \frac{R_C^4\cos^2(CA)\sin^2(CA)}{\left(\sqrt{L_{CR}^2-R_C^2\sin^2(CA)}\right)^3}\right)$$

(3.81)

For our simulations we choose a crank radius equal to $R_C = 40\ mm$ and a connecting rod length $L_{CR} = 140\ mm$. The results are for an $2000\ RPM$.

In the common engine working conditions, the upper region gas pressure P_u as defined in Figure 3.3. is always higher than the lower region one P_d. This is confirmed for all the crank angles by the simulation results obtained from the dynamic model. Therefore the gas pressure force is always directed downwards pushing the ring towards the groove lower flank. Figure 3.53 shows the piston velocity and acceleration variation with respect to the crank angle over one engine revolution. An engine cycle corresponds to two engine revolutions. We can see that for a crank angle between 0° and around 80° (and thus between 360° and around 440°), the inertial and friction force are directed upwards, both opposite to the gas pressure force. Therefore in this region the ring can lose its conformability with the groove lower flank. In our study we look at the smallest value of P_d, noted $(P_d)_c$, that makes this happen. We consider that the ring loses its conformability with the minimum of the ring-groove lower flank clearance is equalt to $5\sigma_p = 1.5\ \mu m$. For a crank angle between around 80° and 180° (and thus between around 440° and 540°), the inertial force is directed downwards and the friction upwards. Given the parameters of our simulation, and mainly the oil properties, its film thickness and the engine architecture, even for the first crank angle (as integer) that gives the smallest non-zero acceleration and almost the highest value of the piston velocity and with $P_d = (P_d)_{max} = P_u$ the static case of the ring gives a conformability with the lower groove flank. Therefore, for this range of crank angles, the ring cannot lose its static conformability with the lower groove flank. For a crank angle between 180° and around 280° (and thus between 540° and around 640°), both friction and inertia are directed downwards and thus the ring will conform to the groove lower flank. Finally for a crank angle between around 280° and 360° (and thus between around 640° and 720°), the inertial force is directed upwards and the friction downward. As stated previously, given the parameters of our simulation the inertia effect is more significant than the friction one and thus for this range of crank angles we can look at the smallest value of P_d that makes the ring lose its conformability.

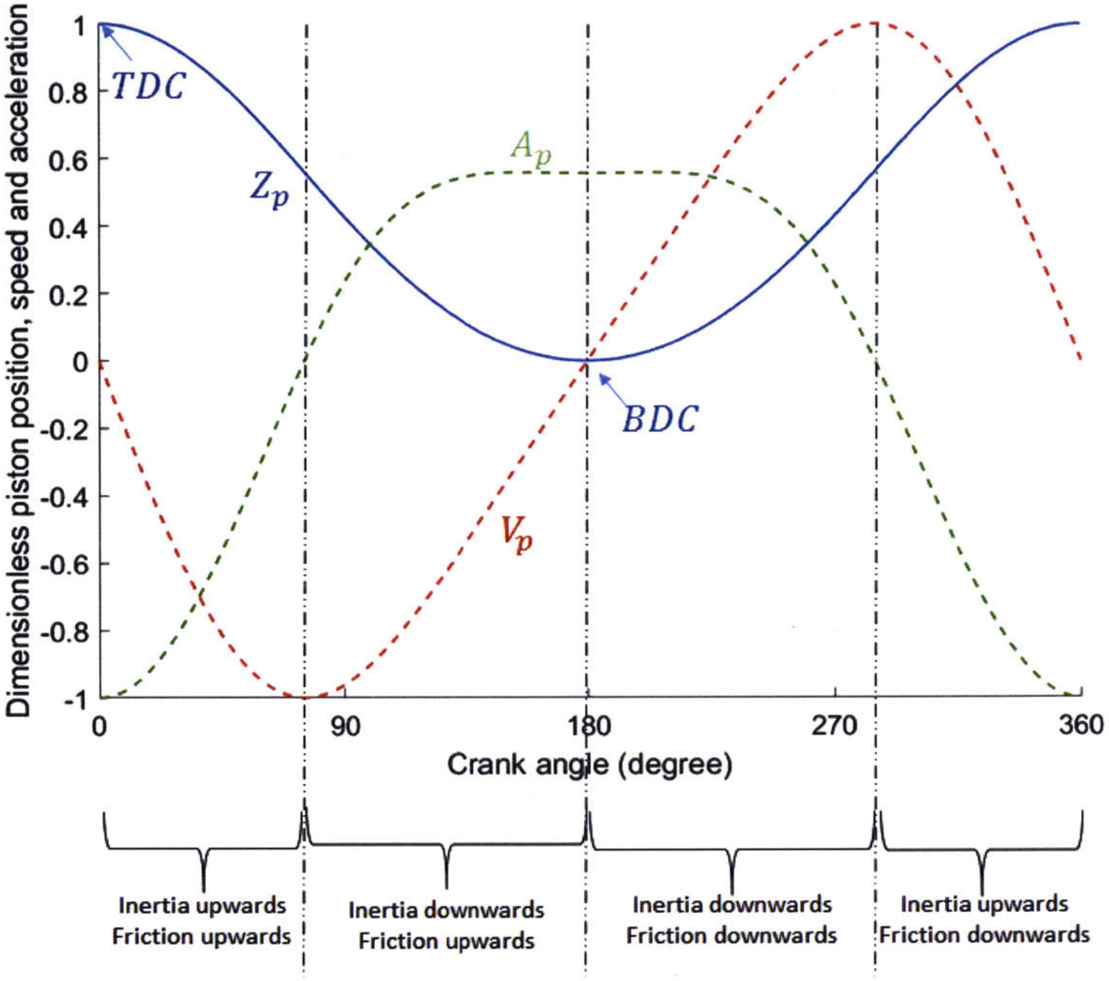

Figure 3.53 – Piston position, speed and acceleration over one engine revolution

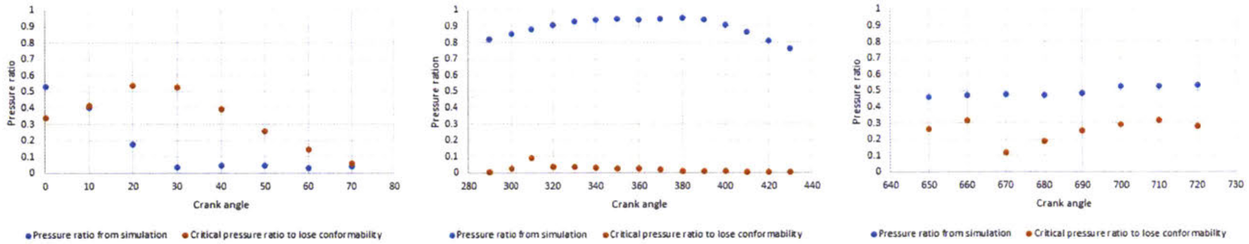

Figure 3.54 – Pressure ratios for different crank angle

In Figure 3.54, we plot the two ratios $\frac{P_u-P_d}{P_u}$ with blue points and $\frac{P_u-(P_d)_c}{P_u}$ with orange points, where P_u and P_d are the upper groove region and lower groove region gas pressures respectively obtained from the dynamic simulation, and $(P_d)_c$ is the critical lower groove region gas pressure that makes the ring lose its conformability with the lower flank for different crank angles within the intervals where this phenomenon can happen as explained above. The critical lower groove region gas pressure represent the pressure above which the ring will have a minimum clearance with the groove lower flank that is higher than the threshold that we fixed $(3\sigma_p)$. This gives us an idea about the regions where the ring is susceptible to lose its conformability with the groove lower flank in the engine working conditions simulated here. We see that among all the crank angles considered, only the interval $[10°; 70°]$ contains a lower region pressure that is higher than the critical value and thus the ring is likely to lose its conformability. This corresponds to the first half of the intake stoke where the gas pressure is getting more and more homogenous around the ring making P_u and P_d close enough while both the inertia and friction forces are directed upwards which explains the results obtained for that region. However for the interval $[360°; 430°]$ that contains the second part of the engine cycle where the inertia and friction force are upwards, we see that the rings does not lose its conformability. Indeed, this corresponds to the first half of the expansion (or combustion) stroke. Therefore the pressure difference $P_u - P_d$ is high since the gas pressure needs a longer period of time to get homogenous compared to the intake stroke and thus, even with a friction and inertia forces directed upward, the pressure difference is high enough to maintain the ring-lower groove conformability. This is confirmed by the ratio $\frac{P_u-P_d}{P_u}$ close to 1 that we obtained for that region. Besides, the critical pressure $(P_d)_c$ is determined mainly by the difference $P_u - (P_d)_c$ that gives a global axial force directed upwards. Therefore this difference is the same for the crank angles within the interval $[0°; 70°]$ and $[360°; 430°]$ but since P_u is bigger in the second one and since Figure 3.54 shows the ratio $\frac{P_u-(P_d)_c}{P_u}$, this quantity is smaller for crank angles within the interval $[360°; 430°]$ (does not exceed 0.1 in the plot given in the middle) than within the first one (almost always bigger than 0.1 except for 70° in the plot given on the right). This same analysis is valid when we compare the results obtained for the intervals $[280°; 360°]$ (analogous to the interval $[360°; 430°]$) and $[640°; 720°]$ (analogous to the interval $[0°; 70°]$). For the interval $[280°; 360°]$ during the second half of the compression stroke, the gas pressure is getting higher in the groove upper region faster than the increase of the gas pressure in the lower one, therefore the ring does not lose its conformability with the groove lower flank. Besides this explains the small values obtained for the ratio $\frac{P_u-(P_d)_c}{P_u}$ as for the interval $[360°; 430°]$. Concerning crank angles within $[280°; 360°]$ during the second half of the exhaust stroke, only inertia is directed upwards and the gas pressure is getting more homogenous making $\frac{P_u-P_d}{P_u}$ smaller and $\frac{P_u-(P_d)_c}{P_u}$ higher but not enough to make the ring lose its conformability with the groove lower flank. This trend is kept till we reach the intake stroke (note the same ratios obtained for crank angles equal to

0° and 360°) during which both inertia and friction are directed upwards with a more homogenous gas pressure, making the ring more likely to lose its conformability with the groove lower flank as explained above. This analysis gives an idea about the gas pressure that needs to be maintained in the lower groove region during the engine cycle so that the ring does not lose its conformability and oil does not move around the ring to the groove inner region which promotes its flow to the crown land (or 2nd land if we considered the second ring) and thus is very likely to contribute to oil consumption.

3.5. Conclusion

In this chapter, the ring statics model based on the curved beam finite element method developed in the previous section was used along with ring-liner contact, ring-groove contact and thermal moment models. This is a comprehensive tool to analyze ring structural response and to study ring-liner and ring-groove conformability. Based on the boundary conditions, this tool is also able to help understand some local processes and its effect on the ring-liner and ring-groove interaction.

The results obtained prove that the curved beam finite element method is able to give a reasonable prediction of ring structural response. The thermal moment model that we used is more general than L. Liu [30] solution in the sense that it takes into account the thermal bending moment all along the ring and not only at the tips which can be significant when we have high bore distortions and thus large ring-liner clearance at points far from the tips. The gap location of the ring within the distorted bore also affects its conformability leading to significant difference for the ring-liner clearances. Hence this structural response affects the oil consumption and sealing performances. Furthermore this tool is able to determine the threshold between the different lubrication boundary conditions and the ring conformability and its interaction with the liner when it encounters some local oil accumulation or when bridging happens. In a more general sense, this curved beam finite element method links the global and local behaviors and the interaction between them. The trend of the ring-liner and ring-groove contact behavior is mainly determined by the global structural response while the local process makes a difference to the oil supply and contact behavior locally. As shown in the experiments [42] [43], oil film thickness on the liner varies along the circumferential direction and local oil accumulation is observed. As a result, both of them need to be included to study ring-liner interaction. We also gives a study of the ring-groove conformability that is determined by the gas pressure, the friction and the inertial forces. The results show that the ring is susceptible to lose its conformability with the groove lower flank during the first half of the intake stroke. The study also shows the condition that can be imposed on the pressure within the groove lower region for each crank angle so that the ring conforms well to the groove. Otherwise oil is very likely to flow around the ring to the groove inner region and then to piston upper parts and hence increase its consumption. Besides this will hamper the sealing performance of the ring pack system.

4. Static twist under fixed ID/OD constraint

To control gas or oil transport more effectively, top two rings are often designed to have static twist angles after being inserted into the piston and cylinder. This is accomplished by making the ring cross-section asymmetric. The static twist is used in the 2D ring dynamics model [40] that assumes the static twist value is obtained under no external moment. In practice, the static twist is measured by minimizing the external moment as described later. To calculate the static twist, we adapt Liu's method [25] that applies constraints that level the axial position of ring ID or OD depending on the direction of the static twist.

To model the static twist under fixed ID/OD constraint, we use the closing ring method, modify the curved beam finite element model introduced in chapter 2 and consider the appropriate external loads. We also compare the results obtained by our model with the existing straight beam based ring design tool developed by L. Liu.

4.1. Experiments description

To determine the static twist under fixed ID/OD constraint, the ring is first closed such that it has a zero gap. Then, it is introduced within a circular band on a flat plate and the user taps gradually on the ring till it reaches a stable static position. The tapping along the circumferential direction is carried out so that the ring reaches the minimum clearance with the lower plate but without generation of any contact force between them.

Ideally the band would be perfectly circular and the ring gap is zero. However, these two conditions could not be satisfied and our model is able to consider these conditions by introducing band distortion and a non-gap. Besides, the tapping process is never carried out such that there is no contact force between the ring and the lower plate. In Section 4.4, we will consider these non-ideal cases where the clearance is lower than the one giving a zero force contact when we compare our results with those given by the straight beam based ring design tool.

4.2. Ring symmetry

As introduced in chapter 2, ring cross section can be asymmetric as presented in figure 4.1. In that case the principal frame does not align with the natural one creating a non-zero principal angle. When closing the ring to a circular shape and maintaining it in that configuration, we are actually applying a radial load on the outer diameter surface of the ring. Because of the mass distribution within the asymmetric cross section, this radial load create a local twist moment. Since we are dealing with continuum solid body, the twist of each cross section will create an internal stress with the adjacent cross section and make it twist in the same direction. Thus by moving from each of the ring tips toward the ring back (the opposite point to the tips), we have an increasing total twist moment at each cross section resulting from the internal stress effect plus the radial load applied. This results in an increasing absolute value of the static twist angle which reaches it maximum at the ring back. This explains the numerical and experimental results that we observe for the static twist under fixed ID/OD constraint.

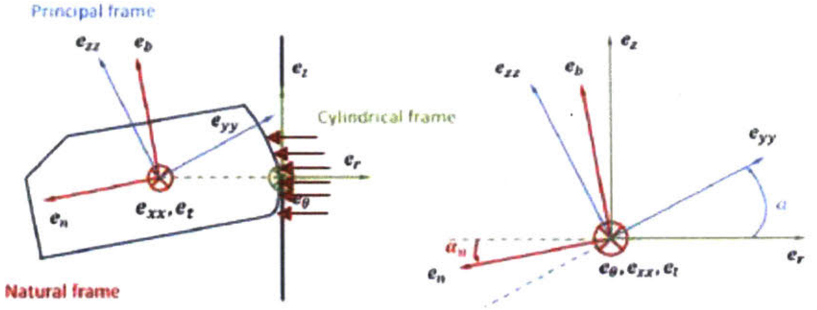

Figure 4.1 – Ring principle frame, Natural frame and Cylindrical frame

The sign of the static twist depends on the ring cross section and mass distribution. Two types of second rings are shown in Figure 4.2. The left one is called the scraper ring and the right one the Napier ring. For the second ring, static twist is generally introduced by cutting off the ring material at the one of the internal diameter corners. If the ring has a negative principal angle, its static twist will also be negative. In that case we have a fix OD constraint. This is the case when the lower internal diameter corner is cut-off. If the ring has a positive principal angle, its static twist will also be positive. In that case we have a fix ID constraint. This is the case when the upper internal diameter corner is cut-off.

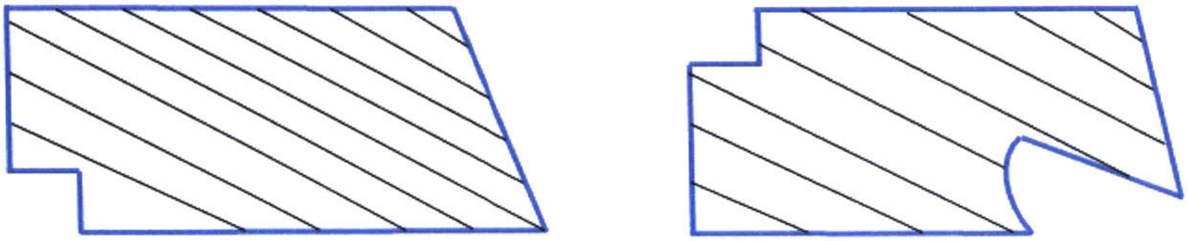

Figure 4.2 – Second ring designs

4.3. Adaptation of curved beam finite element model

In order to adapt the curved beam finite element model for the static twist problem, we keep the modeling of the ring within the piston and cylinder but only consider dry contact forces introduced in section 3.1.1 for the ring-liner contact which models the ring-band contact and in section 3.2.2 for the ring-groove contact which models the ring-lower plate contact. The ring-upper flank groove contact force will always be zero since we impose the fix ID/OD constraint which makes the ring in contact with the lower flank groove and adopt a groove clearance bigger than the ring's diagonals which ensures that there is no force generation with the upper groove flank whatever the static twist angle is.

If the ring has a positive principal angle, we apply a fix ID constraint. This means that the lower internal corner will have the smallest possible clearance with the lower plate, modeled as the groove lower flank, but without the generation of any force contact. Based on the simplified formulation of the greenwood and Tripp pressure contact formula (3.6) this means that the clearance should be equal to $\Omega\sigma_p$ where $\sigma_p = 0.4\ \mu m$ the standard deviation of the lower plate roughness and Ω is the threshold that determines the clearance under which the asperity contact is generated. A typical value for this threshold is 4. If the ring has a negative principal angle, then we apply a fix OD constraint and it is the lower external corner that will have the smallest possible clearance with the lower plate without the generation of any force contact.

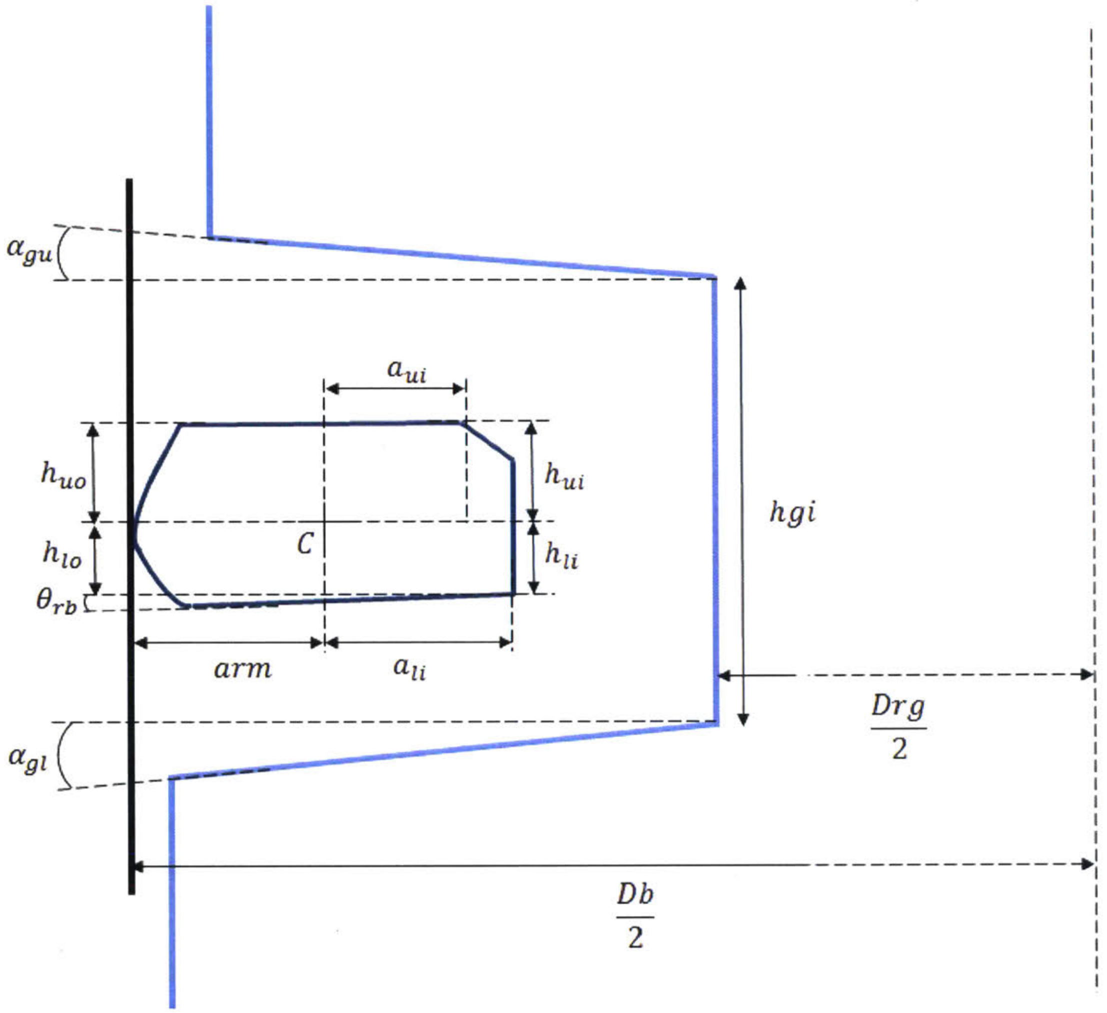

Figure 4.3 – Groove and ring-cross section dimensions

Figure 4.3 shows the groove and ring-cross section dimensions that will be used to determine the constraint equations to model the fix ID/Od conditions. These equations will be solved along with Euler-Lagrange equations introduced in section 2.3. Db and Drg are respectively the bore and groove root diameter. hgi is the groove inner axial height.

If the radial axis is noted as the y axis and the axial one as the z axis, the principal angle is given by the following equation

$$\alpha_p = \frac{\operatorname{atan}\left(\frac{2I_{yz}}{I_{yr} - I_{zr}}\right)}{2}$$

(4.1)

Where I_{yr} and I_{zr} are respectively the moments of inertia out of and in plane and I_{yz} is the product of inertia. Their definitions are given below.

$$I_{yr} = \int_A z^2 dA$$

(4.2)

$$I_{zr} = \int_A y^2 dA$$

(4.3)

$$I_{yz} = \int_A yzdA$$

(4.4)

The fix ID or fix OD constraint is solely determined by the ring cross section based on the principal angle sign. If that angle is positive then we have a fix ID constraint and the corresponding equation is the following one:

$$\frac{gcl}{2} + z - ali\ \alpha_r = \Omega\sigma_p$$

(4.5)

$\frac{gcl}{2}$ is the ring groove clearance at the centroid location when the groove is located at the midpoint of the groove axial clearance. The axial displacement z is defined appropriately to this choice. Therefore gcl is given by the following equation:

$$gcl = hgi + \left(\frac{Db}{2} - \frac{Drg}{2} - arm\right)\left(\alpha_{gu} + \alpha_{gl}\right) - \left(hui + \theta_{rt}aui + hli + \theta_{rb}ali\right)$$

(4.6)

If the ring principal angle is negative then we have a fix OD constraint and the corresponding equation is the following one:

$$\frac{gcl}{2} + z + alo\ \alpha_r = \Omega\sigma_p$$

(4.7)

The tapping force is modeled as an unknown. In order to keep the same smoothness as the other variables, we interpolate it using 5th order Hermite polynomial spline. Therefore we add three additional unknowns per node. In order to have a close system, we need to have three equations apart from the Euler-Lagrange ones. Hence, as we do for the axial and radial displacement, we interpolate the angles using the 5th order Hermite polynomial spline so that the constraint (4.5) or (4.7) gives three additional equations involving z and α, their first derivatives and the second ones. Hence we give up the 3rd order interpolation adopted in section 2 modeling for the angles.

Using the isoparametric variable η define in (2.18) and the shape functions $(N_k)_{k=1}^{k=6}$ defined in (2.22)-(2.27), the fifth order interpolations for an element give:

$$y(\eta) = \sum_{k=1}^{6} N_k(\eta) u_{yk} \text{ where } \{u_y\} = \{u_{y1} \dots u_{y6}\}^T = \{y_1, y_1', y_1'', y_2, y_2', y_2''\}^T$$

(4.8)

$$z(\eta) = \sum_{k=1}^{6} N_k(\eta) u_{zk} \text{ where } \{u_z\} = \{u_{z1} \dots u_{z6}\}^T = \{z_1, z_1', z_1'', z_2, z_2', z_2''\}^T$$

(4.9)

$$\alpha_r(\eta) = \sum_{k=1}^{6} N_k(\eta) u_{\alpha k} \text{ where } \{u_\alpha\} = \{u_{\alpha 1} \dots u_{\alpha 6}\}^T = \{\alpha_1, \alpha_1', \alpha_1'', \alpha_2, \alpha_2', \alpha_2''\}^T$$

(4.10)

$$f(\eta) = \sum_{k=1}^{6} N_k(\eta) u_{fk} \text{ where } \{u_f\} = \{u_{f1} \dots u_{f6}\}^T = \{f_1, f_1', f_1'', f_2, f_2', f_2''\}^T$$

(4.11)

Each ring element has two nodes and therefore 24 nodal variables, 12 degree of freedoms per node. The variable vector for an element is rewritten below.

$$u^{(e)} = \{u_1, \dots, u_{24}\} = \{y_1, y_1', y_1'', z_1, z_1', z_1'', \alpha_1, \alpha_1', \alpha_1'', f_1, f_1', f_1'', y_2, y_2', y_2'', z_2, z_2', z_2'', \alpha_2, \alpha_2', f_2, f_2', f_2''\}$$

(4.12)

To select the appropriate shape function corresponding to the kth nodal displacement within a ring element, we use the mapping function given below.

$$k_y = [1,2,3,13,14,15]$$

(4.13)

$$k_z = [4,5,6,16,17,18]$$

(4.14)

$$k_\alpha = [7,8,9,19,20,21]$$

(4.15)

$$k_f = [10,11,12,22,23,24]$$

(4.16)

$$k \longmapsto m(k)$$

$$[1,2,3,4,5,6,7,8,9,10,11,12,13,14,15,16,17,18,19,20,21,22,23,24]$$

$$\longmapsto [1,2,3,1,2,3,1,2,3,1,2,3,4,5,6,4,5,6,4,5,6,4,5,6]$$

(4.17)

Using this mapping function, (4.8), (4.9), (4.10) and (4.11) can be rewritten in a more compact form as follows.

$$y(\eta) = \sum_{k_y} N_{m(k_y)}(\eta) u_{k_y}$$

(4.18)

$$z(\eta) = \sum_{k_z} N_{m(k_z)}(\eta) u_{k_z}$$

(4.19)

$$\alpha_r(\eta) = \sum_{k_\alpha} N_{m(k_\alpha)}(\eta) u_{k_\alpha}$$

(4.20)

$$f(\eta) = \sum_{k_f} N_{m(k_f)}(\eta) u_{k_f}$$

(4.21)

By modeling the closing ring process as we carried it out in section 2.4, the Euler-Lagrange equations become:

$$\frac{\partial U^{(e)}}{\partial u_{di}} = \frac{\partial W^{(e)}}{\partial u_{di}} - F_{initial,di} \text{ for } i = \{1 \dots n\}$$

(4.22)

$$W^{(e)} = \int_0^{L_e} (f_r y + f_z z + f z + m_t \alpha) ds$$

(4.23)

$$U^{(e)} = U_{zz}^{(e)} + U_{yy}^{(e)} + U_{\theta}^{(e)}$$

(4.24)

$$U_{yy}^{(e)} = \frac{1}{2}\int_0^{L_e} EI_{yy}(\kappa_{zz} - \kappa_{zz0})^2 ds = \frac{L_e EI_{yy}}{2}\int_0^1 \left(\left(\frac{1}{R} - \frac{y + y''}{R^2}\right)\sin\left(\alpha + \frac{z''}{R}\right) - \kappa_{fs}\sin(\alpha_p)\right)^2 d\eta$$

(4.25)

$$U_{\theta}^{(e)} = \frac{1}{2}\int_0^{L_e} GJ_t\left(\tau + \frac{d}{ds}(\alpha_n - \alpha)\right)^2 ds = \frac{L_e GJ_t}{2}\int_0^1 \left(\frac{z' - R\alpha'}{R^2}\right)^2 d\eta$$

(4.26)

$$U_{zz}^{(e)} = \frac{1}{2}\int_0^{L_e} EI_{zz}(\kappa_{yy} - \kappa_{yy0})^2 ds = \frac{L_e EI_{zz}}{2}\int_0^1 \left(\left(\frac{1}{R} - \frac{y + y''}{R^2}\right)\cos\left(\alpha + \frac{z''}{R}\right) - \kappa_{fs}\cos(\alpha_p)\right)^2 d\eta$$

(4.27)

$$F_{initial,di}^{(e)} = \frac{\partial U^{(e)}}{\partial u_{di}}\Big|_{\substack{y=0,y'=0,y''=0 \\ z=0,z'=0,z''=0 \\ \alpha=\alpha_p,\alpha'=0}}$$

(4.28)

The axial force f_z in (4.23) includes only the ring-band and ring-lower plate dry contact forces .The variable u_{di} represents the dith displacement degree of freedom of the system composed by the two nodes of the ring element and when assembled in one vector, form the displacements and their derivatives at those nodes (4.29). Thus $di \in k_y \cup k_z \cup k_\alpha$. Subscripts 1 and 2 refer to the first and second node of the element respectively.

$$u_d^{(e)} = \{u_{d1}, \dots, u_{d16}\} = \{y_1, y_1', y_1'', z_1, z_1', z_1'', \alpha_1, \alpha_1', y_2, y_2', y_2'', z_2, z_2', z_2'', \alpha_2, \alpha_2'\}$$

(4.29)

These equations along with the constraint one (4.5) or (4.7) and their first and second derivatives gives a close system of 24 unknowns and 24 equations per element.

$$z' - ali\ \alpha' = 0$$

(4.30)

$$z'' - ali\ \alpha'' = 0$$

(4.31)

$$z' + alo\ \alpha' = 0$$

(4.32)

$$z'' - alo\ \alpha'' = 0$$

(4.33)

In analogy with section 2.5, we develop the stiffness matrix, load vector and initial force. The load vector in this case does not only include external forces components but also the constant term in the constrain equations 94.5) or (4.7).

$$alg = ali * (\alpha_p \geq 0) - alo * (\alpha_p < 0)$$

(4.34)

$$K_{ij}^{(e)} = \begin{cases} \frac{L_e E I_{zz}}{R^4} \int_0^1 \left(N_{m(i)} + N''_{m(i)}\right)\left(N_{m(j)} + N''_{m(j)}\right) d\eta & for\ \{i,j\} \in k_y \\ \frac{L_e}{R^2} \int_0^1 \left(E I_{yy} N_{\alpha m(i)} N_{\alpha m(j)} + G J_t N'_{\alpha m(i)} N'_{\alpha m(j)}\right) d\eta & for\ \{i,j\} \in k_\alpha \\ \frac{L_e}{R^4} \int_0^1 \left(E I_{yy} N''_{m(i)} N''_{m(j)} + G J_t N'_{m(i)} N'_{m(j)}\right) d\eta & for\ \{i,j\} \in k_z \\ \frac{L_e}{R^3} \int_0^1 \left(E I_{yy} N''_{m(i)} N_{\alpha m(j)} - G J_t N'_{m(i)} N'_{m(j)}\right) d\eta & for\ (i,j) \in k_z \times k_\alpha\ or\ (i,j) \in k_\alpha \times k_z \\ -L_e \int_0^{L_e} N_{m(i)} N_{m(j)} ds & for\ (i,j) \in k_z \times k_f \\ \frac{L_e}{R^3} \int_0^1 \left(E I_{yy} N''_{m(i)} N_{\alpha m(j)} - G J_t N'_{m(i)} N'_{m(j)}\right) d\eta & for\ (i,j) \in k_z \times k_\alpha\ or\ (i,j) \in k_\alpha \times k_z \\ 1 & for\ (i,j) \in k_f \times k_z \\ -alg & for\ (i,j) \in k_f \times k_\alpha \\ 0 & otherwise \end{cases}$$

(4.35)

$$F_{ext,i}^{(e)} = \begin{cases} \int_0^{L_e} f_r N_{m(i)} ds & for\ i \in k_y \\ \int_0^{L_e} f_z N_{m(i)} ds & for\ i \in k_z \\ \int_0^{L_e} m_t N_{\alpha m(i)} ds & for\ i \in k_\alpha \\ \Omega \sigma_p - \frac{gcl}{2} & for\ i \in k_f \end{cases}$$

(4.36)

$$F_{initial,i}^{(e)} = \begin{cases} -L_e E I_{zz} \int_0^1 \left(\frac{1}{R} - \kappa_{fs}\right) \frac{\cos^2(\alpha_p)}{R^2} \left(N_{m(i)} + N''_{m(i)}\right) d\eta & \\ -L_e E I_{yy} \int_0^1 \left(\frac{1}{R} - \kappa_{fs}\right) \frac{\sin^2(\alpha_p)}{R^2} \left(N_{m(i)} + N''_{m(i)}\right) d\eta & for\ i \in k_y \\ -L_e E I_{zz} \int_0^1 \left(\frac{1}{R} - \kappa_{fs}\right) \frac{cos(\alpha_p) \sin(\alpha_p)}{R^2} N''_{m(i)} d\eta & \\ +L_e E I_{yy} \int_0^1 \left(\frac{1}{R} - \kappa_{fs}\right) \frac{sin(\alpha_p) \cos(\alpha_p)}{R^2} N''_{m(i)} d\eta & for\ i \in k_z \\ -L_e E I_{zz} \int_0^1 \left(\frac{1}{R} - \kappa_{fs}\right) \frac{cos(\alpha_p) \sin(\alpha_p)}{R^2} N'_{m(i)} d\eta & \\ +L_e E I_{yy} \int_0^1 \left(\frac{1}{R} - \kappa_{fs}\right) \frac{sin(\alpha_p) \cos(\alpha_p)}{R^2} N'_{m(i)} d\eta & for\ i \in k_\alpha \\ 0 & for\ i \in k_f \end{cases}$$

(4.37)

The finite element equation to solve (4.38) is given by:

$$[K]^{(e)}\{u\}^{(e)} = \{F_{ext}\}^{(e)} - \{F_{initial}\}^{(e)}$$

(4.38)

The assembly of the finite element matrices is carried out as explained is section 2.6 to end up with global matrices and unknown vector $\{u\}$ (4.40) as the assembly of the different nodal unknown vectors. n is the total number of nodes for the whole ring.

$$[K]\{u\} = \{F_{ext}\} - \{F_{intiial}\}$$

(4.39)

$$\{u\} = \left\{u_1^{(1)}, \dots, u_{12}^{(1)}, u_1^{(2)}, \dots, u_{12}^{(2)}, \dots, u_1^{(n-1)}, \dots, u_{12}^{(n-1)}, u_1^{(n)}, \dots, u_{12}^{(n)}\right\}^T$$

(4.40)

The tapping force is assumed to be applied on the cross section centroid without any offset which explains the expression adopted for the external work (4.23) where the tapping force do not contribute to the twist moment term. This is an ideal case but at least minimizes the external twist moment and gives stable results for the two different cases regarding the principal angle sign. In fact, when modelling the tapping force as being applied on the ring external upper corner, it gives oscillatory static twist for positive principle angle rings as shown in Figure 4.4. and when applied on the ring internal upper corner, it gives oscillatory static twist for negative principle rings as presented in Figure 4.5. Indeed for these cases, the tapping force is introducing a static moment in the opposite direction to the moment introduced by the radial force which by itself defines a stable static position for the ring angular displacement. Thus the extra moment introduced by the tapping force is altering that equilibrium which makes the static twist oscillate in order to balance the different moment components.

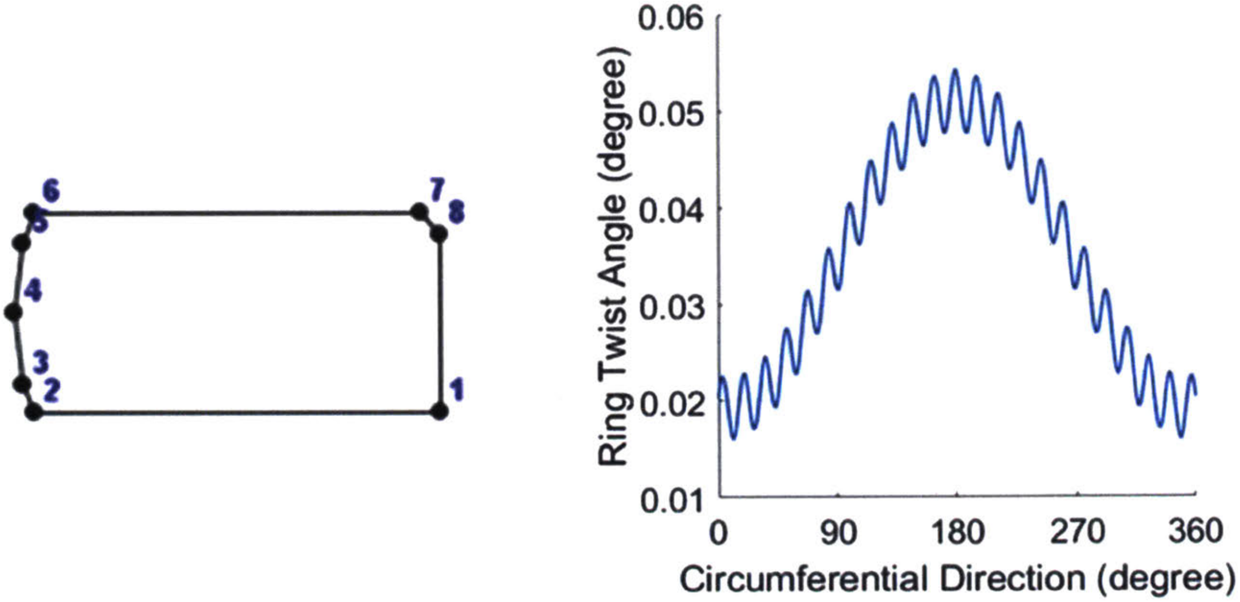

Figure 4.4 – Ring cross section with positive principal angle and the corresponding twist angle - tapping force as being applied on the ring external upper corner

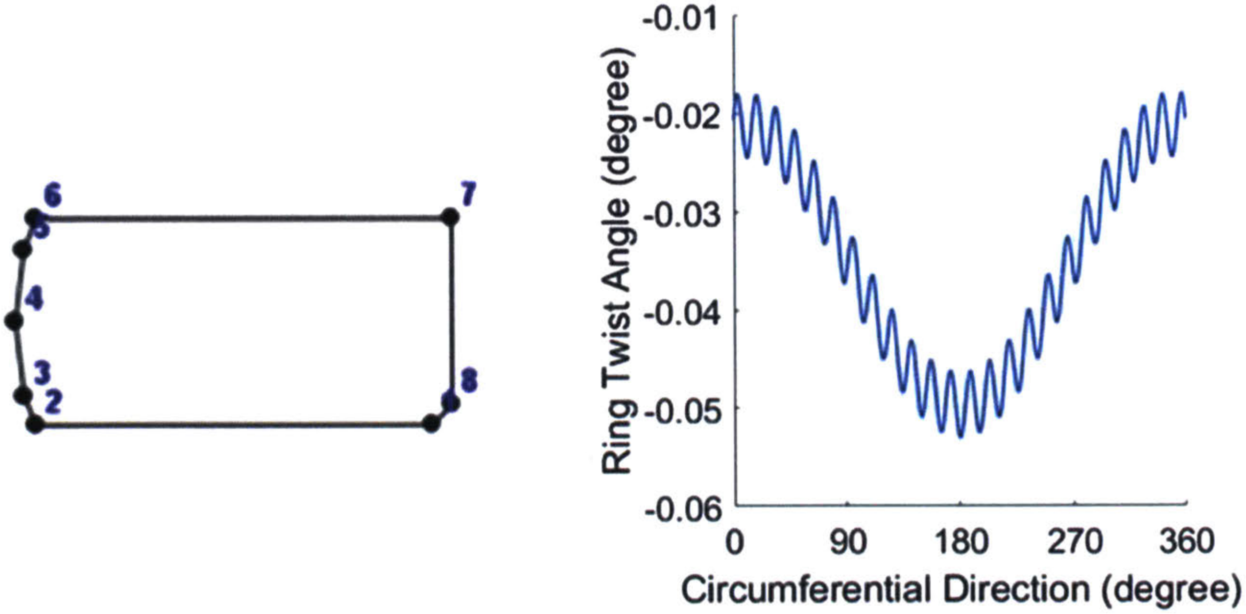

Figure 4.5 – Ring cross section with negative principal angle and the corresponding twist angle - tapping force as being applied on the ring internal upper corner

4.4. Sample results

In this section we compare the results obtained with our model to those given by the existing straight beam model. For all the cases we observe that the absolute value of the static twist is lower for our model. This shows an advantage of adopting the curved beam model compared to the straight beam one since it solves for a stability position with a lower static twist and thus a lower twist moment which is the intuition behind the static twist under fixed ID/OD constraint experiment. In fact the users try to figure out the stability position of the ring when it is closed to a circular shape with the minimum possible static twist. This explains the gradually increasing tapping force adopted in order to minimize the clearance with the lower stage but without introducing any force contact with it or any additional twist moment.

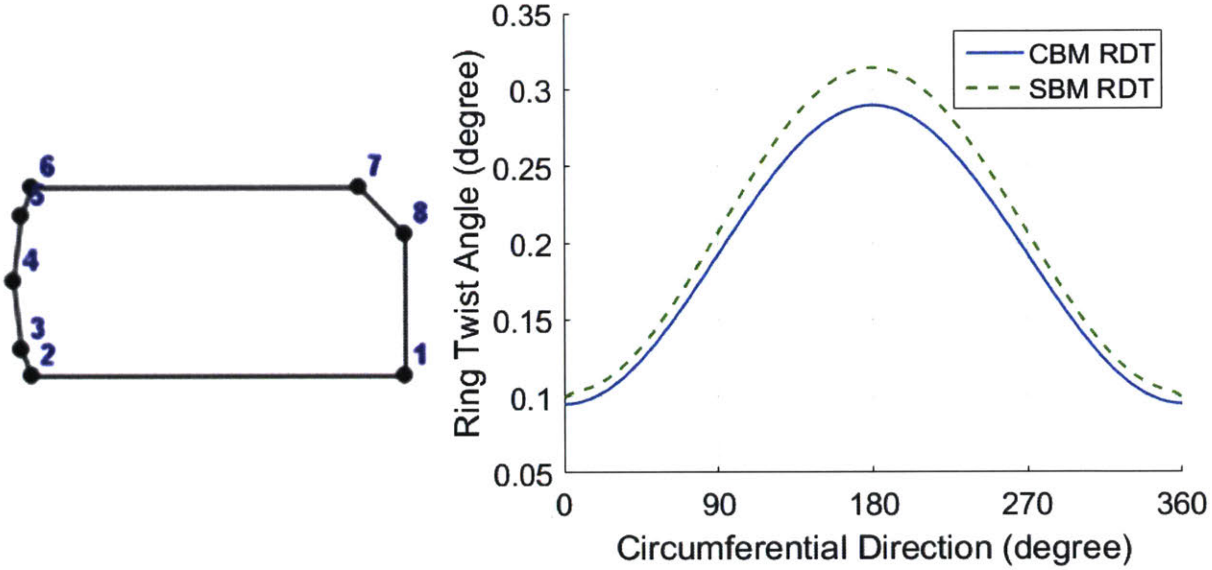

Figure 4.6 – Ring cross section with a 0.5 x 0.5 mm cut off on the internal upper corner of a 2 x 4 mm ring and the corresponding twist angle

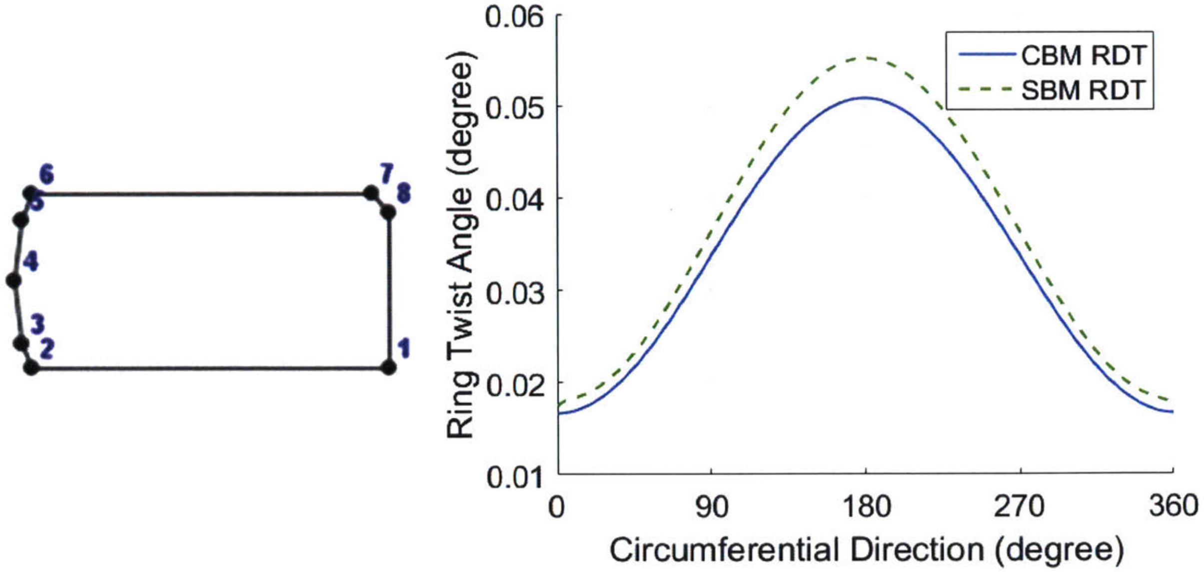

Figure 4.7 – Ring cross section with a 0.2 x 0.2 mm cut off on the internal upper corner of a 2 x 4 mm ring and the corresponding twist angle

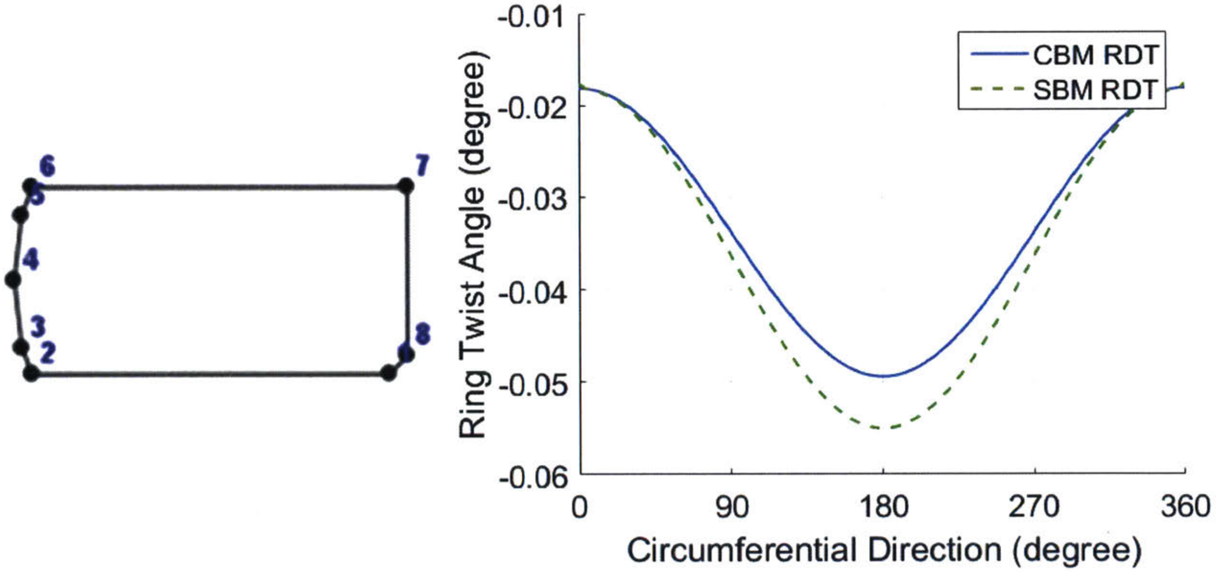

Figure 4.8 – Ring cross section with a 0.2 x 0.2 mm cut off on the internal lower corner of a 2 x 4 mm ring and the corresponding twist angle

Figures 4.6 and 4.7 show that the bigger the cut off engineered on the ring, the larger the absolute value of the static twist angle is. In fact for a larger cut off, the local twist moment distribution along the axial axis introduced by the radial force is bigger since the mass distribution varies in a wider range. Therefore the resulting static twist angle is bigger in absolute value.

Figures 4.7 and 4.8 show the almost symmetric results for the symmetric cut offs realized on the ring. The small discrepancy in the symmetry for the results obtained for the twist angle is due to the fact that the ring of Figure 4.7 with a positive twist and a minimum clearance at the internal lower corner is not symmetric to the case where the ring if Figure 4.8 with a negative twist and a minimum clearance at the external lower corner. Indeed, the centroid radial position is the same for these two rings but since the minimum clearance constraint is once applied on the internal lower corner and once on the external one, the twist angles needed won't be the opposite of each other because the distance between each of these points where we have the constraint and the centroid is not the same.

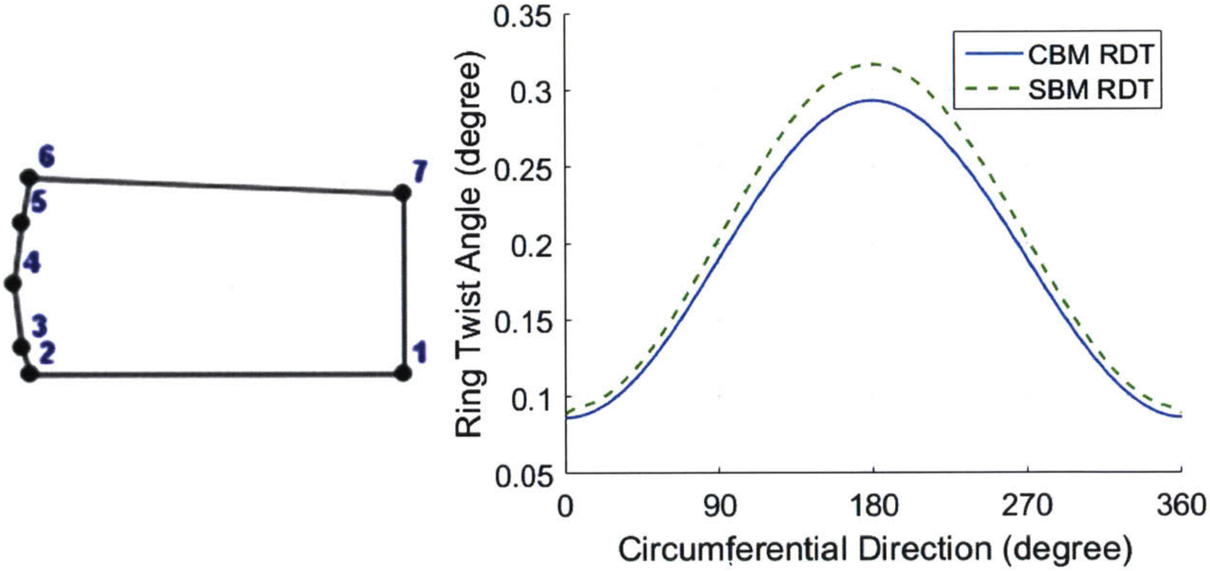

Figure 4.9 – Ring cross section with a cut off along the upper flank of a 2 x 4 mm ring and the corresponding twist angle

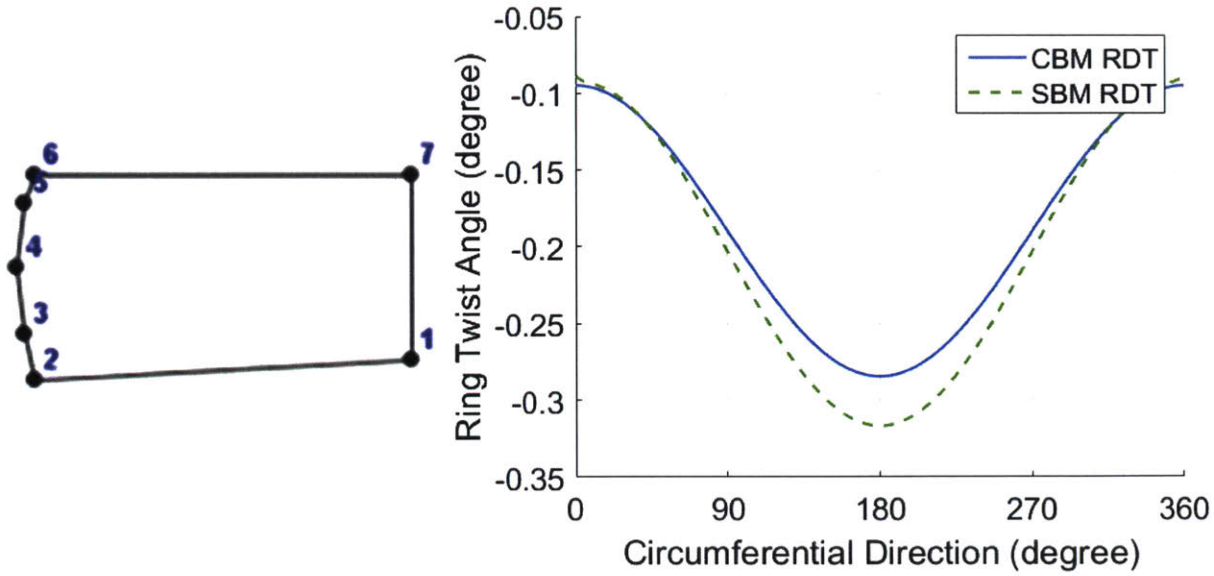

Figure 4.10 – Ring cross section with a cut off along the lower flank of a 2 x 4 mm ring and the corresponding twist angle

Figures 4.9 and 4.10 show the results obtained for rings with non-zero upper or lower flank angles. Again these two cases are not exactly symmetric since the radial distance between the centroid and the lower corner points where we have the constraint in each case is not the same: ali for the case of Figure 4.9 is different from alo of the ring in Figure 4.10. Therefore equations (4.5) and (4.7) are not equivalent for opposite α_r and hence we don't obtain perfectly opposite static twist angles.

4.5. Conclusion

We extended the curved beam model based on nodal displacements to determine the static twist under fixed ID/OD by simulating the axial taping force carried out in the experimental set-up. Translating the clearance constraint into equations and considering the tapping force as a variable we end up with a close system whose solution gives the static twist. A physical understanding of the generation of the static twist from the radial pressure was given and a study of the ring's asymmetry effect along with sample results were presented. Besides, developing a static twist under fixed ID/OD constraint based on curved beam model is essential to conceive a complete ring design tool based solely on that modelling that allows us to reach a better accuracy with less computation cost than the straight beam model as proven by Baelden [31].

This tool is of practical interest for ring designers to have an analytical tool that determines the ring static twist based on its design which will facilitate the iterative design process needed to obtain the desired static twist. In order to control oil and gas transport, compression rings are generally designed to have non-zero static twist. For instance, this feature makes the ring push against the top groove lower flank and make sure the ring prevents gas leakage when its upper surface is exposed to high gas pressure. This positive static twist as shown in the sample results can be achieved by creating a cut at the upper ID. The amplitude of the static twist can be tuned base on the dimensions of the cut off.

Our model is also able to consider non-zero gaps at the closed shape. This feature did not influence the results obtained for the geometries considered and more complicated cross section designs could be considered to investigate more the effect of non-zero gap. Furthermore, as stated previously, our framework is able to model the tapping force at other locations than on the centroid and also to impose smaller clearances constraint. These cases could also be considered in the future to model other experimental scenarios different from the ideal one. Finally our model can be extended further to include the tip lapping case.

5. Free shape, force distribution in circular bore and ovality

In this last section, we present the four sub-models developed to relate the ring free shape, its final shape when subjected to a constant radial pressure (this final shape is called ovality) and the force distribution in circular bore. To do so, we relate the free shape to each of the other two variables reciprocally. Knowing one of these distributions and combining the appropriate sub-models, one can determine the other two as explained in Figure 5.1.

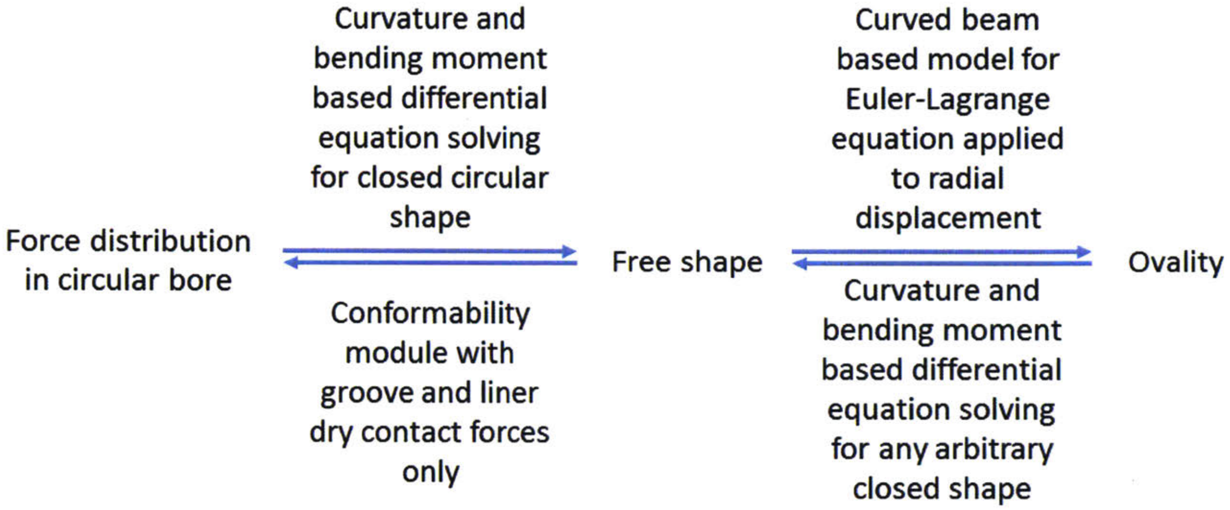

Figure 5.1 – Free shape, force distribution in circular bore and ovality sub-modals representation

Knowing the ring free shape and the constant radial pressure applied on it, we determine its ovality by considering the curved beam model and the Euler-Lagrange equation for radial displacement. By simulating the ring inside the groove and the cylinder with dry contact via the conformability module introduced in Chapter 3, we recover the force distribution in circular bore. Finally we developed a general framework that lets us recover the free shape from any final shape given a certain force distribution. In particular, this lets us determine the free shape from the force distribution in circular bore and also from the ovality and hence we have all the tools to relate the ring free shape, its ovality and force distribution in circular bore.

For the conformability module used to recover the force distribution from the free shape, we deal with the ring closing process as explained in section 2.4 since small displacement assumption is not valid. For the other 3 sub-models, that assumption is still violated so we use the general expression of the curvature for planar curve (2.9) applied to the free shape and the closed one instead of the simplified one (2.14).

Measuring the ovality is more accurate than doing so for the free shape or force distribution in circular bore. Thus, the tool we developed is useful in the sense that having a model that takes the ovality as an input is more convenient and useful based on the experiments carried out to characterize the ring. We validated our sub-models by recovering two theoretical force distributions provided by Mahle using the four modellings we have. Mahle also provided us with experimental measurement of the ovality but we were not able to recover the corresponding theoretical force distributions. Nevertheless, we investigated the reason behind it and gave an initial explanation.

5.1. Determining ring's force distribution in circular bore using its free shape

Determining the ring force distribution in circular bore using its free shape is simply carried out using the conformability module introduced in section 3 by considering only dry contact forces from the groove and the liner. We carry out the same modeling for the ring closing process as explained in section 2.4 by considering some initial force vector. Therefore we end up with the (2.107) finite element matrix equation to solve:

$$[K]\{u\} = \{F_{ext}\} - \{F_{intiial}\}$$

(2.107)

$F_{initial}$ is determined based on the ring free shape as stated in equations (2.82)-(2.84). F_{ext} contains the terms corresponding to the ring-liner and ring-groove dry contact forces and is assembled from the load vectors (2.100) coming from the different elements. The stiffness matrix K is also an assembly of the element based ones (2.98).

$$K_{ij}^{(e)} = \begin{cases} \dfrac{L_e E I_{zz}}{R^4}\displaystyle\int_0^1 \left(N_{m(i)} + N''_{m(i)}\right)\left(N_{m(j)} + N''_{m(j)}\right) d\eta & for\ \{i,j\} \in k_y \\ \dfrac{L_e}{R^2}\displaystyle\int_0^1 \left(E I_{yy} N_{\alpha m(i)} N_{\alpha m(j)} + G J_t N'_{\alpha m(i)} N'_{\alpha m(j)}\right) d\eta & for\ \{i,j\} \in k_\alpha \\ \dfrac{L_e}{R^4}\displaystyle\int_0^1 \left(E I_{yy} N''_{m(i)} N''_{m(j)} + G J_t N'_{m(i)} N'_{m(j)}\right) d\eta & for\ \{i,j\} \in k_z \\ \dfrac{L_e}{R^3}\displaystyle\int_0^1 \left(E I_{yy} N''_{m(i)} N_{\alpha m(j)} - G J_t N'_{m(i)} N'_{m(j)}\right) d\eta & for\ (i,j) \in k_z \times k_\alpha\ or\ (i,j) \in k_\alpha \times k_z \\ 0 & otherwise \end{cases}$$

(2.98)

$$F_{ext,i}^{(e)} = \begin{cases} \displaystyle\int_0^{L_e} f_r N_{m(i)} ds & for\ i \in k_y \\ \displaystyle\int_0^{L_e} f_z N_{m(i)} ds & for\ i \in k_z \\ \displaystyle\int_0^{L_e} m_t N_{\alpha m(i)} ds & for\ i \in k_\alpha \end{cases}$$

(2.100)

5.2. Determining ring's free shape using its force distribution in circular bore

The ring free shape is a key characterization of the ring. In practice designers need to determine the geometry of the ring free shape that will produces the desired ring tension and force distribution once the ring is closed to the bore diameter. This process relies mainly on internal proprietary formula and experimental results. The following modeling lets us recover the ring free shape from known force distribution along the ring circumference in circular bore.

To compute the ring free shape we determine first its curvature. To do so we use the bending moment equation (2.45) along the axial direction which is proportional to the curvature change in the radial one. We keep using the same notations introduced in Section 2.

$$M_{zz} = EI_{zz}(\kappa_{yy} - \kappa_{yy0})$$

(2.45)

κ_{yy} is the ovality curvature corresponding the curvature of the closed ring while κ_{yy0} is the free shape curvature. Since the final shape is a circular one, $\kappa_{yy} = \frac{1}{R}$.

The bending moment is calculated from the force distribution starting from the ring gap $\theta = 0$ which is a free end without any internal or external stress. The integral expression of the local bending moment based on the radial force distribution for a closed circular shape is given by the following expression. A more general expression for any arbitrary closed shape will be given in section 5.4.

$$M_{zz} = \int_0^{\theta} P(\alpha)\, R^2 \sin(\theta - \alpha)\, d\alpha$$

(5.1)

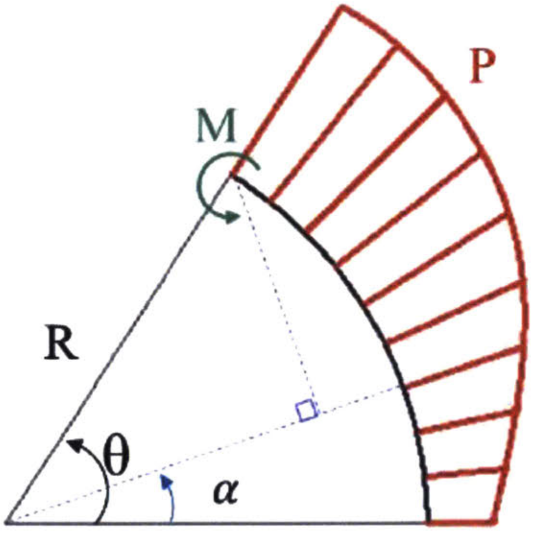

Figure 5.2 – Bending moment and radial force distribution

$P(\alpha)$ is the contact pressure distribution applied on the ring when it is closed to the circular shape. R is the ring nominal radius and α is the angle swiping from 0 to θ.

Using equation (2.9) for planar curve, we can express the ring free shape curvature (5.2).

$$\kappa_{yy0} = \frac{r_{fs}^2 + 2r_{fs}'^2 - r_{fs}r_{fs}''}{\left(r_{fs}^2 + r_{fs}'^2\right)^{\frac{3}{2}}}$$

(5.2)

$$r_{fs} = R + y_0$$

(5.3)

r_{fs} is the radius of the ring free shape. When the ring is closed from its free shape to the round one, the element ds of the ring changes its angular position from θ_{fs} to θ_{rs} as shown in Figure 5.3. Therefore, the curvature change calculation needs to be carried out on a specified ring differential element ds instead of an angular position θ. Since the closed shape is a circular one (2.45) can be re-written as follows and based on the arc length coordinate s instead of θ:

$$\kappa_{yy0}(s) = \frac{1}{R} - \frac{M_{zz}\left(\frac{\pi R - s}{R}\right)}{EI_{zz}}$$

(5.4)

The arc length coordinate is chosen such that $s = 0$ at the back of the ring. To obtain an arc length coordinate based differential system, we should relate ds to $d\theta$ which is done by simplifying (2.7) for a planar curve to obtain:

$$ds = \sqrt{r_{fs}^2 + r_{fs}'^2 d\theta}$$

(5.5)

By combining (5.1), (5.2), (5.4) and (5.5) along with the boundary conditions specified below (5.6)-(5.11), we solve the ring free shape numerically.

$$\theta(s = 0) = 180°$$

(5.6)

$$r_{fs}(s = 0) = R$$

(5.7)

$$\frac{dr_{fs}}{d\theta}(s=0)=0$$

(5.8)

$$\frac{d\theta}{ds}(s=0)=\frac{1}{R}$$

(5.9)

$$\frac{dr_{fs}}{ds}(s=0)=0$$

(5.10)

$$\frac{d}{ds}\left[\frac{dr_{fs}}{d\theta}\right](s=0)=\frac{RM_{zz}(s=0)}{EI_{zz}}$$

(5.11)

The ring free shape curvature can be computed directly by combining only (5.1) and (5.4) without solving any differential equation which gives more accurate results than evaluating the curvature from the solution obtained for the ring free shape r_{fs} based on (5.2). This is of utmost importance since when using the free shape as input to any of our models, either to determine the force distribution in circular bore or the ovality, all we need to use is the curvature which appears in the resulting Euler-Lagrange equation in each case (that term is inserted in the initial load vector in our conformability module that we use to determine the force distribution in circular bore) and once we know the curvature we don't need to use neither the ring free shape r_{fs} nor its first or second derivatives.

5.3. Determining ring's ovality using its free shape

Given a certain ring design, by applying a certain constant pressure on it we can make its gap closed. The final shape obtained afterwards is called ovality. We also use this name to design the final shape obtained after applying a constant radial pressure on the ring whether the gap is perfectly closed or not, but by specifying its value in the latter case.

To determine the ovality from the free shape, we can use solve the Euler-Lagrange equation since we are looking at the final static state of the ring. Therefore the finite element curved beam model can be used.

In this case, we only have the strain energy related to in plane bending that we derived in section 2.

$$U^{(e)} = U_{zz}^{(e)} = \frac{1}{2}\int_0^{L_e} EI_{zz}\left(\kappa_{yy} - \kappa_{yy0}\right)^2 ds$$

(5.12)

κ_{yy} is the ovality curvature corresponding the curvature of the closed ring while κ_{yy0} is the free shape curvature that we have as input. Below is the expression of the ovality curvature where R is the ring nominal radius and y the radial displacement. We use equation (2.9) for planar curves.

$$\kappa_{yy} = \frac{(R+y)^2 + 2y'^2 - (R+y)y''}{[(R+y)^2 + y'^2]^{\frac{3}{2}}}$$

(5.13)

The work of external contains only the constant radial force.

$$W^{(e)} = \int_0^{L_e} f_{ov} y ds = f_{ov}\int_0^{L_e} y ds$$

(5.14)

We use 5th order spline interpolation for radial displacement as introduced in section 2.

$$y(\eta) = \textstyle\sum_{k=1}^{6} N_k(\eta) u_{yk} \text{ where } \{u_y\} = \{u_{y1} \dots u_{y6}\}^T = \{y_1, y_1', y_1'', y_2, y_2', y_2''\}^T$$

(2.20)

$$y'(\eta) = \sum_{k=1}^{6} N_k'(\eta) u_{yk}$$

(2.28)

$$y''(\eta) = \sum_{k=1}^{6} N_k''(\eta) u_{yk}$$

(2.29)

Using the Hamilton's principle, we obtain the Euler-Lagrange equations for each ring element.

$$L^{(e)} = W^{(e)} - U^{(e)}$$

(5.15)

$$\frac{\partial L^{(e)}}{\partial u_{yi}} = 0 \text{ for } i = \{1 \ldots 6\}$$

(5.16)

The variable u_i represents the i$^{\text{th}}$ degree of freedom of the system composed by the two nodes of the ring element and when assembled in one vector, form the radial displacements and their derivatives at those nodes (5.17). Subscripts 1 and 2 refer to the first and second node of the element respectively.

$$u_y^{(e)} = \{u_{y1}, \ldots, u_{y6}\} = \{y_1, y_1', y_1'', y_2, y_2', y_2''\}$$

(5.17)

Combining (5.12), (5.14), (5.15) and (5.16), we obtain the following equations to solve for each ring element:

$$L_e E I_{zz} \int_0^1 (\kappa_{yy} - \kappa_{yy0}) \left(\frac{\partial \kappa_{yy}}{\partial y} N_i + \frac{\partial \kappa_{yy}}{\partial y'} N_i' + \frac{\partial \kappa_{yy}}{\partial y''} N_i'' \right) d\eta = L_e f_{ov} \int_0^{L_e} N_i d\eta$$

(5.18)

κ_{yy}, $\frac{\partial \kappa_{yy}}{\partial y}$, $\frac{\partial \kappa_{yy}}{\partial y'}$ and $\frac{\partial \kappa_{yy}}{\partial y''}$ are expressed using (5.13) and (2.20), (2.28) and (2.29) so that we end up with an equation in terms of $u_y^{(e)} = \{u_{y1}, \ldots, u_{y6}\}$ to solve.

In order to obtain the finite element equations for the complete ring, we assemble the terms obtained in (5.18) for the different ring elements as explained in section 2.6 for the vector assembly. The two extreme nodes corresponding to the ring tips belong to only one element. Thus, the equations for their radial displacements and their first two derivatives are simply in the form of (5.18) applied to the corresponding elements. Any other node belongs to two elements. Therefore the equation satisfied by the radial displacement and its two first derivatives for these nodes are the sum of two equations in the form of (5.18) applied to the two elements to which belongs the node. We end up with a non-linear system that we solve using Newton-Raphson algorithm.

5.4. Determining ring's free shape using its ovality

Determining the ring free shape from its ovality is a generalization of the process described in section 5.2 where we determined the ring free shape from the force distribution in circular bore. In this section, we derive the equation to be solved in order to determine the free shape from any closed shape with any pressure distribution applied to it.

To compute the ring free shape, we determine first its curvature using the bending moment equation (2.45) along the axial direction. The difference with the circular shape is in the integral expression of the local bending moment (Figure 5.3).

$$M_{zz} = EI_{zz}\left(\kappa_{yy} - \kappa_{yy0}\right)$$

(2.45)

$$M_{zz} = \int_0^{\theta} P(\alpha)\, r_{ov}(\alpha)\, f(r_{ov}(\alpha), \alpha, \theta) d\alpha$$

(5.19)

$$f(r_{ov}(\alpha), \alpha, \theta) =$$

$$\frac{\left|(r_{ov}'(\alpha)\cos(\alpha) - r_{ov}(\alpha)\sin(\alpha))r_{ov}(\theta)\cos(\theta) + \left(r_{ov}'(\alpha)\sin(\alpha) + r_{ov}(\alpha)cos(\alpha)\right)r_{ov}(\theta)\sin(\theta) - r_{ov}(\alpha)r_{ov}'(\alpha)\right|}{\sqrt{(r_{ov}'(\alpha)\cos(\alpha) - r_{ov}(\alpha)\sin(\alpha))^2 + (r_{ov}'(\alpha)\sin(\alpha) + r_{ov}(\alpha)\cos(\alpha))^2}}$$

(5.20)

We can check that equation (5.19) is consistent with (5.1) since for a final circular shape, $r_{ov}(\alpha) = r_{ov}(\theta) = R$ and thus $f(r_{ov}(\alpha), \alpha, \theta) = R|\sin(\theta - \alpha)|$. Since $0 \le \theta \le \pi$ and $0 \le \alpha \le \theta$ we have $0 \le \theta - \alpha \le \pi$ and thus $f(r_{ov}(\alpha), \alpha, \theta) = R\ \sin(\theta - \alpha)$. Therefore (5.19) is reduced to (5.1).

κ_{yy} is the ovality curvature corresponding the curvature of the closed ring. We expressed as in (5.13), where R is the ring nominal radius and y the radial displacement. We use equation (2.9) for planar curves.

$$\kappa_{yy} = \frac{(R+y)^2 + 2y'^2 - (R+y)y''}{[(R+y)^2 + y'^2]^{\frac{3}{2}}}$$

(5.13)

The ring free shape curvature equations (5.2) and (5.4), arc length coordinate based differential equation (5.5) and boundary conditions (5.6)-(5.11) are still valid.

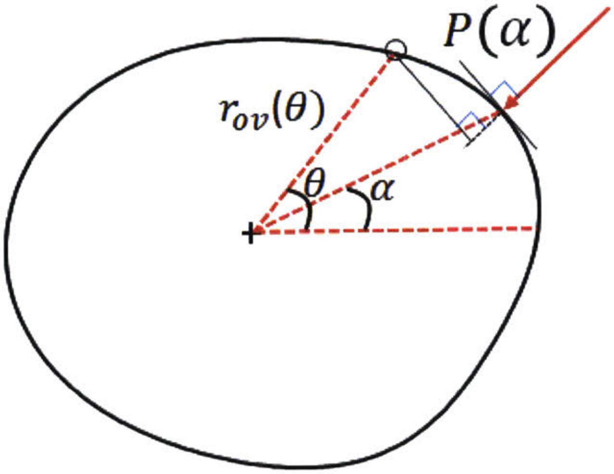

Figure 5.3 – Bending moment and radial force distribution for any arbitrary closed shape

The ring free shape curvature can be computed directly by combining only (5.19) and (5.4) without solving any differential equation to obtain more accurate results than using r_{fs} based on (5.2). As stated before, this is useful since when we will use the free shape results as input to another sub-model, all we need is its curvature.

5.5. Validation of the four models

In this section we present a theoretical validation of the four models based on data provided by Mahle. We have two different data sets for the same ring of rectangular cross section with a radial width equal to $4\ mm$ and an axial one equal to $2\ mm$. The nominal radius is of $45.625\ mm$. Each data set corresponds to a certain pressure distribution and therefore to a specific ovality and free shape. Tomanik presented a theoretical study and experimental procedure to characterize the free shape and ovality of these two ring types [47]. We call these data sets by the Usual and the TC one, using the same nomenclature given to the rings. The linear force distribution (force per ring axial width) for each of them is plotted in Figure 5.4. When closed, the gap clearance for the Usual case is equal to $0.48\ mm$, while it is $0.4\ mm$ for the TC one.

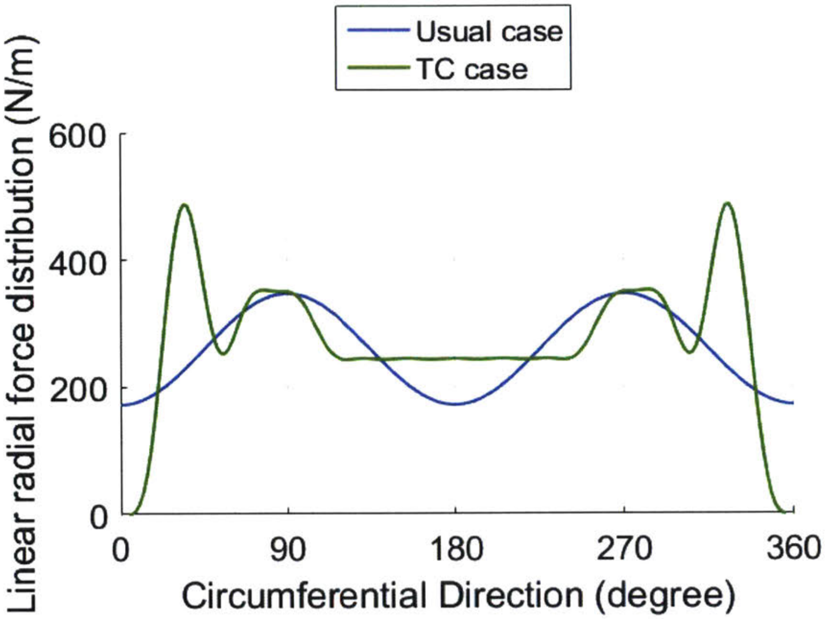

Figure 5.4 – Theoretical linear radial force distribution for usual and TC cases

In order to validate theoretically the four models introduced previously, we start with these force distribution to compute the corresponding free shapes and then the ovalities using sections 5.2 and 5.3 models respectively. Then using sections 5.4 and 5.1 respectively we recover the free shapes and force distributions. Based on Figure 5.1 this is equivalent to going from left to right and then in the opposite direction.

As stated in sections 5.2 and 5.4, at any time we compute the ring free shape we keep the curvature computed from the relation based on the bending moment and not from the expression based on the radial coordinates of the ring free shape which involves first and second derivatives. We will also compare the free shape and its curvature computed from the force distribution and from the ovality.

All our models rely on the usual representation for the free shapes and ovality. It means that the radial coordinates are computed as the distance between the ring points and the center of the circle adjacent to the ring back with a radius equal to the ring nominal radius. This representation is illustrated in Figure 5.5. Mahle data sets are available in the centralized representation where the radial coordinates are defined as the distance between the ring points and center of the circle passing through the ring back and the tips as presented in Figure 5.6.

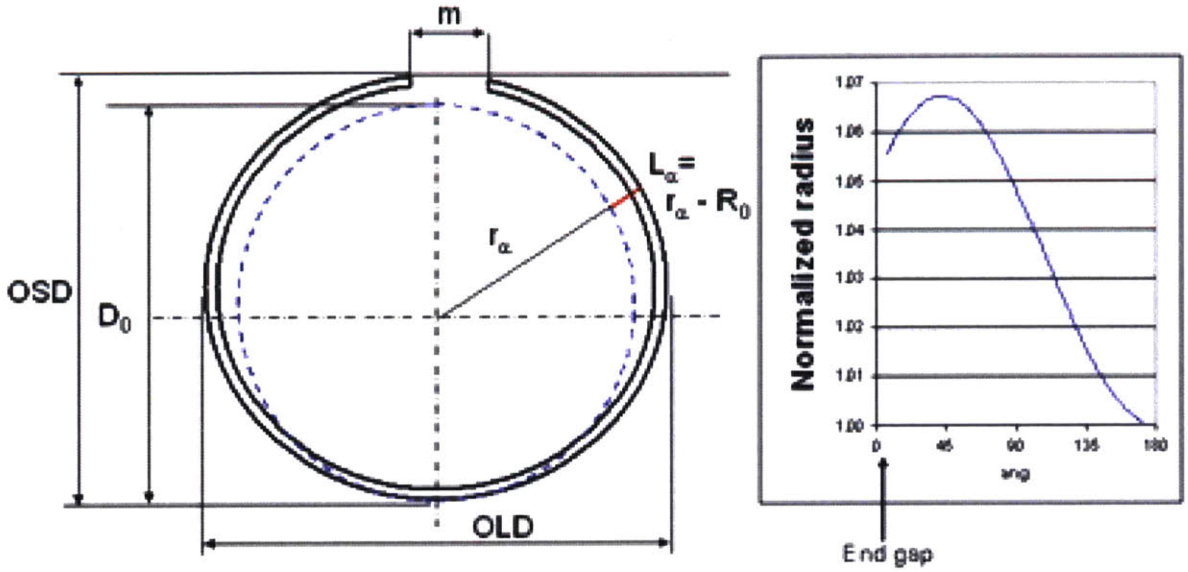

Figure 5.5 – Free shape usual representation (Figure provided by Mahle)

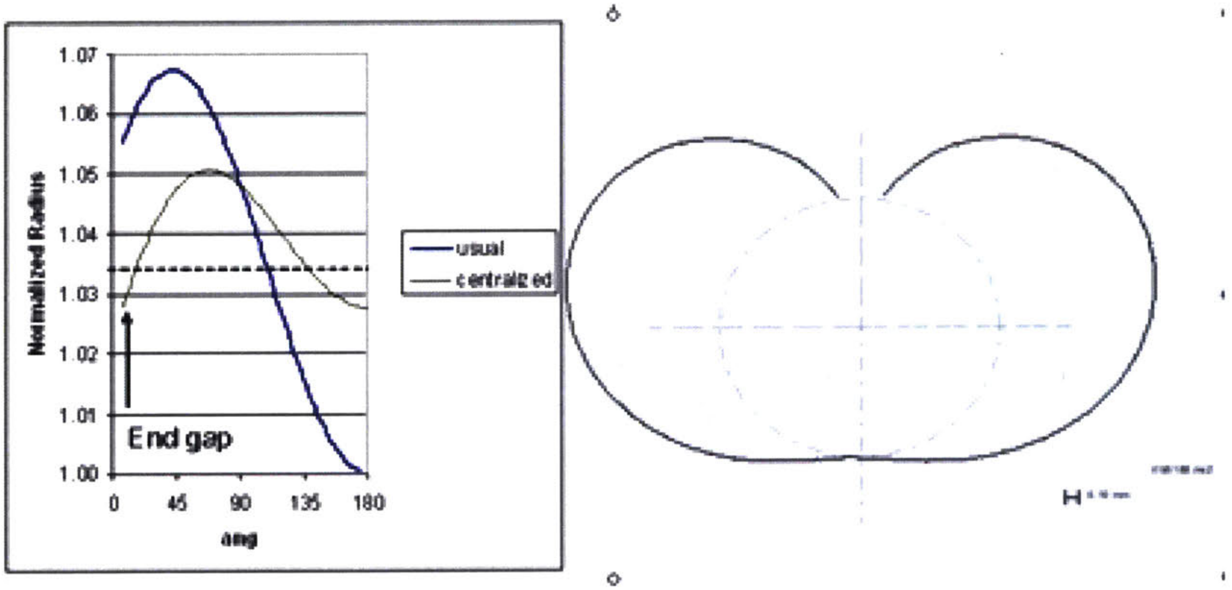

Figure 5.6 – Free shape centralized representation (Figure provided by Mahle)

Figure 5.7 show the ovality obtained from the theoretical pressure distribution for the usual case in radial coordinates and its comparison with the measured one using the centralized representation. Figure 5.8 provides the same results for the TC case. In the sub model computing the ovality from the free shape, we use 16 elements.

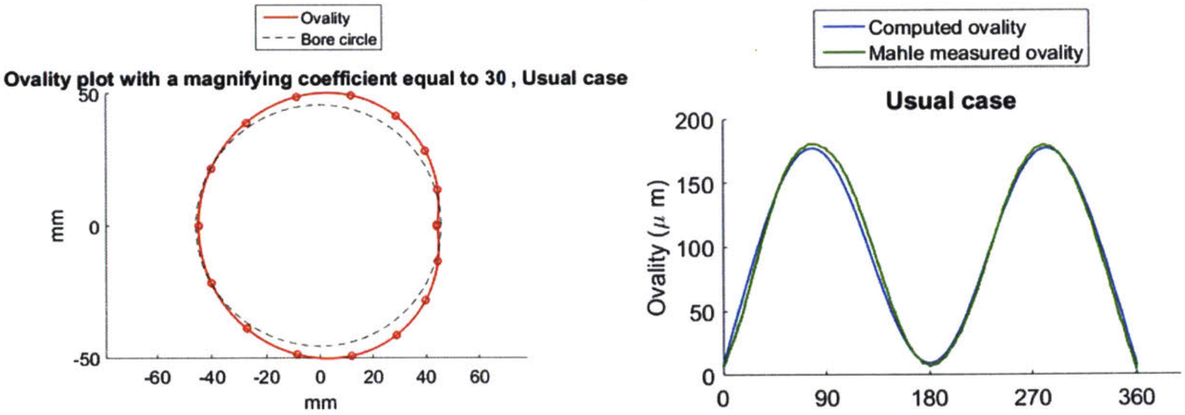

Figure 5.7 – Ovality obtained from theoretical force distribution compared to the measured one in centralized representation (Usual case)

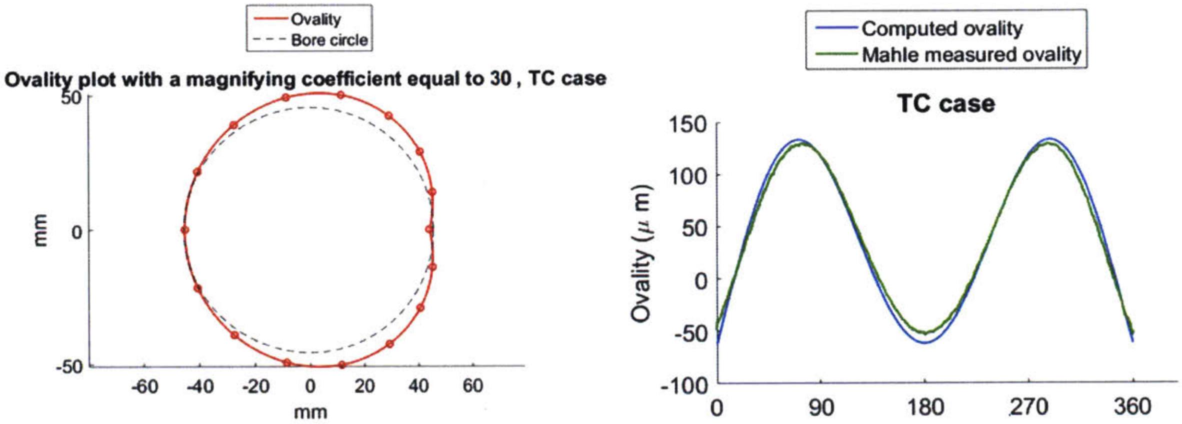

Figure 5.8 – Ovality obtained from theoretical force distribution compared to the measured one in centralized representation (TC case)

Figures 5.9 and 5.10 show the results obtained for the free shapes in the usual representation at two different steps: when computed from the theoretical force distribution and when determined from the ovality computed by our models. We notice that our models are consistent since they recover the same free shape for each case. We obtained a maximum relative error between the two free shapes of 0.6% for the two cases.

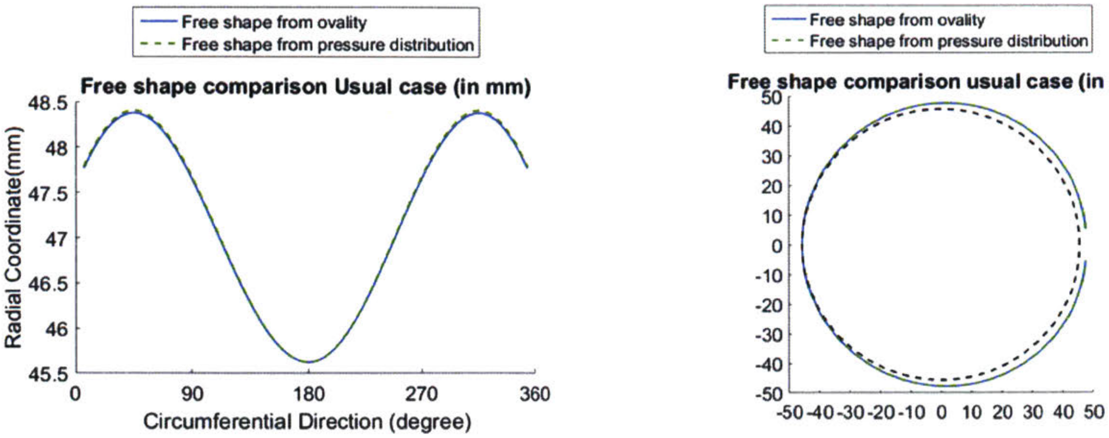

Figure 5.9 – Comparison of free shape obtained from theoretical force distribution and from computed ovality in usual representation (usual case)

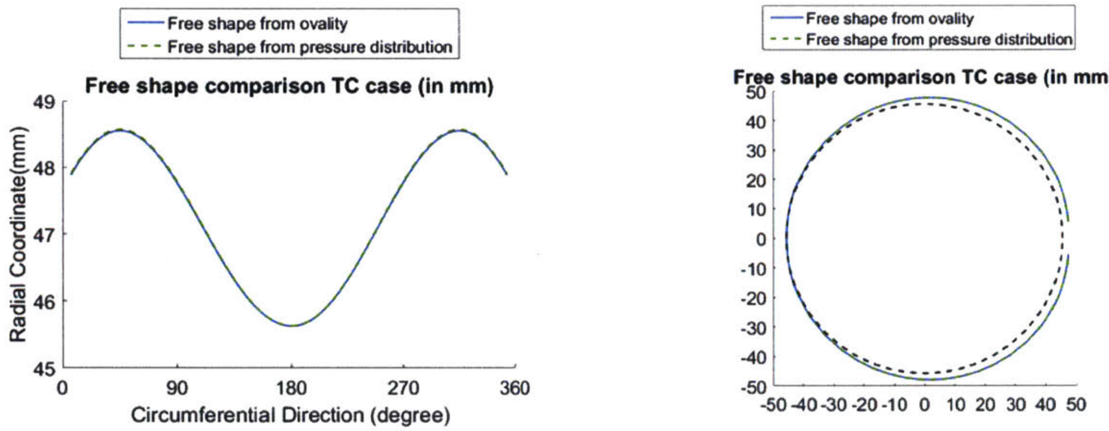

Figure 5.10 – Comparison of free shape obtained from theoretical force distribution and from computed ovality in usual representation (TC case)

In figures 5.11 and 5.12, we compare three different free shape curvatures. The dashed green one corresponds to the free shape curvature obtained from the theoretical force distribution using equation (5.4). The blue curve is the free shape curvature computed from the momentum equation (2.45) applied to the ovality computed in our model. Finally, the dashed red curve shows the free shape curvature computed using equation (5.2) after solving for the ring free shape radial coordinates using the ovality computed in our model. Again our models are consistent and provide the same results for the curvature for both the usual and the TC cases. For the usual case, we obtain a maximum relative error of 0.02% for the curvature computed from the momentum equation and an error of 0.07% for the one computed using the free shape radial coordinates. For the TC case, we obtain a maximum relative error of 0.03% for the curvature computed from the momentum equation and an error of 0.08% for the one computed using the free shape radial coordinates.

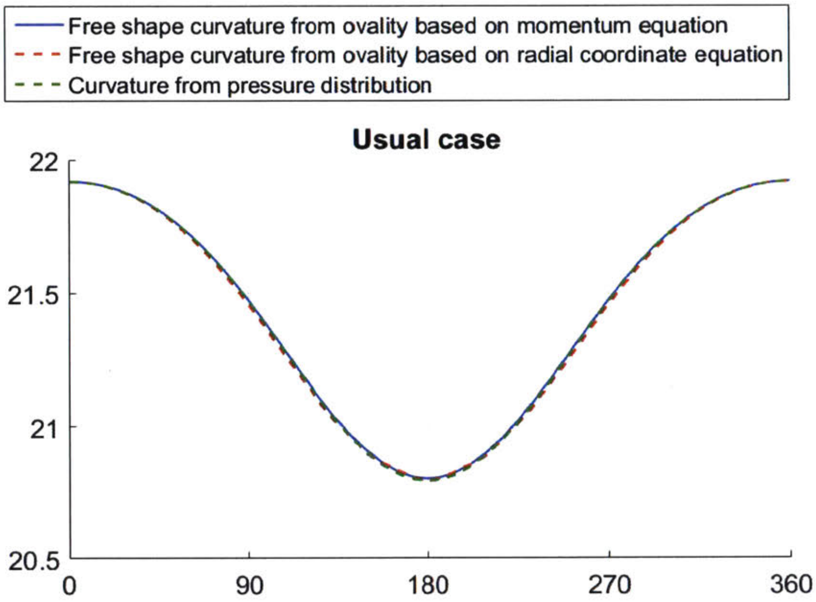

Figure 5.11 – Free shape curvature comparison (Usual case)

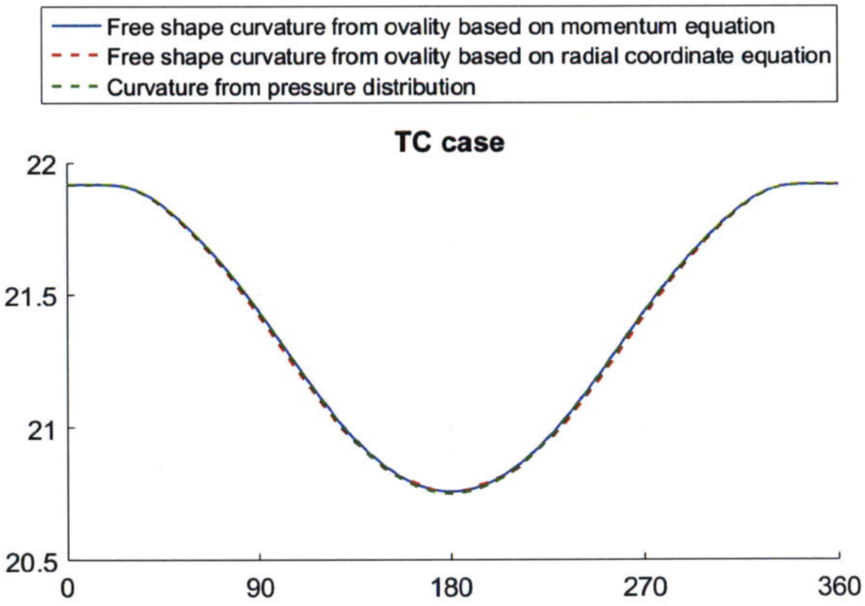

Figure 5.12 – Free shape curvature comparison (TC case)

Finally we use our last sub model of section 5.1 to retrieve the force distribution in closed circular shape using the free shape curvature computed from the ovality that we determined. We use the free shape curvature determined using the momentum equation (2.45) based on the ovality (curvature in blue curve in Figures 5.11 and 5.12). The results are presented in Figures 5.13 and 5.14. In the last sub model computing the force distribution from the free shape, we use 16 elements and 1000 points per element for the force evaluations.

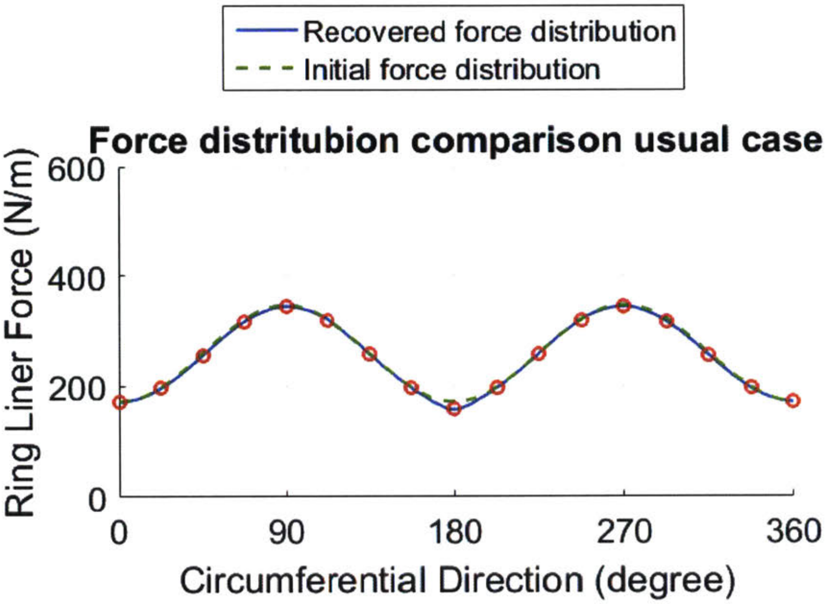

Figure 5.13 – Force distribution comparison (Usual case)

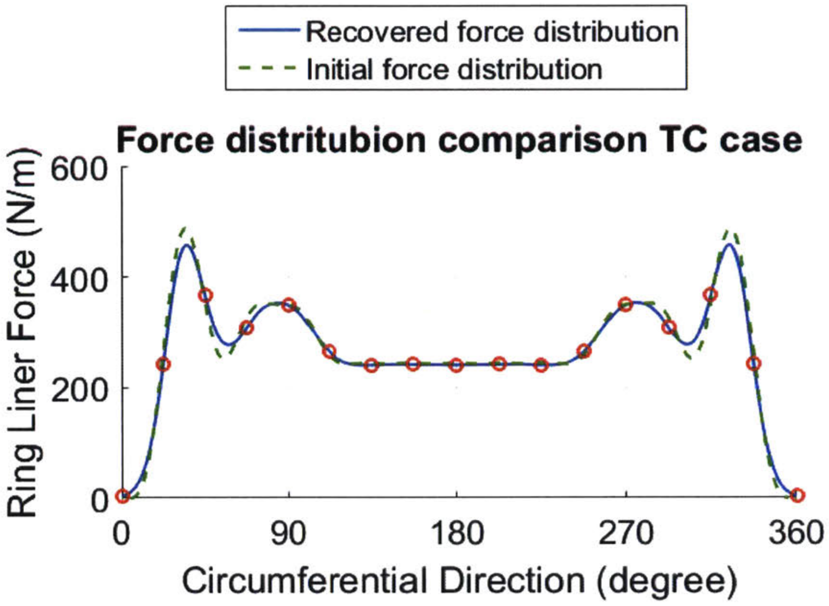

Figure 5.14 – Force distribution comparison (TC case)

As explained in section 5.1 the force distribution is taken as the force applied from the liner on the ring. The contact model adopted, the roughness of the liner and its material related properties explain the small differences we observe in the two force distributions since the provided one is a theoretical one and independent from the source applying it on the ring.

As a conclusion our four sub models are consistent all together and able to recover the inputs we provide them with by determining any two variables from the third one among the ring free shape, its ovality and the force distribution in closed circular shape. However, our models showed some limits when we tried to validate them with experimental measurements. More details are provided in the following section along with some explanations regarding the discrepancies observed which are not only related to our models but also to the measurement deviations.

5.6. Validation of the model using ovality measurement

Besides the theoretical force distribution, Mahle provided us with measured ovality for the usual and the TC cases that has been used in Tomanik's work [47]. In this section we will present the results obtained from our model using these experimental data sets. The first sub part will be devoted to the description of the data processing procedure and the second one contains the results obtained.

5.6.1. Ovality data processing

The ovality measurement is carried out using a stylus-based equipment. We carry out the data processing by approximating the measures with the 5th order polynomial shape functions introduced in the curved beam model (2.22)-(2.27). Therefore the radial displacement will have the (2.20) interpolation form for each element.

$$y(\eta) = \sum_{k=1}^{6} N_k(\eta) u_{yk} \text{ where } \{u_y\} = \{u_{y1} \dots u_{y6}\}^T = \{y_1, y_1', y_1'', y_2, y_2', y_2''\}^T$$

(2.20)

We carry out the interpolation using the least square method. N_d refers to the number of data points, and N to the number of nodes consider in the interpolation. If we note the measures by $r = \left[(r_i)_{i=1}^{N_d}\right]$ for the radial displacement and by $(\eta_i)_{i=1}^{i=N_d} = (\theta_i)_{i=1}^{i=N_d}$ for the circumferential direction, the least square method minimizes S given by (5.14) with respect to $(y_i, y_i', y_i'')_{i=1}^{i=N}$, where the $y(\eta_i)$ corresponds to the approximation of r_i using the function $y(\eta)$ at the element to which belongs the ith point.

$$S = \sum_{i=1}^{N_d} \left(r_i - y(\eta_i)\right)^2$$

(5.14)

If we note y_{nodes} the vector containing the radial displacements and their first and second derivative at the nodes (5.15), the least square method reduces to solve the matrix equation (5.16) derived by setting the derivatives of S with respect to the elements of y_{nodes} to zeros.

$$y_{nodes} = \begin{bmatrix} y_i \\ y_i' \\ y_i'' \end{bmatrix}_{i=1..N}$$

(5.15)

$$X^T.X.y_{nodes} = X^T.r$$

(5.16)

X is an N_d by $3N$ block matrix based on the evaluation of the different shape functions (2.22)-(2.27) at the measurement locations. By imposing the continuity of the third derivatives at the nodes belonging to two elements (i.e. all nodes except the two corresponding to the ring tips), we obtain a matrix relation between the vectors $d2y$ and y_{prim}, where the matrix C is $N-2$ by $2N+2$ and depends on the angular length of the elements.

$$d2y = [y_i'']_{i=2\ldots N-1}$$

(5.17)

$$y_{prim} = \begin{bmatrix} y_1'' \\ y_1 \\ y_1' \\ y_2 \\ y_2' \\ \ldots \\ y_{N-1} \\ y_{N-1}' \\ y_N \\ y_N' \\ y_N'' \end{bmatrix}$$

(5.18)

$$d2y = C.y_{prim}$$

(5.19)

Combining (5.16) and (5.19) we end up with a matrix equation relating y_{prim} and r (5.20), where A is an N_d by $2N+2$ matrix computed from blocks from X and C.

$$A^T.A.y_{prim} = A^T.r$$

(5.20)

In conclusion, we solve for y_{prim} using (5.20) then for $d2y$ using (5.19) which lets us completely determine y_{nodes}. Therefore we obtain our fitted ovality using the shape functions. The measured and fitted ovality for the two cases are plotted in Figures 5.15 and 5.16. The average difference between the measures and their fit is in the order of $10^{-10}m$.

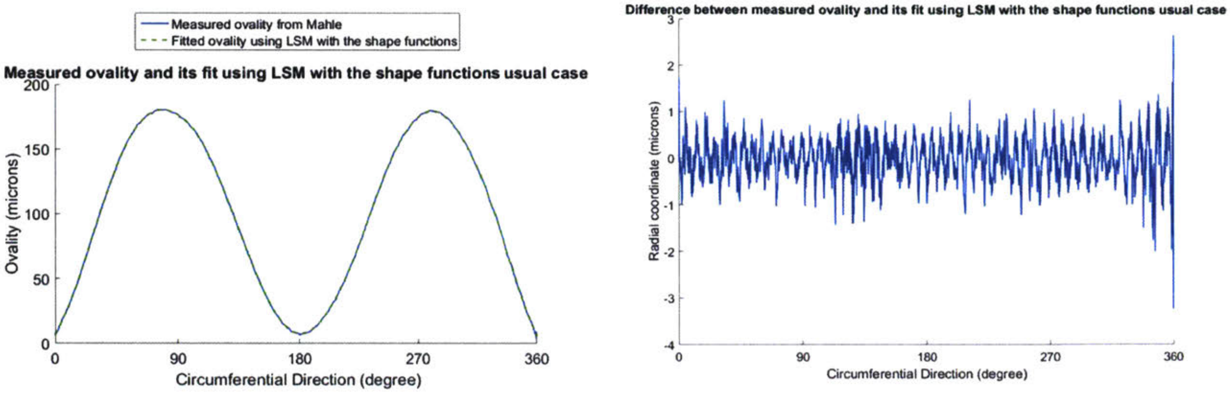

Figure 5.15 – Fitted measured ovality in centralized representation (Usual case)

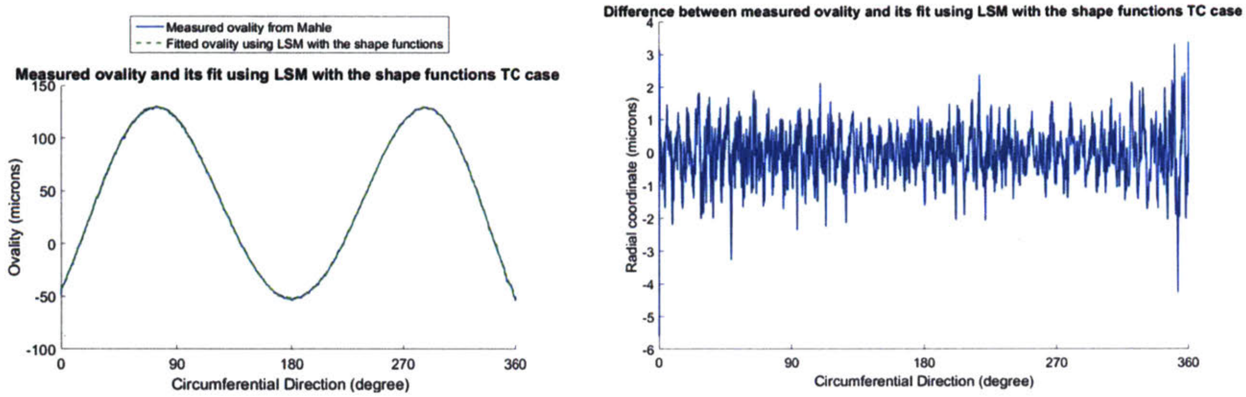

Figure 5.16 – Fitted measured ovality in centralized representation (TC case)

Once we have our fitted data in the centralized representation, we convert it to the usual one and use our models of section 5.4 and 5.1 to recover the ring free shape and the force distribution for the closed circular shape. The corresponding results are presented in the following section.

5.6.2. Results

After using the sub model corresponding to section 5.4 we obtain the ring free shape and its curvature. Figures 5.17 and 5.18 present the results for the usual case while Figures 5.19 and 5.20 show the outputs for the TC case. We conclude that we are still able to recover the right free shape even when using the ovality measures. The maximum relative error has slightly increased compared to the free shape computed from the theoretical ovality as done in section 5.5 in the theoretical validation of the model since if goes from 0.6% to 0.7%.

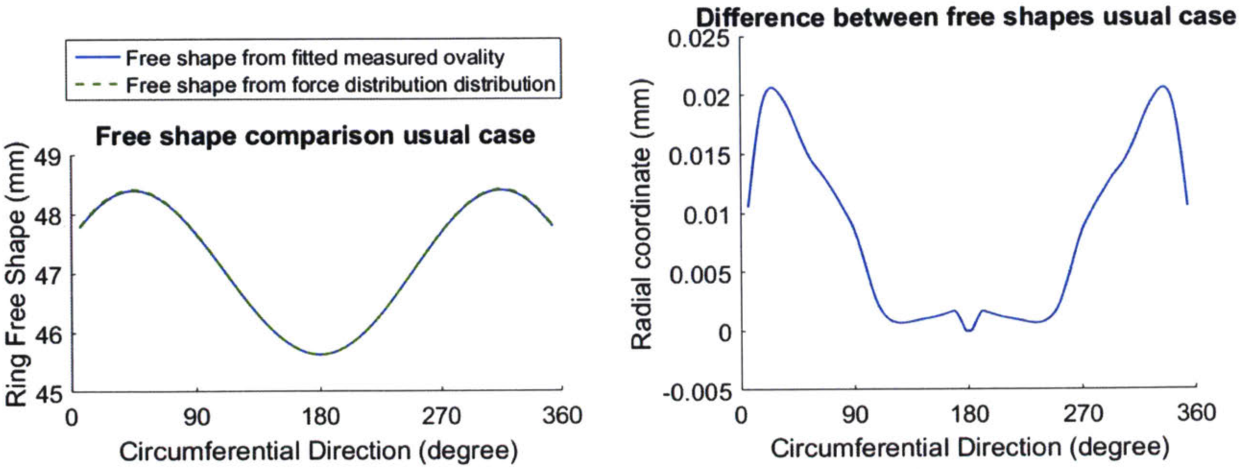

Figure 5.17 – Comparison of free shape obtained from theoretical force distribution and from measured ovality in usual representation (usual case)

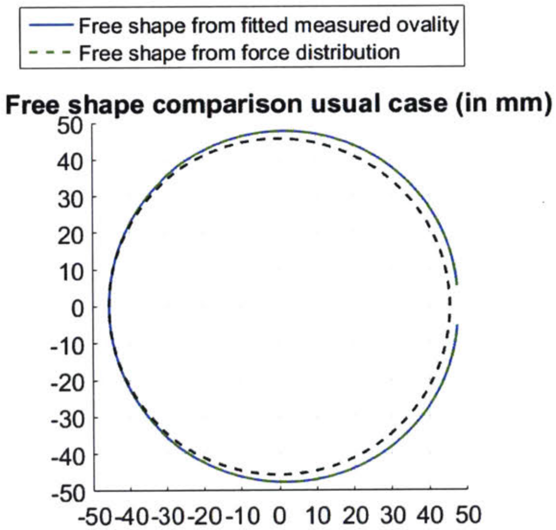

Figure 5.18 – Comparison of free shape obtained from theoretical force distribution and from measured ovality in radial plots (usual case)

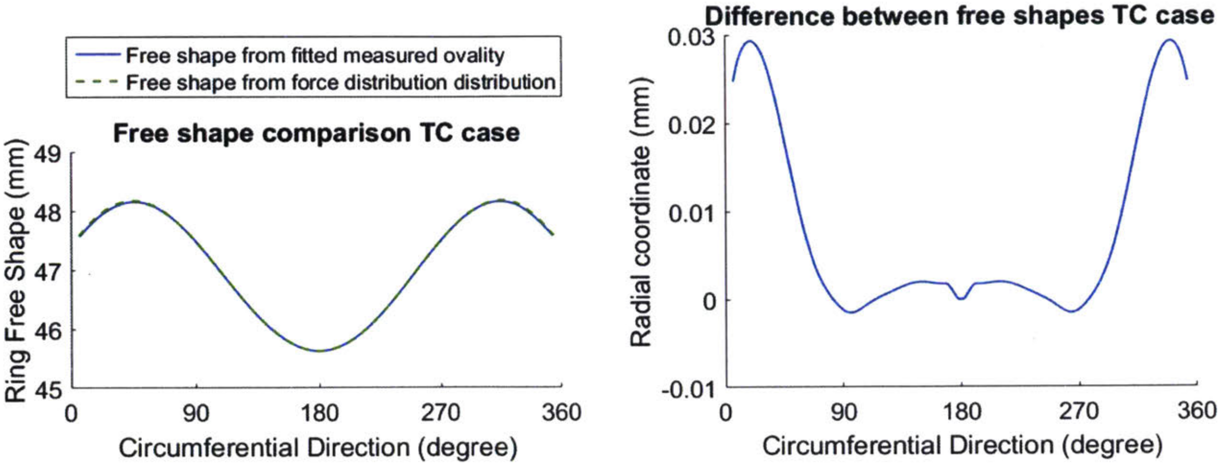

Figure 5.19 – Comparison of free shape obtained from theoretical force distribution and from measured ovality in usual representation (TC case)

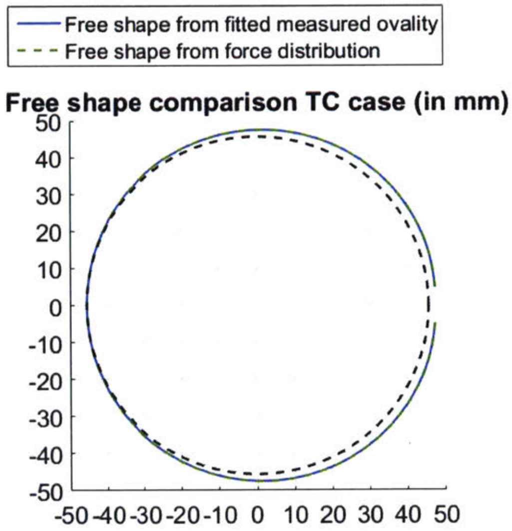

Figure 5.20 – Comparison of free shape obtained from theoretical force distribution and from measured ovality in radial plots (TC case)

The following graphs Figure 5.21 and 5.22 show the results obtained for the free shape curvatures. We observe that the difference between the free shape curvature obtained from the theoretical force distribution used in section 5.5 and the curvatures computed from the measured ovality is well more significant than the difference observed in the free shape. Indeed the maximum relative error goes from 0.02% to 0.46% for the usual case regarding the curvature computed from the momentum equation and from 0.03% to 0.49 % for the TC case.

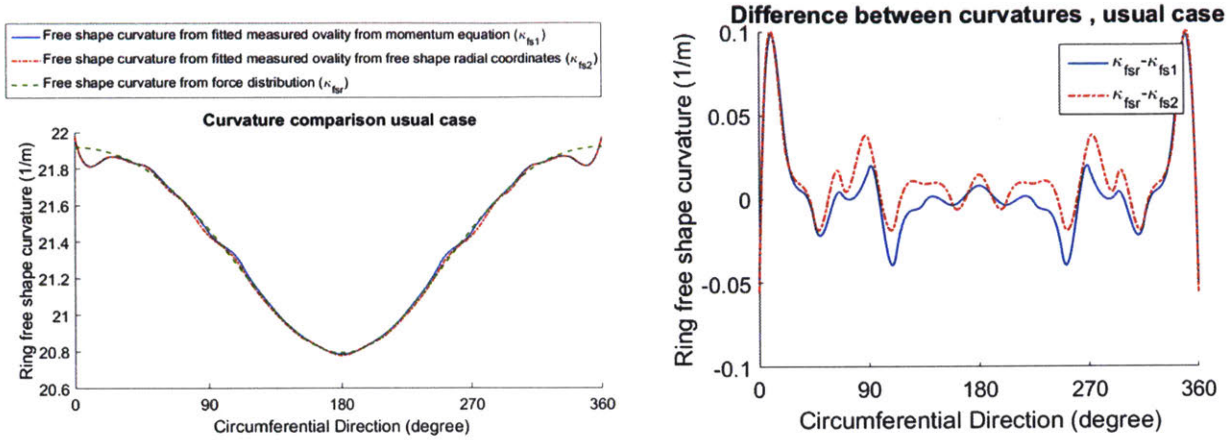

Figure 5.21 – Free shape curvature comparison for measured ovality (Usual case)

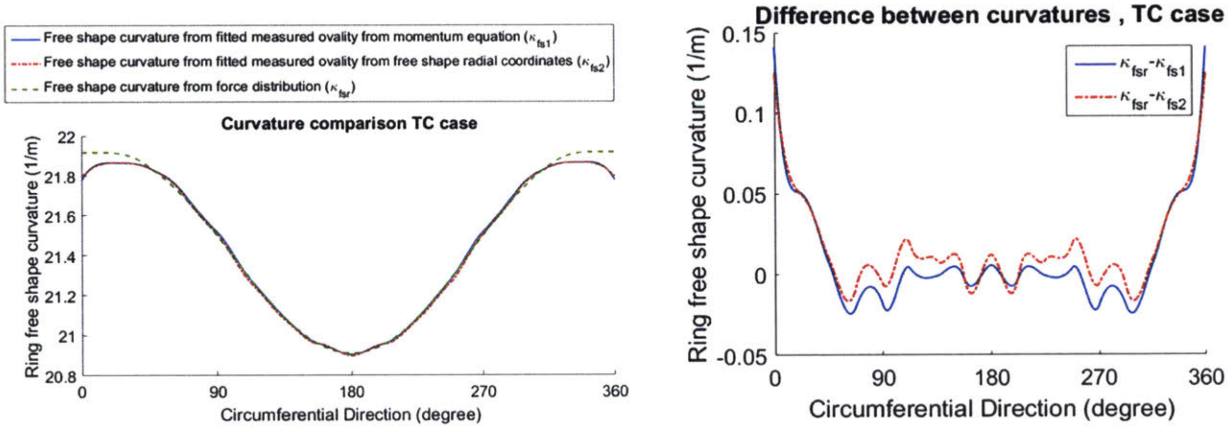

Figure 5.22 – Free shape curvature comparison for measured ovality (TC case)

We explain these discrepancies by two factors. First, the fitted ovality and the one obtained in section 5.5 from the theoretical force distribution that lets us recover the right curvature and thus the force distribution, are off by $\pm 8\mu m$ for the usual case and $\pm 9\ \mu m$ for the TC one as we can see in Figure 2.23 and 2.24. This is well coherent with the radial distances deviation reported by Mahle. The modes observed in these differences correspond to low frequencies while the white noise filtered by our least square method present high frequencies as we observed in Figures 5.15 and 5.16. We also notice that the white noise present comparable amplitudes to the modes corresponding to the differences observed between the fitted ovality and the one giving the right free shape and force distribution. We also verified our data fitting, by adding the difference between the ovality measurement and its fit, to the ovality computed from the theoretical force distribution (the ovality that gives back the right free shape and force distribution) and then processing that artificial ovality by fitting it and using it as an input to our model. For both cases (Usual and TC) we were able to recover the exact free shape and force distribution.

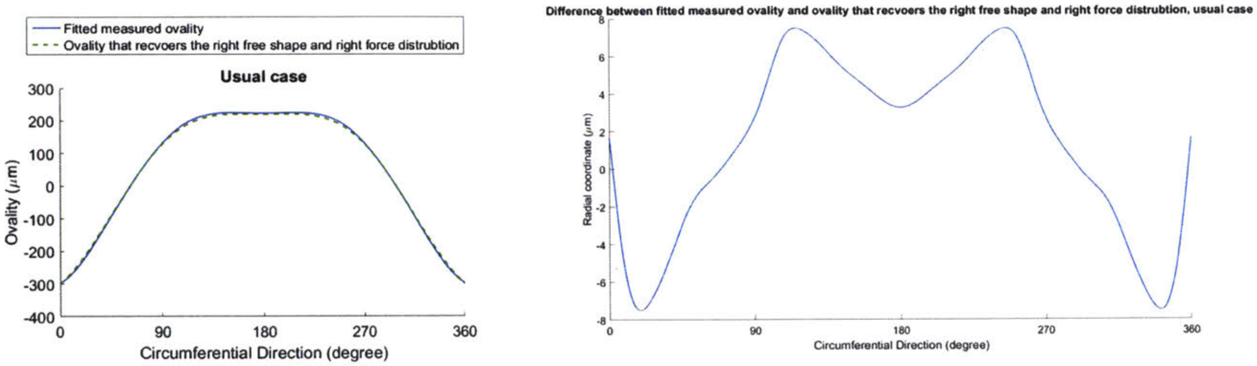

Figure 5.23 – Comparison of fitted measured ovality and ovality that recovers the right free shape and force distribution in usual representation (usual case)

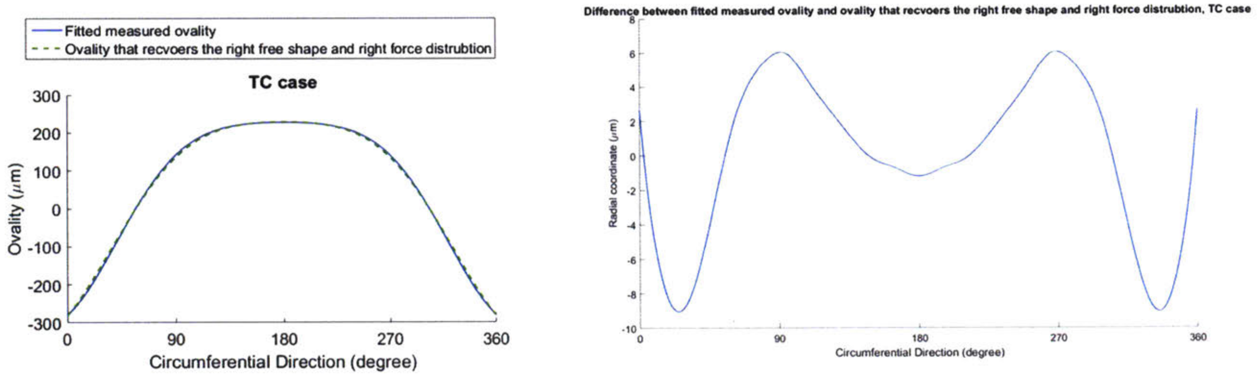

Figure 5.24 – Comparison of fitted measured ovality and ovality that recovers the right free shape and force distribution in usual representation (TC case)

The second reason that may explain the discrepancies observed is that even if the fitted ovality is still a good approximation within the deviation observed, its first and second derivatives should also be comparable to those of the right ovality. Indeed the free shape curvature depends directly for the ovality curvature based on the momentum equation (2.45) and the ovality curvature is a function of the radial displacement and its first and second derivatives (equation 5.13). Figures 5.25 and 5.26 confirm the fact that even though the first derivative of the fitted ovality seems to be a fairly good approximation of the exact one, its second derivative present a more significant deviation from the ideal second derivative distribution, both for the usual and the TC case.

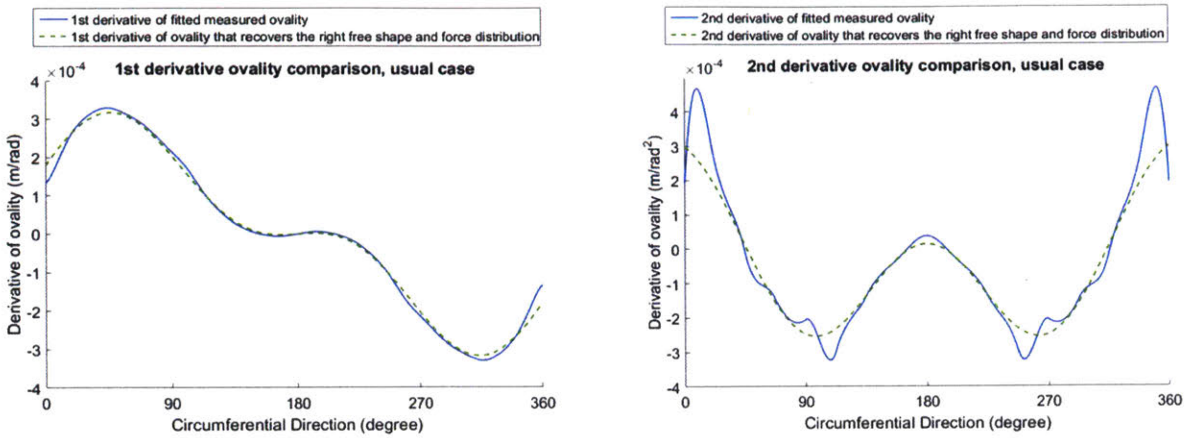

Figure 5.25 – Comparison of 1st and 2nd derivatives of fitted measured ovality and ovality that recovers the right free shape and force distribution in usual representation (usual case)

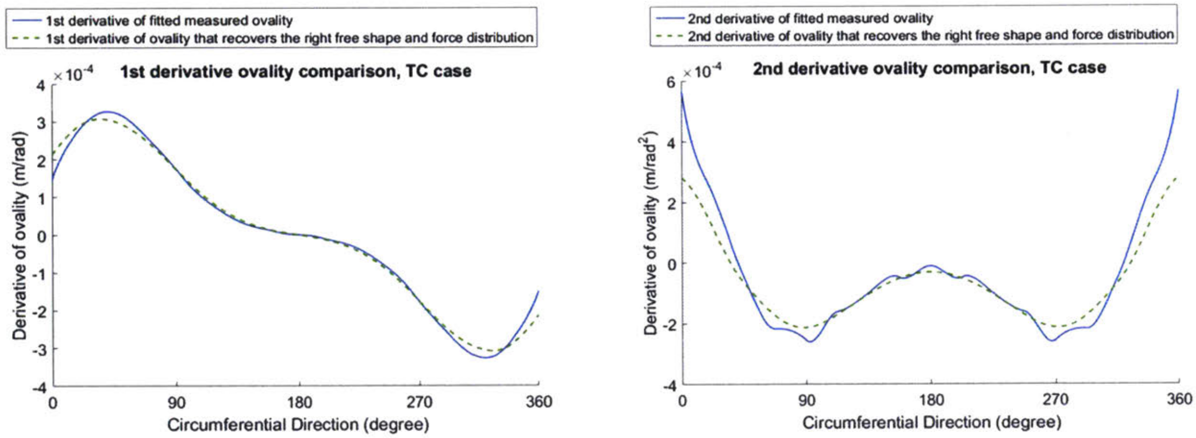

Figure 5.26 – Comparison of 1st and 2nd derivatives of fitted measured ovality and ovality that recovers the right free shape and force distribution in usual representation (TC case)

Finally, using the curvatures computed from the fitted ovality we determine the force distribution in closed circular shape. Figures 5.27 and 5.28 show the results obtained. We used 16 elements and 1000 points per element for the forces evaluations. We tried different combination of these numbers and run our models even with 256 elements but it did not improve the results.

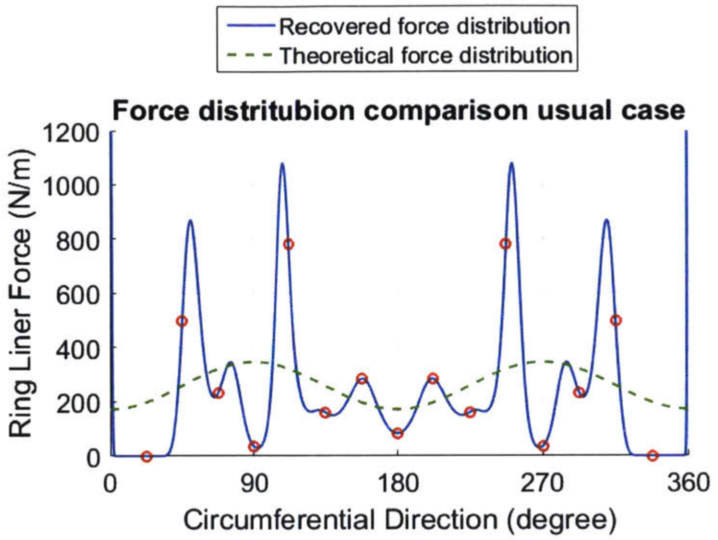

Figure 5.27 – Force distribution recovered from measured ovality comparison (usual case)

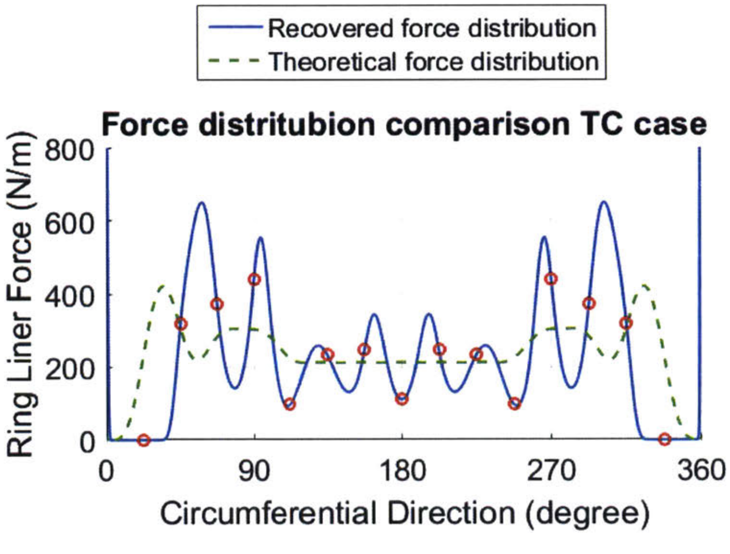

Figure 5.28 – Force distribution recovered from measured ovality comparison (TC case)

We increased the liner roughness from $0.3\ \mu m$ to 3 and $10\ \mu m$ (which are not an acceptable values for typical cylinders) in order to smoothen the force distribution. The results obtained are plotted in Figures 5.29 and 5.30. Both values of roughness gave better results for the two cases. For the TC one, the roughness of $3\ \mu m$ gives the best results since it smoothens the force distribution enough to be close to the theoretical one but without losing the characteristic variations like the peaks around 30° and 330°. However, for the usual case the best results were obtained for a roughness of $10\ \mu m$. This approach could be generalized provided we determine a process that gives the best liner roughness to consider for any arbitrary ring without knowing the theoretical force distribution.

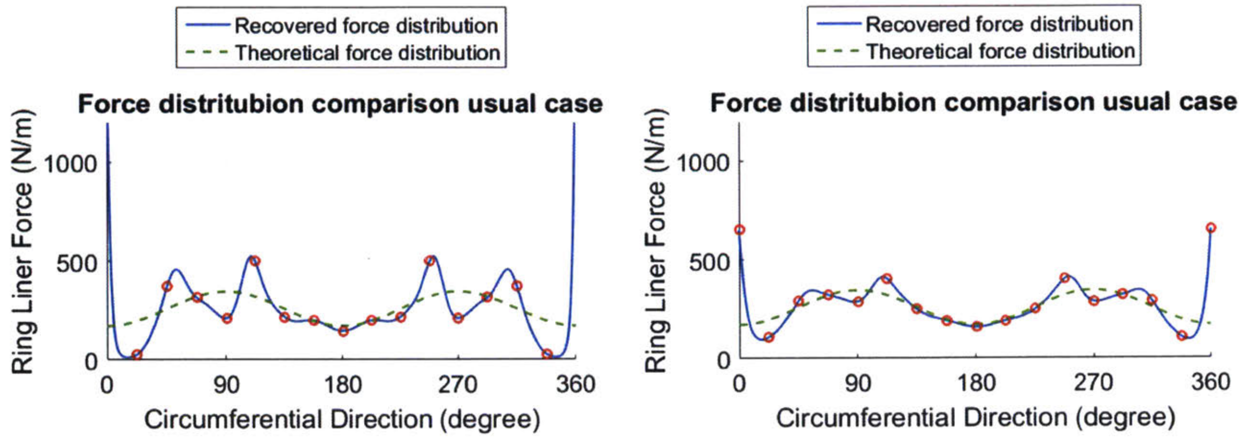

Figure 5.29 – Force distribution recovered from measured ovality comparison for a liner roughness of 3 (left curve) and $10\ \mu m$ (right curve) for the usual case

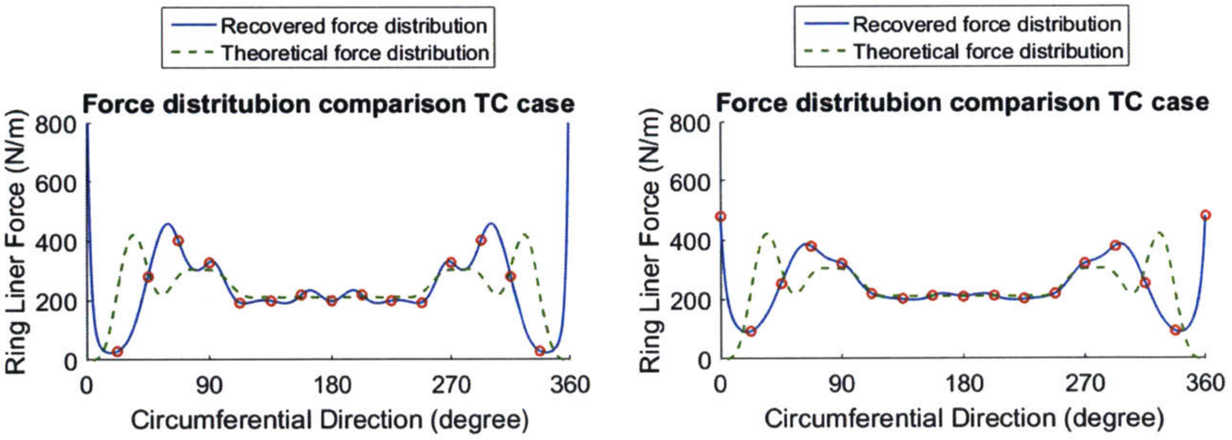

Figure 5.30 – Force distribution recovered from measured ovality comparison for a liner roughness of 3 (left curve) and $10\ \mu m$ (right curve) for the TC case

Last, we tried some heuristic approaches like fitting the data with only one polynomial for the whole ring instead of one polynomial for each element. The order of the polynomial was determined heuristically and we opted for an 8th order polynomial for the usual case. The curvatures and force distribution obtained from that fitted ovality are given in Figure 5.31 and in Figures 5.32 and 5.33 respectively and we can see that it gives much better results than those obtained with the least square method applied with our 3rd order polynomial shape functions. We also notice that tuning the liner roughness value lets us improve the results but without reaching the exact force distribution. However we have no guarantee that this 1 polynomial fit approach is general for any ring design, while the curved beam model and the 3rd order polynomials used rely on the definition of the curvature that depends on the 1st and 2nd derivatives of the radial displacement, which explains the necessity of using at least 3rd order polynomials as stated in section 2.

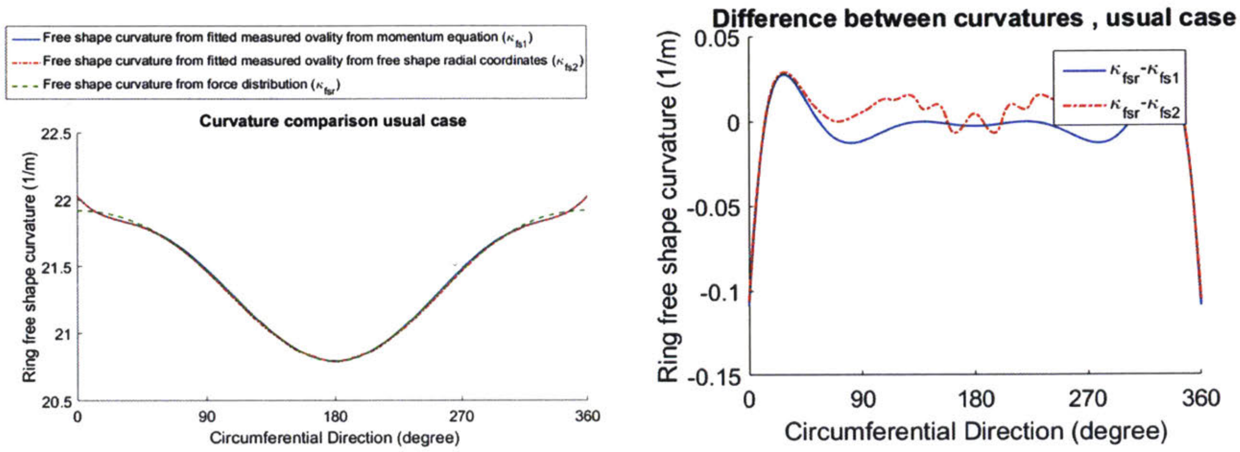

Figure 5.31 – Free shape curvature comparison for fitted measured ovality with one 8th order polynomial for the whole ring (usual case)

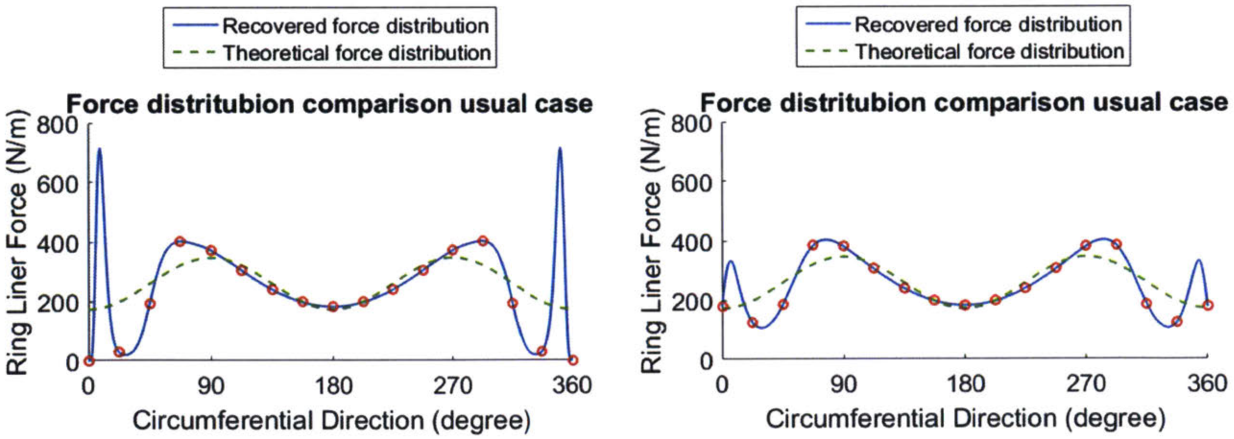

Figure 5.32 – Force distribution recovered from fitted measured ovality with one 8th order polynomial for the whole ring with a liner roughness of 0.3 (left curve) and $3\ \mu m$ (right curve) for the usual case

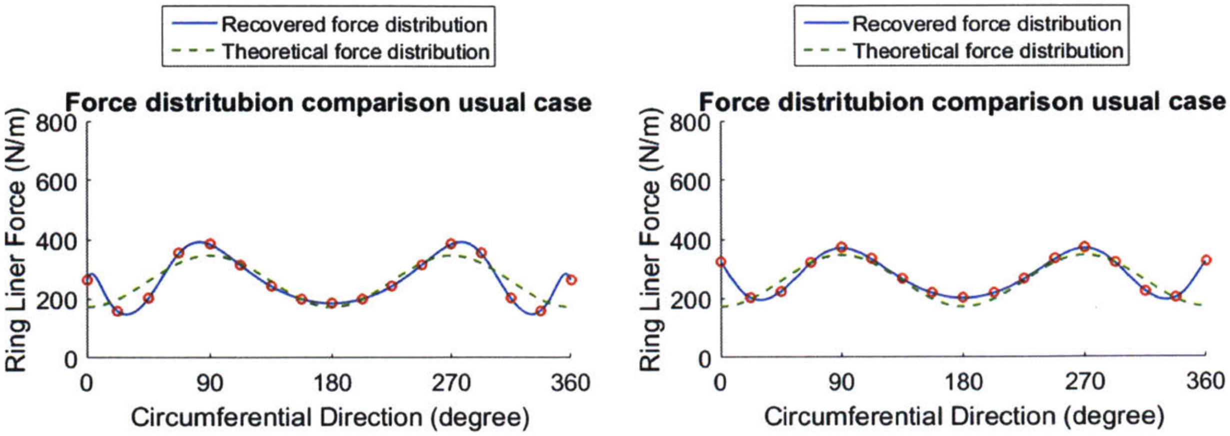

Figure 5.33 – Force distribution recovered from fitted measured ovality with one 8th order polynomial for the whole ring with a liner roughness of 10 (left curve) and $50\ \mu m$ (right curve) for the usual case

As we can see in Figures 5.21 and 5.22 and in Figures 5.25 and 5.26 (even in Figure 5.29 and 5.30), the free shape 2nd order derivatives and curvature mismatches occur mainly close to the tips (and hence for the force distribution too). Therefore we tried to remove some of the results obtained close to the ring gap and extrapolate those values based on the neighboring points. This improved the results as we can see in Figure 5.34 and Figure 5.35 but determining the criteria defining which points to remove and which extrapolation technique to use in order to generalize this approach was not studied. For the two cases presented below, we remove the curvature values between 0° and 30° and between 330° and 360° and use the extrapolation based on the neighboring points. For the fit using the least square method based on 3rd order polynomial shape functions (Figure 5.34) we used a linear extrapolation and a liner roughness of $10\ \mu m$. Compared to the results obtained from the same fit and liner roughness without extrapolation (Figure 5.29 right graph), we improved significantly the force distribution recovered. On the other hand, for the fit using one 8th order polynomial for the whole ring (Figure 5.35) we used a cubic extrapolation and a liner roughness of $0.3\ \mu m$ and again we observe a net improvement in the recovered force distribution compared to the output obtained from the same fit and liner roughness without extrapolation (Figure 5.32 left graph).

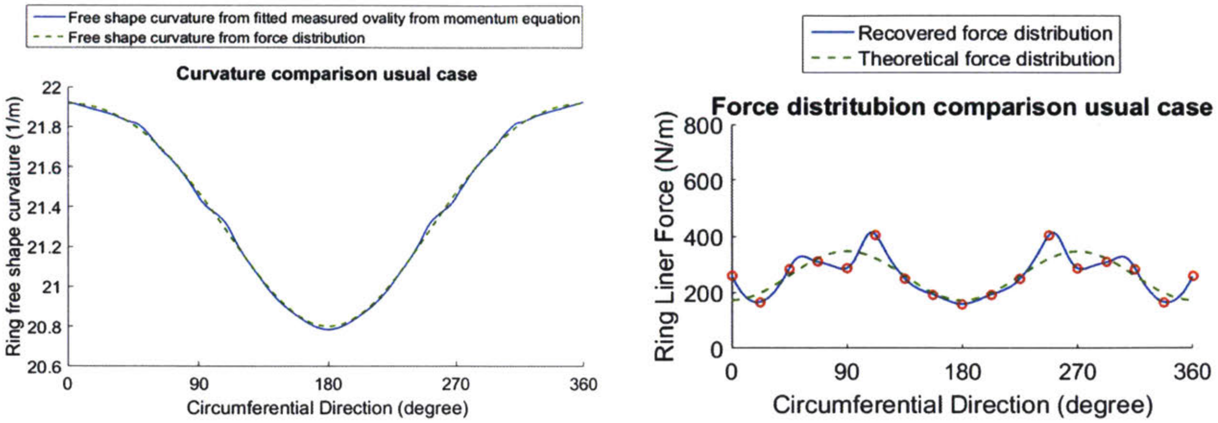

Figure 5.34 – Extrapolated curvature and force distribution comparison from fitted measured ovality with the least square method based on 3rd order polynomial shape functions (usual case)

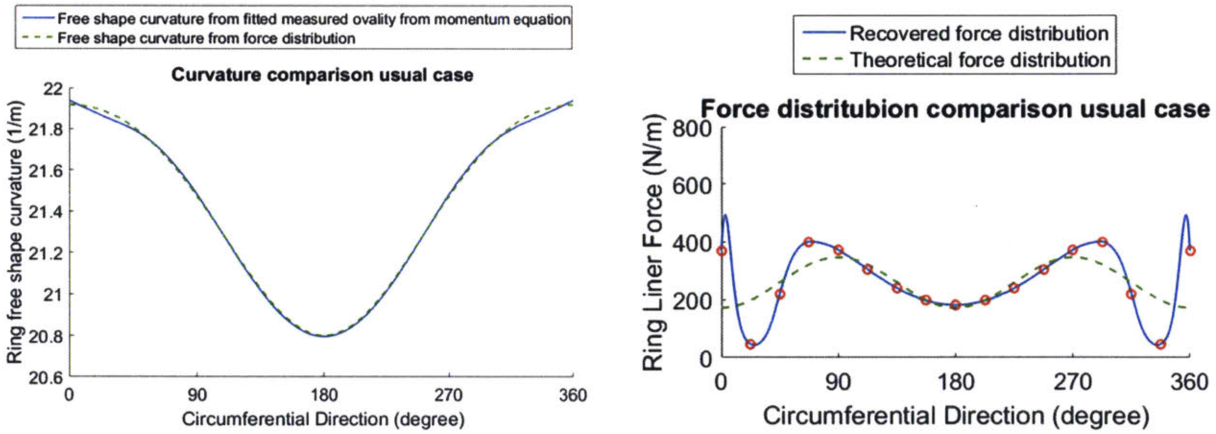

Figure 5.35 – Extrapolated curvature and force distribution comparison from fitted measured ovality with one 8th order polynomial for the whole ring (usual case)

5.7. Conclusion

We have developed a set of consistent models to relate the force distribution in closed circular shape, the free shape and the ovality in a way that lets us recover any two of these three distributions by just knowing the third one. The sub-model taking the ovality as input recovers the other two distributions for any closed shape. These models were validated theoretically by proving their consistency.

We tried to apply these models to measured ovality by looking for the ring free shape and force distribution. Fitting the measurement with a least square model based on the 3rd order polynomial shape functions used in our curved beam model lets us recover the ring free shapes properly for the two sets of data (Usual and TC). However the free shape curvature that depends on the first and second derivative of the free shape radial coordinates was not close enough to the exact one that recovers the proper force distribution. Some heuristic approaches based on a single higher order polynomial fit for the whole ring ovality, or on tuning the liner roughness or on removing some of the curvature values computed close to ring gap and using extrapolation were carried out. These techniques showed overall satisfactory results by considerably improving the force distribution recovered. However no theoretical or at least deterministic framework to generalize any of these approaches for any arbitrary ring was developed.

As shown previously the ovality measurement deviations provided by Mahle explain well the difference obtained between the fitted ovality and the theoretical one. This difference is large enough to make our model unable to recover the force distribution. Apart from other fitting techniques for the measured ovality, a statistical treatment for repeated measures carried on the same ring or a better experimental measurement process could be considered too. Besides, measurement related sources of error could be investigated further by considering more advanced and probably automated measurement techniques in the future like laser based ones to minimize human introduced deviations. Finally we may also consider the influence of the friction when closing the ring. Indeed, computing the ring free shape based on the momentum equations (5.19) and (5.20) assumes that the force applied on the ring is locally normal as shown in Figure 5.3. Considering some friction models, even simple ones based on constant friction coefficient, could give us an idea on the influence of the force tangential component on our results.

6. Conclusion

To investigate the ring structure response, we developed a complete ring design tool based on curved beam finite element method presented in Chapter 2 that relates the global and local behaviors of the ring. The conformability analysis relies on the multi-scale meshing to solve the ring structural deformation using a coarse mesh but considering the different interactions with the liner and piston on a finer contact grid. As proven by the results presented, this method allows efficient coupling of structural deformation of the ring and contact forces at the ring-liner and ring-groove interfaces which occur at different length scales. Hence, we are able to relate the global and local behavior of the ring that are affected by bore distortion, temperature distribution and gas pressure and by gap location and local contact change with different boundary conditions such as birding respectively. The curved beam finite element method was also extended to study the static twist under fixed ID/OD constraint and also used to relate the ring's free shape, its ovality and the force distribution in radial bore by determining any two of these variables from the third one. This is the first tool, whether based on curved or straight beam model, which is able to give this characterization.

6.1. Summary and main findings

The conformability model presented in Chapter 3 characterizes the ring statics behavior inside the piston by considering gas pressure, dry and hydrodynamic ring-liner and ring-groove contacts along with the thermal moment. We used that tool to understand some local processes and its effect on the ring-liner and ring-groove conformability. In particular we looked at the effect of the radial temperature gradient and showed that our model generalizes the existing one by considering the bending moment along the whole ring and not restricting it at the tips. Relating the global and local behaviors of the ring, we analyzes the effect of the ring gap location within a distorted bore on the ring-liner conformability. This structural response affects the oil consumption and the sealing performance of the ring pack system. Ring structural response also depends on local oil distribution on the liner and the groove flanks. In particular we studied the effect of the oil peak location on the liner with respect to the ring gap. Although having that peak at the ring gap makes the radial force smoother and thus limits the wearing effect, it increases oil consumption. We also used that tool to quantify the threshold that should be used to distinguish between the two lubrication boundary conditions. The same analysis characterizes the ring response to local oil accumulation or bridging. Besides we carried out a study of the ring-groove conformability by looking at the condition that should be satisfied by the gas pressures in order to maintain the ring-groove lower flank conformability based on the friction and the inertial forces applied on the ring during the engine cycle, mainly for the first half of the intake stroke. This analysis gives a quantifiable condition that ensures the ring conformability with the groove lower flank, thus preventing oil from flowing around the ring to the groove inner region and then to piston upper parts increasing its consumption.

In Chapter 4, we extended the curved beam model based on nodal displacements to determine the static twist under fixed ID/OD by simulating the axial taping force carried out in the experimental set-up. We also gave a physical understanding of the generation of the static twist from the radial pressure based on the internal stress created by the twist of each cross section on the adjacent one resulting in an increasing total twist angle from the ring tips to the ring back. A study of the ring's asymmetry effect along with sample results was also presented. This tool helps design the ring to obtain the desired static twist in order to control oil and gas transport. Indeed, non-zero static twist makes the ring push against the top groove lower flank and make sure the ring prevents gas leakage when its upper surface is exposed to high gas pressure. The amplitude of the static twist can be tuned base on the dimensions of the cut off engineered at the upper ID.

Finally, in Chapter 5 we present the four models developed to relate the ring's free shape, its ovality and force distribution in radial bore, which defines a complete tool that relates in any desired order these three ring's characterizations. The sub-model computing the free shape and force distribution using the ovality can consider any closed shape. A theoretical validation of these four models is presented by recovering the radial force distribution used first as an input and then recovered after being processed through all the four models. We also recovered the free shapes of two different rings using ovality measurement fitted with a least square method based on the shape functions used in our curved beam model. However the computed free shape curvature was not close enough to the exact one to recover the right force distribution in radial bore. Some heuristic approaches based on a single higher order polynomial fit for the whole ring ovality, or on tuning the liner roughness or on removing some of the curvature values computed close to ring gap and using extrapolation gave better results.

6.2. Future work

The ring conformability is crucial for the ring pack performances in terms of gas sealing and oil consumption. We used our model to analyze ring structural responses to different global and local conditions. Further analyzes based on dimensionless number need to be carried out in order to relate these behaviors in a more general frame work. For instance, the results presented in section 3.4.3.1 could be improved by looking at the effect of the ring stiffness (cross section and Young's modulus), its free shape, the bore diameter, its distortions and the gas pressures on the results obtained. Moreover our model could be extended to quantify the amount of oil that is scraped because of bridging and determine the effective parameters that determine it. Besides, the ring-groove conformability given in section 3.4.3.2 can also be extended to investigate other factors that affect the results like the ring free shape, the bore diameter, its distortions and the RPM considered. In addition the whole conformability model could be upgraded by modelling the ring tips overlapping. This upgrading can also be applied to the static twist under fixed ID/OD constraint model. Furthermore, that framework can be used to investigate further the effect of applying a tapping force at other locations than on the centroid and the effect of imposing smaller clearances constraint. These enables modelling other experimental scenarios different from the ideal one.

Finally, for the free shape, ovality and force distribution in radial bore model, the ovality measurement deviations explain well the difference obtained between the fitted ovality and the theoretical one. This difference is large enough to make our model unable to recover the right force distribution. A theoretical or at least deterministic framework to generalize any of the heuristic approaches that we tired would be of utmost usefulness. Besides, a statistical treatment for repeated measures carried on the same ring or a better experimental measurement process could be considered too in order to minimize the measurement related sources of error. Finally, friction could also be considered when computing the ring free shape to have an idea on the influence of the force tangential component on the results obtained.

References

[1] D. E. Richardson, "Review of power cylinder friction for diesel engines," *Journal of engineering for gas turbines and power,* vol. 122(4), pp. 506-519, 2000.

[2] *K. Liao, "Factors Affecting Piston Ring Friction," Ph.D. Thesis, the Department of Aeronautics and Astronautics, Massachusetts Institute of Technology, Cambridge, MA, 2013.*

[3] L. L. Ting, "Development of a Reciprocating Test Rig for Tribological Studies of Piston Engine Moving Components - Part I: Rig Design and Piston Ring Friction Coefficients Measuring Method," SAE Technical Paper, no. 930685, 1993.

[4] L. L. Ting, "Development of a Reciprocating Test Rig for Tribological Studies of Piston Engine Moving Components-Part II: Measurements of Piston Ring Friction Coefficients and Rig Test Confirmation," SAE Technical Paper, no. 930686, 1993.

[5] M. Takiguchi, K. Watanabe, T. Kato, M. Sato, and H. Ueno, "Effects of piston ring tension on oil consumption and piston friction in diesel engines," in ASME ICE Spring Technical Conference, 1999, vol. 32.

[6] R. B. Edara, "Reciprocating engine piston secondary motion-literature review," SAE paper, vol. 2008011045, 2008.

[7] D. Bai, "Modeling Piston Skirt Lubrication in Internal Combustion Engines," Ph.D. Thesis, the Department of Mechanical Engineering, Massachusetts Institute of Technology, Cambridge, MA, 2012.

[8] Tian, T., 2002, "Dynamic Behaviors of Piston Rings and Their Practical Impact. Part 1: Ring Flutter and Ring Collapse and Their Effects on Gas Flow and Oil Transport," Proc IMechE, Part J: Journal of Engineering Tribology, Vol. 216, pp. 209-227

[9] Tian, T., 2002, "Dynamic Behaviors of Piston Rings and Their Practical Impact. Part 2: Oil Transport, Friction, and Wear of Ring/Liner Interface and the Effects of Piston and Ring Dynamics," Proc IMechE, Part J: Journal of Engineering Tribology, Vol. 216, pp. 229-247

[10] Timoshenko, S., and Lessells, J. M., Applied Elasticity, Westinghouse Press, 1925.

[11] Sun, D. C., "A Thermal Elastica Theory of Piston-Ring and Cylinder-Bore Contact," ASME Journal of Applied Mechanics, Vol.58, pp. 141-153, 1991.

[12] E. W. Schneider, D. H. Blossfeld, D. C. Lechman, R. F. Hill, R. F. Reising, and J. E. Brevick, "Effect of cylinder bore out-of-roundness on piston ring rotation and engine oil consumption," SAE Technical Paper, 1993.

[13] H. Hitosugi, K. Nagoshi, M. Komada, and S. Furuhama, "Study on mechanism of lubricating oil consumption caused by cylinder bore deformation," Internal Combustion Engines, vol. 2015, pp. 06–22, 1996.

[14] H. Hitosugi, K. Nagoshi, M. Ebina, and S. Furuhama, "Study on cylinder bore deformation of dry liner in engine operation," JSAE review, vol. 17, no. 2, pp. 113–119, 1996.

[15] R. Müller, "Zur Frage des Formfüllungsvermögen von Kolbenringen in von der Kreisform abweichenden Bohrungen gleicher Umfangslänge," MTZ, vol. 31, pp. 79–82, 1970.

[16] V. V. Dunaevsky, "Analysis of distortions of cylinders and conformability of piston rings," Tribology transactions, vol. 33, no. 1, pp. 33–40, 1990.

[17] Dunaevsky, V., Alexandrov, S., Barlat, F., 2000, "Analysis of Three-Dimensional Distortions of the Piston Rings with Arbitrary Cross-Section," SAE Paper 2000-01-3453.

[18] V. V. Dunaevsky, S. Alexandrov, and F. Barlat, "Fundamentals for analysis of threedimensional distortions of the piston rings," in Proceedings of the 2000 Fall Technical Conference of the ASME Internal Combustion Engine Division, 2000, pp. 15–22.

[19] V. V. Dunaevsky, "Development of conformability model of piston rings with consideration of their three-dimensional torsional distortions and Fourier series representation of cylinder bore geometry," in SAE Technical Paper 2002-01-3131, 2002.

[20] V. Dunaevsky and J. Rudzitis, "Clarification of a Semi-Empirical Approach in Piston Ring-Cylinder Bore Conformability Prediction," Journal of Tribology, vol. 129, no. 2, p. 430, 2007.

[21] E. Tomanik, "Piston ring conformability in a distorted bore," SAE transactions, vol. 105, no. 5, pp. 394–405, 1996.

[22] E. Tomanik, "Improved Criterion for Ring Conformability Under Realistic Bore Deformation," in SAE Technical Paper 2009-01-0190, 2009.

[23] Ma, J., Ryan, T. W., Winter, J., and Dixon, R., 1996, “The Piston Ring Shape and Its Effects on Engine Performance,” SAE Paper 960052.

[24] M. A. Ejakov, H. J. Schock, and L. J. Brombolich, “Modeling of Ring Twist For an IC Engine,” in SAE Technical Paper 982693, 1998.

[25] L. Liu, T. Tian, and R. Rabuté, “Development and Applications of an Analytical Tool for Piston Ring Design,” in SAE Technical Paper 2003-01-3112, 2003.

[26] L. Liu and T. Tian, “A Three-Dimensional Model for Piston Ring-Pack Dynamics and Blow-By Gas Flow,” in ASME 2004 Internal Combustion Engine Division Fall Technical Conference ICEF2004-0968, 2004.

[27] L. Liu and T. Tian, “Modeling Piston Ring-Pack Lubrication With Consideration of Ring Structural Response,” SAE International, Warrendale, PA, 2005-01-1641, Apr. 2005.

[28] Prescott, J., Applied Elasticity, Dover Publication Inc. New York, 1925.

[29] Dunaevsky, V., Alexandrov, S., Barlat, F., 2001, “The Effect of Contact Pressure on Piston Ring Twist,” SAE Paper 2001-01-2720.

[30] L. Liu, “ Modeling the Performance of the Piston Ring-Pack with Consideration of Non-Axisymmetric Characteristics of the Power cylinder System in Internal Combustion Engines,” Ph.D. Thesis, the Department of Mechanical Engineering, Massachusetts Institute of Technology, Cambridge, MA, 2005.

[31] C. Baelden, “A multi-scale model for piston ring dynamics, lubrication and oil transport in internal combustion engines," Ph.D. Thesis, the Department of Mechanical Engineering, Massachusetts Institute of Technology, Cambridge, MA, 2014.

[32] S. P. Timošenko, Strength of Materials: Elementary Theory and Problems, D. Van Nostrand Company, 1940.

[33] Y. Liu “A Multi-scale Model Integrating both Global Ring Pack Behavior and Local Oil Transport in Internal Combustion Engines,” Ph.D. Thesis, the Department of Mechanical Engineering, Massachusetts Institute of Technology, Cambridge, MA, 2017.

[34] A. N. Pressley, Elementary differential geometry, Springer Science & Business Media, 2010.

[35] H. Chen, "Modeling the lubrication of the piston ring pack in internal combustion engines using the deterministic method," Ph.D. Thesis, the Department of Mechanical Engineering, Massachusetts Institute of Technology, Cambridge, MA, 2011.

[36] Y. Liu, "Developing an approach utilizing local deterministic analysis to predict the cycle friction of the piston ring-pack in internal combustion engines," Master Thesis, the Department of Mechanical Engineering, Massachusetts Institute of Technology, Cambridge, MA, 2013.

[37] J. A. Greenwood and J. H. Tripp, "The contact of two nominally flat rough surfaces," Proceedings of the institution of mechanical engineers, vol. 185, no. 1, pp. 625-633, 1970.

[38] Y. Hu, H. S. Cheng, T. Arai, Y. Kobayashi and S. Aoyama, "Numerical Simulation of Piston Ring in Mixed Lubrication - A Nonaxisymmetrical Analysis," ASME Journal of Tribology, vol. 116(3), pp. 470-478, 1994.

[39] H. Chen, Y. Li and T. Tian, "A novel approach to model the lubrication and friction between the twin-land oil control ring and liner with consideration of micro structure of the liner surface finish in internal combustion engines," SAE Technical Paper, no. 2008-01-1613, 2008.

[40] T. Tian, "Modeling the Performance of the Piston Ring-Pack in Internal Combustion Engines," Ph.D. Thesis, the Department of Mechanical Engineering, Massachusetts Institute of Technology, Cambridge, MA, 1997.

[41] Mierbach, A., Duck, G. E., and Newman, B. A., 1983, “Heat Flow through Piston Rings and Its Influence on Shape,” SAE Paper 831283.

[42] S. S. V. Przesmitzki, "Characterization of oil transport in the power cylinder of internal combustion engines during steady state and transient operation," Ph.D. Thesis, the Department of Mechanical Engineering, Massachusetts Institute of Technology, Cambridge, MA, 2008.

[43] E. B. Senzer, "Oil transport inside the oil control ring grove and its interaction with surrounding areas in internal combustion engines," Ph.D. Thesis, the Department of Mechanical Engineering, Massachusetts Institute of Technology, Cambridge, MA, 2012.

[44] T. Fang, "Computations and Modeling of Oil Transport between Piston Lands and Liner in Internal Combustion Engines," Master Thesis, the Department of

Mechanical Engineering, Massachusetts Institute of Technology, Cambridge, MA, 2014.

[45] S. Przesmitzki, A. Vokac and T. Tian, "An Experimental Study of Oil Transport between the Piston Ring Pack and Cylinder Liner," SAE Technical Paper, no. 2005-01-3823, 2005.

[46] Liu, L., Tian, T., and Rabuté, R., "Development and Applications of an Analytical Tool for Piston Ring Design," SAE Technical Paper 2003-01-3112, 2003, doi:10.4271/2003-01-3112.

[47] Tomanik, E. and Bruno, R., "Calculation of Piston Ring Radial Pressure Distribution from its Measured Free Shape," SAE Technical Paper 2012-01-1322, 2012, doi:10.4271/2012-01-1322.